VERTICAL VELOCITY OBSERVATIONS OF A FIRE II CIRRUS EVENT

by: Ran Song and Stephen K. Cox

Department of Atmospheric Science
Colorado State University
Fort Collins, CO 80523

Funding Agencies:
National Aeronautics and Space Administration
(Grant NAG 1-1146)
Department of Energy
(Contract No. DE-FG02-90ER60970)

Colorado State University

DEPARTMENT OF ATMOSPHERIC SCIENCE

PAPER NO. 560

"VERTICAL VELOCITY OBSERVATIONS OF A FIRE II CIRRUS EVENT"

Ran Song and Stephen K. Cox

Department of Atmospheric Science
Colorado State University
Fort Collins, CO 80523

Research Supported By

National Aeronautics and Space Administration (Grant NAG 1-1146)
Department of Energy (Contract No. DE-FG02-90ER60970)

July, 1994

Atmospheric Science Paper No. 560

ABSTRACT

VERTICAL VELOCITY OBSERVATIONS OF A FIRE II CIRRUS EVENT

The development of doppler radar wind profilers and their subsequent deployment have dramatically improved the spatial and temporal resolutions of wind observations. While the horizontal winds deduced from these observations are generally reliable, serious questions remain on the ability to reliably observe the vertical wind component. In an upper tropospheric cirrus cloud environment often characterized by weak backscatter signal strength, small magnitude vertical motions, high altitude and short life cycle, this problem is especially difficult. A review of the echo generating mechanisms for a 400 MHz radar system is presented. This study further examines the feasibility of determining reliable vertical motion fields from both individual and a network of wind profiler observations. Data employed in this research were collected during the FIRE II experiment in November and December of 1991. Vertical motions were calculated in three ways: directly from the doppler radial velocity observations, from a quasi-VAD method utilizing the four non-zenith profiler beams, and by applying the kinematic method to profiler network data. The deduced vertical wind fields from each method are compared. This research also includes a diagnostic study of a jet streak system observed on 26 November 1991; this study emphasizes the thermal and dynamic instability structures, the vertical forcing

and the ageostrophic circulation. Results from the diagnostic and previous theoretical studies are compared with the vertical velocity fields deduced from wind profiler observations.

ACKNOWLEDGEMENTS

The authors wish to express their appreciation to the following individuals: Professor Richard Johnson for his guidance in the analysis of the jet streak data; Paul Hein and John Davis for their assistance in obtaining the wind profiler network data and for valuable discussions about the FIRE case studies; Chris Cornwall and David Wood for their contributions to the collection of wind profiler data; Melissa Tucker, Dr. Takmeng Wong and Andrew Heidinger for their assistance in the preparation of this manuscript.

Sounding data used in this study were obtained from the National Center for Atmospheric Research. This research has been supported by the National Aeronautics and Space Administration under Grant NAG 1-1146, and The Department of Energy under Contract No. DE-FG02-90ER60970.

TABLE OF CONTENTS

Abstract			ii
Acknowledgements			iv
1.	**INTRODUCTION**		1
2.	**WIND PROFILER SYSTEM**		6
	2.1	Overview of CSU Wind Profiler	7
	2.2	Radar Echoing Mechanisms	10
	2.3	Signal Processing	17
		2.3.1 Coherent averaging and non-coherent averaging	19
		2.3.2 Noise estimate	19
		2.3.3 Ground clutter signal removal algorithms	20
		2.3.4 Calculations of Radar Signal Moments	23
	2.4	Wind Field Calculation	24
	2.5	Wind Profiler Performance in Detecting Clear Air Turbulence(CAT)	25
3.	**COMPARISON OF VERTICAL VELOCITY ANALYSIS TECHNIQUES**		34
	3.1	Methods and Observations	34
		3.1.1 Direct Doppler Method	35
		3.1.2 Quasi-VAD Method	49
		3.1.3 Kinematic Method	57
	3.2	Discussions	66
4.	**STUDIES ON A JET STREAK AND A CIRRUS CLOUD SYSTEM**		69
	4.1	Jet Streak (Ageostrophic Circulation)	69
	4.2	Cirrus Cloud	81
5.	**OBSERVATIONS AND ANALYSIS OF 26th NOVEMBER, 1991 CASE**		87
	5.1	Synoptic Features	87
	5.2	Observations of Clouds	89
	5.3	Soundings and Stability/Instability	92
	5.4	Wind Profiler Signal Power	111
	5.5	Horizontal Thermal Advection and the Ageostrophic Wind Field	117
	5.6	Divergence Structure and Vertical Wind Field	125

6. SUMMARY AND CONCLUSIONS 148

REFERENCES 152

APPENDIX A 157

APPENDIX B 159

Chapter 1

INTRODUCTION

Cirrus clouds play an important role in the climate change and general circulation due to their significant impacts on the global radiation budget. The radiative effect also interacts with the dynamical and thermodynamic structures of the cirrus cloud system. Establishing a knowledge of the dynamical and thermodynamic processes governing the evolution of cirrus clouds has become a major issue in the research of this cirrus-climate system. Field observations, diagnostic studies and numerical simulations are producing impressive results. The First ISSCP (International Satellite Cloud Climatology Program) Regional Experiment Phase II (FIRE II) experiment, which was conducted in Kansas in November and December of 1991, provided a good opportunity for research on these issues, especially since advanced instruments and conventional rawinsondes were effectively and cooperatively utilized. The vertical wind field is an important parameter for determining the microphysical development of cirrus cloud system and some other processes in a general circulation simulation, however, due to cirrus cloud systems' high altitude, short life time, rapid variation in thickness etc., the vertical wind field related to a cirrus cloud system is still relatively unknown.

The vertical wind field associated with the ageostrophic circulation of an upper-level jet streak has been studied by Namias and Clapp (1949), Uccellini and Johnson (1979), and recently by Shapiro and Kennedy (1981), Mattocks and Bleck

(1986), and Keyser and Shapiro (1986) etc.. Daily averaged vertical wind profiles in the vicinities of jet streaks were reported by Fukao et al. (1991) and Yoe and Ruster (1992). However, to the author's recollection, no observational evidences of the spatial and temporal structures of these wind fields have been produced.

The recent progress in radar wind profiling techniques enhances the capability and accuracy of in situ observations of the wind field. The NOAA Model-400 wind profiler network in the central U.S., for example, significantly improves both the temporal and spacial resolution of wind field observations. However, the direct measurement of vertical wind speeds, which utilizes the vertical beam radial velocity directly to define the vertical wind velocity, has not been put into operational usage due to the radar technique difficulties and errors caused by precipitation and complex atmospheric refractive structure. In this thesis, we will employ direct measurements from 400MHz wind profilers to retrieve vertical wind fields for a cirrus cloud case, and compare the observations with the results deduced from the conventional kinematic method and a quasi-VAD method. The observational results will be further interpreted, firstly, from the view of radar echo mechanisms which will involve analysis of atmospheric thermodynamic structure. Comparisons between the observed wind field and the diagnostic/theoretical studies of the atmospheric wind field, in this case symbolized by a jet streak system, will provide further validation of the radar observations.

During the FIRE II experiment, the locations of CSU (Colorado State University) and NOAA network wind profiler systems are shown in Figure 1.1.

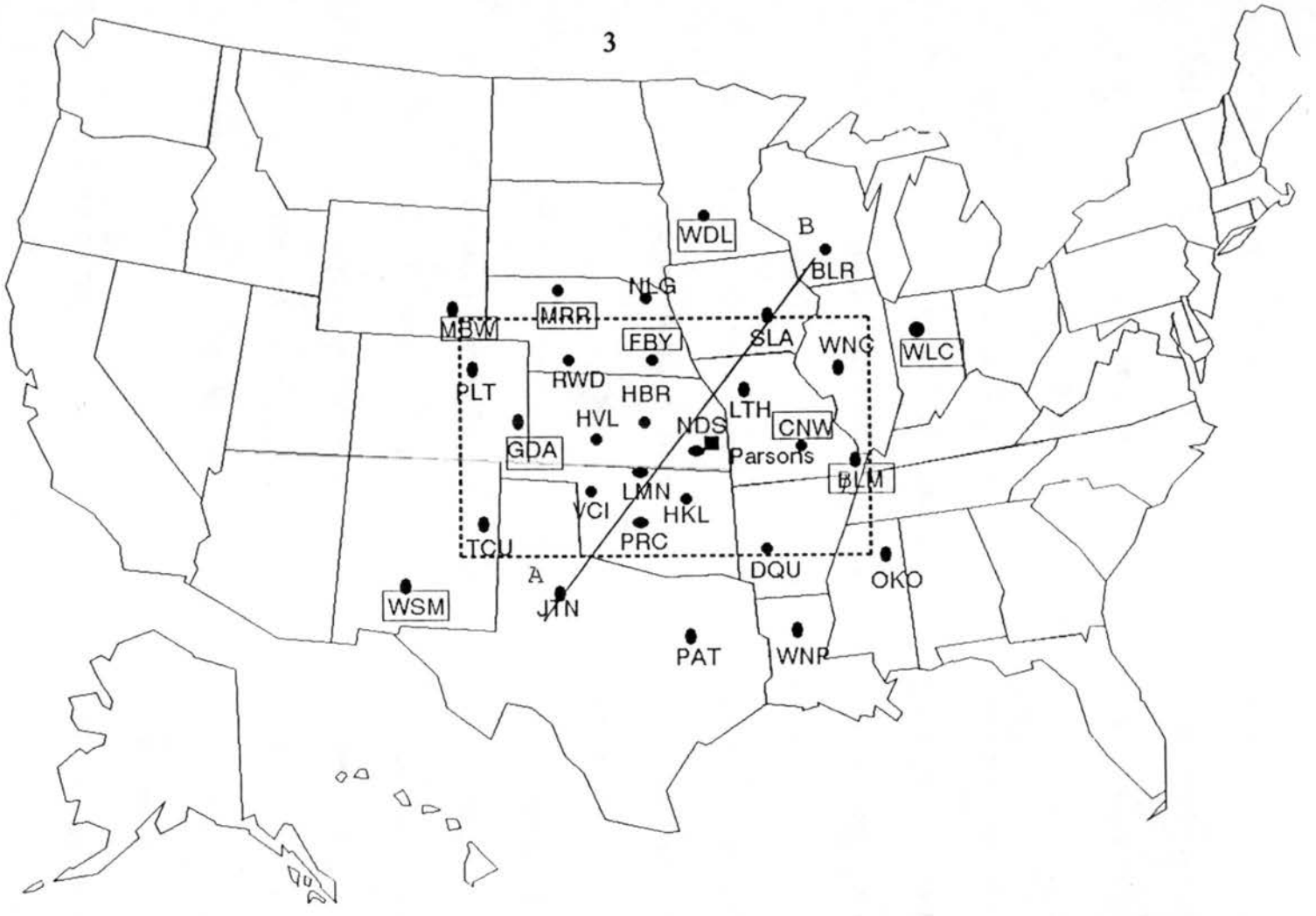

Figure 1.1 Map of wind profilers in central U.S.A. Circles represent NOAA wind profilers and the square is Parsons, Kansas, where the CSU wind profiler was located. The area marked by the dashed lines is the domain where NOAA wind profiler data is horizontally interpolated onto grid points with a resolution of 0.5°x0.5°, as applied in Chapter 5. Line AB is the cross section used in Chapter 5.

The black square is the experimental site (latitude: 37°18'N; longitude: 95°07'W; elevation: 269 meters) near Parsons, Kansas, where the CSU wind profiler is located. Black circles in Figure 1.1 represent NOAA wind profiler locations. Station geographical coordinates and elevations are shown in Table A.1.

For this study, we chose one significant cirrus cloud case on November 26, 1991. A strong jet streak system was passing over Colorado, New Mexico and reaching Kansas, Oklahoma and Texas (Figure 5.1) when cirrus clouds were reported by both sites at Parsons and Coffeyville, Kansas. From this typical jet-cirrus cloud case, the dynamical role of a jet streak in cirrus cloud development can be investigated. We also expect to provide more observations of ageostrophic circulations in the vicinity of a jet streak.

This thesis contains five major chapters. In chapter 2, the system of a Model-400 wind profiler, in particular the CSU wind profiler, will be introduced. The information includes the basic configuration of the radar and methods of signal processing and data processing. For the purpose of interpreting the radar observations in later chapters, the radar echo mechanisms are emphasized and wind profiler performance in terms of frequency response to clear air turbulence is analyzed based on the previous studies.

Chapter 3 gives a detailed discussion of the methods applied to retrieve the vertical wind field. These include Direct Doppler Method (DDM), Quasi-VAD Method (QVM) and Kinematic Method (KM). Results from each method are intercompared for a wind profiling cycle and for longer time averages.

Chapter 4 reviews classical conceptual models and the latest diagnostic studies of ageostrophic circulations related to a jet streak. This provides a general model against which the observations will be compared. Also, the ageostrophic circulation theories will be examined through the observations. The second part of this chapter discusses some of the thermodynamic properties and dynamical forcing of cirrus clouds and the cirrus environment, in particular, the thermal instability, Kelvin-Helmholtz instability and the vertical wind field, etc.

Chapter 5 presents an analysis of the November 26, 1991 case study. The static and dynamical instability structures of the cirrus cloud and cloud environment are investigated. The correlation between the radar signal return and atmospheric thermal structure is analyzed. The ageostrophic circulation of the jet streak and the vertical air transfer related to the cirrus cloud system are studied in detail.

Chapter 6 summarizes the conclusions of this study and gives suggestions for future research.

Chapter 2

WIND PROFILER SYSTEM

With the advent of radiosondes, significant advances were made in measuring the spacial and temporal variabilities of the atmospheric state variables, such as temperature, pressure and even humidity, and wind as a function of height. However, launched only on a regular time period, usually a 12 hour interval, radiosonde data are adequate only for the large-scale weather observations. Also since balloons move with the wind, the sounding data are not solely a function of height. The development of wind profilers provides an opportunity for continuous monitoring of the wind fields above an experiment site at a much finer temporal resolution than radiosondes could ever hope to achieve.

During the FIRE II experiment, the CSU wind profiler was operated in a five-beam mode. It provided the following formats of data:1) raw spectra (after FFT and time-domain averaging) every 10 minutes; 2) product data generated by a Tycho[1] algorithm including profiles of signal power, radial velocities and spectral bandwidth at a 10-minute cycle; 3) 10-minute and hourly averaged horizontal wind profiles deduced from the above product data. The wind profilers in the NOAA network were operated in a 3-beam mode. Radial velocities of three beams were provided for a cycle of six minutes. The hourly averaged products only contained horizontal

[1]Tycho, Subsidary of Vaisala, Inc.

wind components. Appendix A gives more about the geographic location and beam orientations of these wind profilers.

In this chapter, the echo mechanisms of a wind profiler are discussed. The influences of precipitation and cloud ice particles will be addressed. The signal processing and the radar moment calculations will also be presented based on the CSU wind profiler system. Finally, a method of estimating the optimum radar wavelength for detecting clear air turbulence based mainly on previous studies is discussed.

2.1 Overview of CSU Wind Profiler

Radar (RAdio Detecting And Ranging) was initially designed for detecting solid object tracers, such as airplanes. Not long after its introduction, it was discovered that radar can also "see" hydrometers such as rain and ice particles in the atmosphere. A Doppler radar, such as a wind profiler, also can be utilized to measure the atmospheric winds above the profiler site. Radar techniques have been extensively applied in the meteorological community.

Since a wind profiler conceptually receives signal from air, it is also often called a "clear air radar." This name is sometimes misleading since a wind profiler can also receive echoes from cloud particles and precipitation. Wind profilers are developed as pulse Doppler radars and generally operate at frequencies from 50MHz to 900MHz. The model 400 wind profilers used by CSU and the NOAA network operate at 404.37MHz. A general beam configuration of a Model 400 wind profiler

is shown in Figure 2.1. In this configuration, four beams are tilted 15° off the vertical and point in different directions 90° azimuthally apart, such as the east, north, west, and south for CSU wind profiler. Note there is only one vertical beam. Data are collected simultaneously at 64 range gates for each direction (Figure 2.2). Using these five-beam measurements (or at least three beams: two azimuthally orthogonal oblique beams and one vertical beam), the Model 400 wind profiler theoretically can provide measurements of horizontal and vertical winds up to 15km - 16km above the radar site up.

The wind profiler system mainly consists of two parts: the radar system and the computer work station for system operating and data processing. Data can be provided continuously with a cycle set up by the operator, such as the 10-minute cycle used by the CSU wind profiler in the FIRE II experiment. The CSU wind profiler provided data in the formats of 1) raw spectra, 2) processed moments including signal power, velocity, and variance (i.e. the spectral bandwidth), and 3) hourly averaged horizontal winds. Some basic parameters of the radar are shown in Table 2.1.

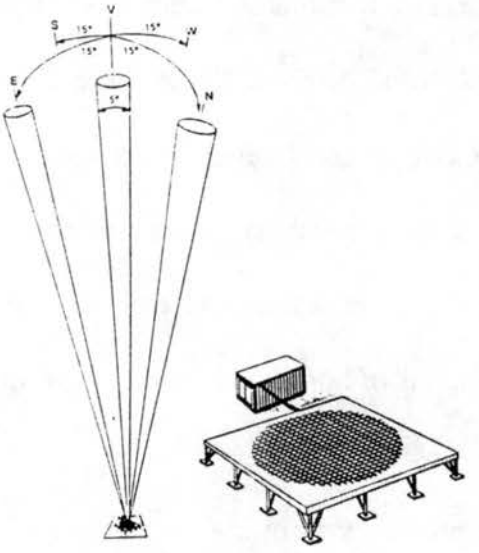

Figure 2.1 Typical beam configuration for a Model 400 wind profiler. (From Peterson, 1988)

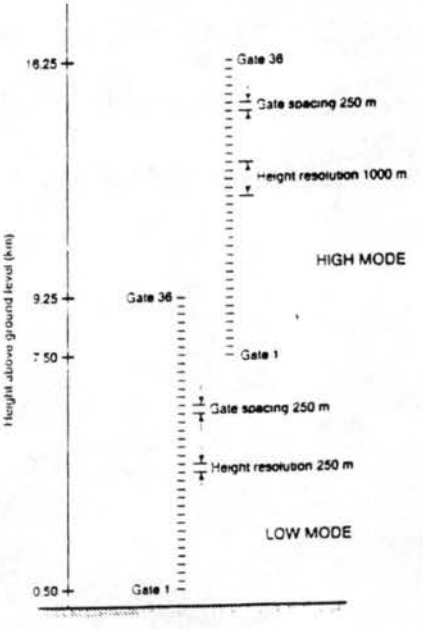

Figure 2.2 Model 400 wind profiler height coverage, gate spacing and height resolution. (From van de Kamp, 1988)

Radar	Tycho DORA 400S wind profiler
Operational Frequency	404.37 MHz
Antenna	Phased Array Coaxial Collinear Dipoles
Antenna Aperture	12m in diameter
Transmitted Peak Power	40 KW
Beam-width	5°

Table 2.1 Model 400 wind profiler basic parameters

One of the major operating procedures is the control parameters setting. These parameters determine the wind profiler performance and should be optimally chosen according to the experimental requirements. Failing to choose these parameters properly can seriously degrade the quality of the data. For example, if the Pulse Repetition Frequency (PRF), the frequency at which pulses are transmitted, is set too high, there are going to be superpositions between echoes from several pulses emitted at different moments and so called "range aliasing" will occur. Also, if the PRF is too high, the velocity resolution will be poor. On the other hand, if PRF is too low, the maximum detectable velocity range is going to be too small and the velocity aliasing may occur. Cox et al. (1992) lists some of these parameters and the corresponding values for the FIRE II experiment.

2.2 Radar Echo Mechanisms

It is important to study the echo mechanisms because only after knowing what a wind profiler receives, can we interpret our observations and successfully retrieve physical and dynamical information of the atmosphere. Gossard et al.(1985) reveals

that the fine scale refractivity structures of the PBL (Planetary Boundary Layer) observed by UHF/VHF radar are closely correlated to the vertical gradients of temperature and wind. Gossard and Frisch (1987) related the reflectivity of radar waves to the atmospheric stability. Summarizing the previous observations and theoretical studies, Rottger and Larsen (1990) gave a brief analysis of three idealized mechanisms, of which no single one is perfectly suited to explain the real observations simply because the received echo is a result of a combination of these mechanisms. The exact physical mechanisms accounting for radar echoes from a clear sky are not clearly understood even after several decades of use. In view of this fact, we will only give a brief review of this complex problem in this section.

A wind profiler mainly receives radar waves scattered and reflected by a clear sky arising from changes in air density which causes variations of refractive index, n. The refractive index changes with air temperature, pressure and humidity according to the following relation (Rottger and Larsen, 1990).

$$n = 1 + \frac{77.6}{T}\left(P + \frac{4810e}{T}\right)\times 10^{-6} - 40.3\frac{N_e}{f_0^2} \qquad (2.1)$$

there, $P(mb)$ and $T(K)$ are the pressure and temperature of the air, respectively, $e(mb)$ is the water vapor pressure, N_e is the number density of free electrons ($1/m^3$), and f_0 is the radar operating frequency in Hz. Generally the equation includes a dry term, a wet term and an ionospheric term, which may be neglected below the mesosphere (Hocking, 1985). In the upper troposphere and stratosphere, the dry term, which is essentially determined by the temperature variation, usually dominates

the changes in n (Rottger, 1990). This equation is only valid for microwave wavelengths that are not near gaseous absorption lines, which means attenuation by the intervening air between the scatterers and the radar can be neglected.

Rottger and Larsen (1990) give three major mechanisms responsible for the clear air echoes. The first one is known as Bragg scattering (isotropic/anisotropic turbulence) which is caused by the randomly distributed and fluctuating irregularities filling the radar volume. The radar received echoes are uncorrelated both vertically and transversely. Bragg scattering can arise from conditions associated with thermal instability, dynamical instability and microphysical processes such as evaporation in a cloud. This scattering is considered to be the most dominant mechanism in the troposphere by Gage (1990), and Gossard and Strauch (1983). The second mechanism is Fresnel reflection. It may be described as the quasi-specular echoes from an isolated layer with sharp gradients of the refractive index. This reflection is transversely coherent and usually associated with stable regions of the free atmosphere. The third mechanism is similar to the reflection mechanism but is used to define those multiple quasi-specular echoes caused by several closely located layers with strong index of refraction gradients. The time-height display of these signals often reveals a vertically random, but transversely coherent pattern. Physically, it is an intermediate mechanism between the above two structures; this mechanism is also called Fresnel scattering. This phenomena has been reported in the ocean and the atmosphere Gage. (1990) presented a sheet-layer model, which contained thin stable sheets of concentrated temperature gradient separated by thicker layers of weak turbulence.

Studying the thin layers with strong radar index of refractor gradients in the PBL, Gossard et al. (1984) gave a theoretical comparison between the contributions to the radar echoes from Bragg scattering and Fresnel Reflection as shown in Figure 2.3. In this figure, they applied a hyperbolic tangent profile for the potential refractive index (right upper corner) and deduced the refractive coefficient, R in Equation 2.2, in a layer of medium with thickness T which has a scale of meters.

$$R = (\Delta\phi)^2(\pi^2 T/\lambda)^2 \sinh^{-2}(\pi^2 T/\lambda) \tag{2.2}$$

where $\Delta\phi$ is the total difference in the potential refractive index of the layer, and λ is the radar wavelength. Confining the Bragg scattering to the same medium layer with the thickness T, Gossard et al. (1984) used a quantity η, the radar reflectivity, multiplied by the depth T to correspond the above reflectivity coefficient, R. In an inertial subrange of isotropic turbulence, this parameter is

$$\eta T = 0.38(T/\lambda) C_n^2 \lambda^{\frac{2}{3}} \tag{2.3}$$

where C_n^2 is the structure parameter of the refractive index.

It can be deduced from Figure 2.3 that the returned power is generally comparable between the reflection and scattering mechanisms when $0.5 < T/\lambda < 0.8$ under those chosen values of $\Delta\phi$ and $C_n^2\lambda^{2/3}$. But once the thickness of the layer is thin enough, the Fresnel Reflection can exceed the Bragg scattering with a fixed

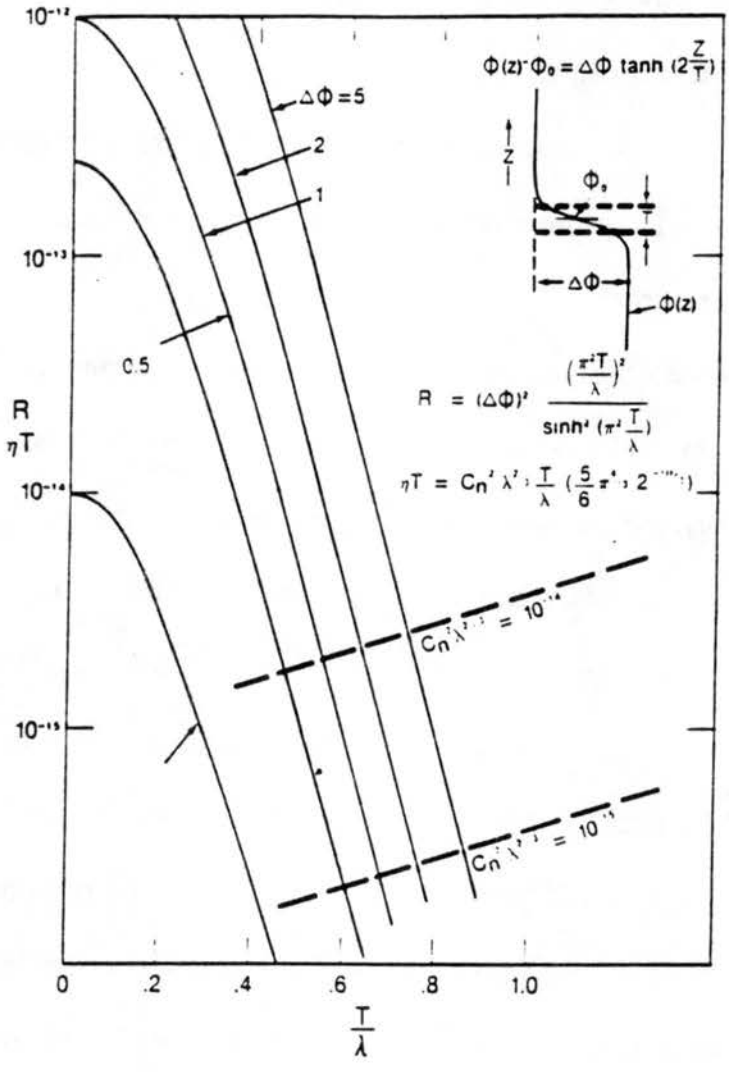

Figure 2.3 Comparison of Bragg scattering with Fresnel reflection derived from a hyperbolic tangent profile of refractive index. (Gossard, et al., 1984)

potential refractive index gradient in the layer. The ratio T/λ in this figure is limited to less than 1.0 which indicates the thickness of the transition layer is several meters, or less if the wavelength is several meters (VHF band). This kind of thin layer is more likely to exist in the PBL than in the free atmosphere. At a wavelength of 75cm, the T/λ can be much bigger than 1.0. Therefore it is expected from this figure that the CSU wind profiler receives echoes mostly from Bragg scattering rather than the Fresnel returns.

Previous observations report that a power maximum is often seen above the tropopause by VHF radars (e.g. Hocking and Rottger, 1983). Layers 50m thick revealing correlations between the maximum radar echo power and strong vertical shear of the horizontal winds are reported by Sato and Woodman (1982) from UHF radar observations of the upper troposphere and lower stratosphere. Rottger and Larsen (1990) suggest that, in the low VHF band, a radar can detect both Fresnel scatter/reflection and Bragg scatter, but a UHF radar can probably detect only Bragg scatter. The received spectrum is usually the superpositions of the Gaussian components, which are partly due to the Bragg scattering from a background of isotropic turbulence and partly due to the beamwidth broadening effects. The non-Gaussian narrow spikes arise from anisotropic turbulence in the radar volumes and Fresnel reflection or Fresnel scattering.

In addition to the scattering and reflection described above which arise from changes in the atmospheric thermodynamic parameters, Rayleigh scattering from small particles, such as rain drops and ice particles, is another potential echo source

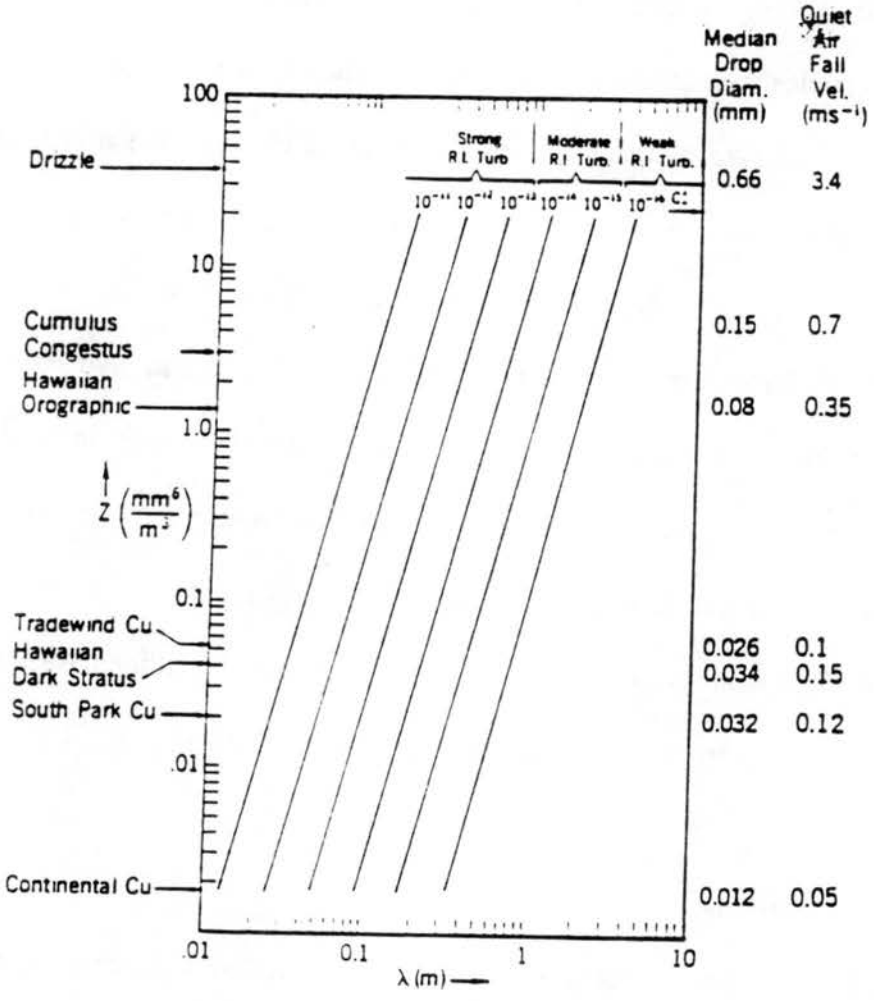

Figure 2.4 Comparison of echoes from Bragg scatter and Rayleigh scatter for various cloud types. Straight lines present equal echo from these two mechanisms. (Gossard, 1990)

for a wind profiler. The relative importance of this scattering can be inferred according to Gossard (1990). Figure 2.4 shows the radar wavelengths where Bragg and Rayleigh scatter are equivalent. For wavelengths larger than 0.7m, Bragg scatter exceeds the Rayleigh scatter from 0.15mm diameter drops. The Rayleigh scatter from ice particles is presumably much weaker than that from the similar size rain drops. Since the size of the ice particles in cirrus clouds have a typical effective radius of 0.05mm with the maximum radius of about 0.150mm, we can assume, for a 75 cm wavelength, the Rayleigh scatter from the cirrus cloud ice particles is much weaker than the scattering/reflection due to the air refractive index change. However, during the FIRE II experiment, the radial velocities measured by the vertical beam of the wind profilers revealed correlations with cirrus clouds. Does this mean that Rayleigh scatter from ice particles is important or that increased small scale turbulence is inherently present in cirrus clouds? In either case, the Doppler velocity obtained from a vertical beam should be used cautiously.

2.3 Signal Processing

The primary signal processing procedures included: Coherent averaging (time domain averaging); DC (Direct Current) removal; FFT (Fast Fourier Transform); Non-coherent averaging (spectral domain averaging); Ground clutter removal; Noise estimation and Moments calculation (Figure 2.5). After these procedures were applied, spectra (Figure 2.6) are obtained and radial velocities are calculated from the averaged Doppler shift. Power and velocity variance are the zeroth and second

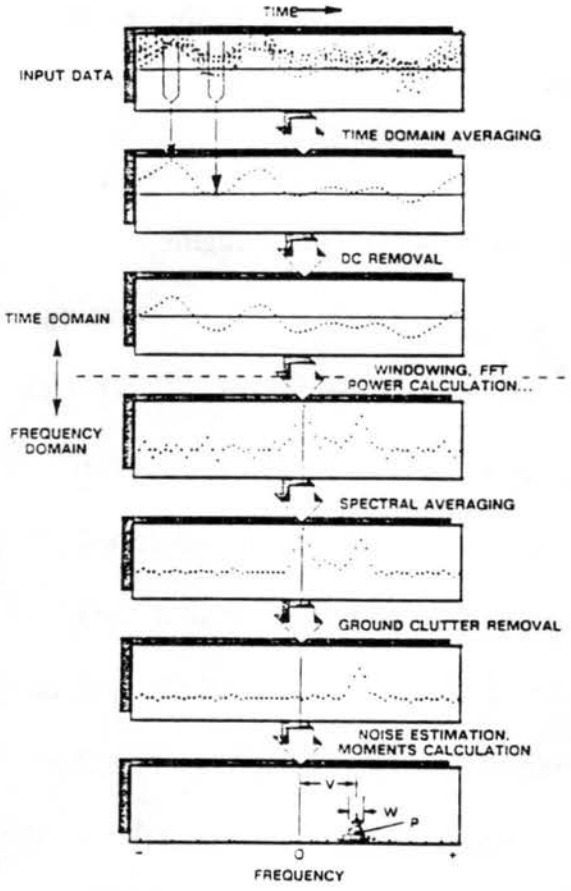

Figure 2.5 The signal processing steps for the CSU wind profiler. (Peterson, 1988).

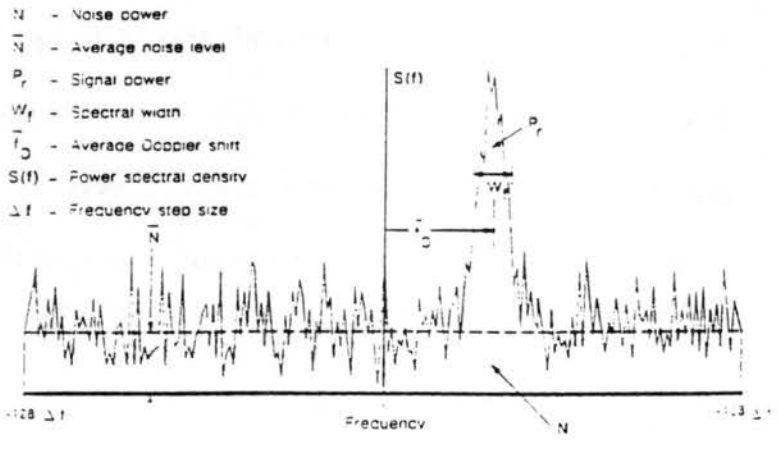

Figure 2.6 A typical signal power spectrum of a wind profiler. (Peterson, 1988).

moments, respectively, and are also calculated. In this section, these procedures are briefly described.

2.3.1 Coherent averaging and non-coherent averaging

Coherent averaging, also called time-domain averaging, takes the mean of a certain number of consecutive samples before the FFT is performed. Non-coherent averaging takes the mean of several consecutive spectra resulting from FFT calculations. The main purpose of averaging is to decrease the random noise from the cosmic background and the wind profiler system itself. In addition, coherent averaging reduces the computational load of the FFT processing. But if too many data sequences in the time-domain are averaged (i.e. parameter NCOH (or TDA) is large), it may cause velocity aliasing due to the small threshold of unaliased velocity (Peterson, 1988).

2.3.2 Noise estimate

It is of practical importance to know the spectral power density level below which the spectrum is dominated by noise from the atmospheric background and radar system. This power density level is referred as the noise-level or the noise-threshold. The noise-level estimation of the CSU wind profiler adopts the ideas of an objective method by Hildebrand et al. (1974). In this method, it is assumed that the atmospheric signal has a colored Gaussian property, and the signal due to the radar and background noise has a white Gaussian spectrum. Then it makes use of

the property that a white Gaussian spectrum has a constant variance which depends only on its frequency span. A series of increasing thresholds is applied to reject any spectral value larger than the arbitrarily assigned threshold until the modified spectrum satisfies the white noise condition $\sigma_N^2=F^2/12$ where σ_N is the variance and F is the frequency span.

2.3.3 Ground clutter signal removal

Since the ground clutter signal strongly affects data quality, especially in the vertical beam, this section introduces three methods applied to the CSU wind profiler data. These methods are the Linear Algorithm, Exponential Algorithm and Half Plane Subtraction method (Tycho Tech.,Inc., 1989). For reasons to be discussed later, the first two interpolation methods are recommended.

-Linear Algorithm

A typical ground clutter signal is shown in Figure 2.7. To remove this strong signal return centered at zero frequency shift, a window of width N is chosen with zero central frequency. The values inside of this window are removed and are linearly interpolated from the values at points f_A and f_B. Any point C between A and B is equal to:

$$P_C = P_B + (f_B - f_C)*k, \qquad k = \frac{P_A - P_B}{N} \tag{2.4}$$

-Exponential Algorithm

This method is similar to the above method, but instead of using a linear interpolation, an exponential interpolation is applied. The slope of the line AB is defined as

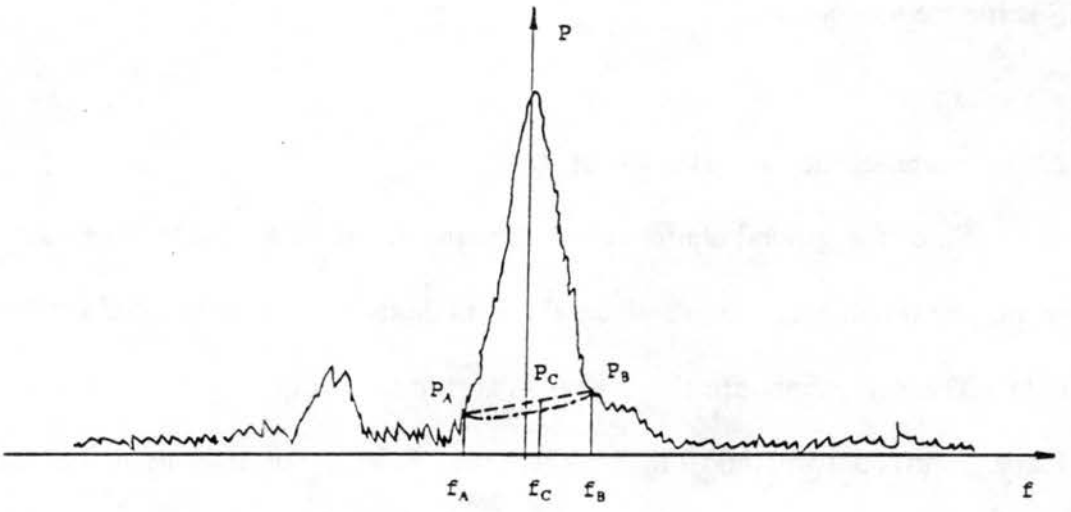

Figure 2.7 Schematic diagram of the linear and exponential interpolations.

$$k = \frac{\log A - \log B}{N}. \tag{2.5}$$

The power at any point C is calculated by

$$P_C = e^{\left(kf_C + \frac{\log A + \log B}{2}\right)}. \tag{2.6}$$

Substituting k into the above equation, the interpolated value at point C is:

$$P_C = e^{\left(\frac{f_C}{N} * \ln\left(\frac{P_A}{P_B}\right)\right)} * e^{\ln\sqrt{P_A P_B}} = \left(\frac{P_A}{P_B}\right)^{\frac{f_C}{N}} * \sqrt{P_A P_B} \qquad (2.7)$$

-Half Plane Subtraction Method

This method is based on the assumption that the clutter signal is perfectly symmetrical about the zero frequency point. The negative frequency side is subtracted from the positive frequency side and the result defines the value of P according to the following:

if $P_+ - P_- \geq 0$ then $P_+ = P_+ - P_-$ and $P_- = 0$
if $P_+ - P_- < 0$ then $P_+ = 0$ and $P_- = P_- - P_+$

With this method, if a noise spike is detected at a position symmetric to a weak signal peak, some noise spikes may then be chosen as the signals by mistake. Also the clutter signal may not be symmetric about zero frequency.

The above methods are generally based on the assumption of certain symmetry of the clutter signal, especially the Half Plane Subtraction Method. In an idealized case, the signals from both the meteorological echoes and clutter echoes have Guassian distribution. One-Gaussian-function or multiple-Gaussian-distribution least-square fitting algorithms could be used in this case. As we noticed, there are large uncertainties of the statistical properties of the clutter signals, which strongly affect the efficiency of any clutter removal algorithms. The methods used in our program are very empirical. To improve the algorithm results, it is strongly recommended that statistical studies of clutter signals under different environments

be performed, in addition to minimizing clutter echoes by improving hardware designs.

2.3.4. Calculations of Radar Moments

Three moments are calculated from each spectrum. The signal power return (the zeroth order moment) is the sum of the area in the signal peak. The averaged Doppler shift of the peak (the first order moment) is the weighted average, by the signal power, of the Doppler shift values as shown in the following equation:

$$\overline{V} = \frac{\sum_{i=m}^{n} (P_i \cdot \Delta f_i)}{\sum_{i=m}^{n} P_i} \cdot \Delta v \qquad (2.8)$$

Here, m and n are the indices at which the peak first reaches the noise level at the right and left side, respectively. P_i is the power value at the Doppler shift point Δf_i , and Δv is the velocity resolution. This averaged Doppler shift gives the radial velocity for each beam. The positive value denotes air moving toward radar.

The second order moment is the variance which represents the fluctuations in the velocity distributions and is given as

$$\sigma = \left[\frac{\sum_{i=m}^{n} (P_i \cdot f_i^2)}{\sum_{i=m}^{n} P_i} - \left(\frac{\sum_{i=m}^{n} P_i \cdot \Delta f_i}{\sum_{i=m}^{n} P_i} \right)^2 \right] \cdot (\Delta v)^2 \qquad (2.9)$$

where, the symbols have the same meaning as those in equation (2.8).

In general, the signal spectra are assumed to have a Gaussian distribution, however some factors, such as the velocity distribution in the pulse volume (Keeler, 1990), can cause non-Gaussian distributions in which the asymmetric spectra and multimode spectra have been observed. Therefore, a more general method to describe the signal spectra may be desirable. Keeler (1990) gives a brief view of different methods applied to the spectral moment estimations in both frequency and time domain.

2.4 Wind Field Calculation

Radial velocity measurements are collected at each range gate along each wind profiler beam. For each range gate, the vertical wind velocity is simply deduced from the radial velocity of the vertical beam in the sense of the direct measurement. However, from the discussions in Chapter 3, we find that the real situation is very complex and the direct utilization of these data as the vertical velocity needs more careful consideration. Two indirect calculations of vertical wind velocity from other atmospheric parameters will be developed in Chapter 3 and their results will be compared with the direct measurements.

The horizontal wind velocity calculation is generally more reliable than the directly observed vertical velocity, and is based on the radial velocities from two orthogonal oblique beams and the known vertical velocity either from the direct measurement or one of the indirect methods. For example, if one chooses east and

north beams, the zonal wind, u, and meridional wind, v, can be calculated from following equations:

$$u = -\frac{V_{re} + w\cos\theta}{\sin\theta} \qquad v = -\frac{V_{rn} + w\cos\theta}{\sin\theta} \tag{2.10}$$

Here, V_{re} and V_{rn} are the east and north beam radial velocities. w is the vertical velocity. θ is the zenith angle. Compared with horizontal velocities, the vertical velocity is usually much smaller and may be assumed to be zero in the above equation. However, large bias can be caused when the real vertical velocity is significantly non-zero.

As mentioned in the Appendix A, the orthogonal beams are usually not pointing directly east(west) and north(south), but are rotated clockwise at angle ϕ, and the zonal and meridional winds (u, v) from Equation(2.10) must be adjusted; the corrected winds (u',v') are

$$u' = u\cos\phi + v\sin\phi \qquad v' = -u\sin\phi + v\cos\phi \tag{2.11}$$

In the above four sections, we gave a general view of model 400 wind profiler in the terms of its echo mechanisms, signal processing and retrieval of atmospheric wind field. In the next section, we will discuss frequency response of a wind profiler to clear air turbulence.

2.5 Wind Profiler Performance in Detecting Clear Air Turbulence (CAT)

It is generally accepted by the radar community that the Bragg turbulence scattering predominates the echo characteristics, however the Fresnel returns are

sometimes dominant for longer wavelength radars (Gossard, 1990; Gage, 1990). In this section, a theoretical study of the radar performance for detecting CAT rather than the turbulence's statistical characteristics will be given. This process is based on turbulent kinetic energy (TKE) spectra and the radar frequency response. As discussed in the previous section, the interpretation of the radar echoes is still not well understood, therefore the radar performance is investigated by assuming the only radar echo mechanism is Bragg scatter.

Figure 2.8 depicts a one-dimensional energy spectrum of the velocity perturbations showing the existence of the refractivity perturbation in an inertial subrange under CAT and quiescent atmosphere situations (Atlas et al., 1966). As the CSU and NOAA wind profilers use a wavelength of 75cm, the one-half wavelength falls into the lower inertial subrange, indicating our studies of the turbulence spectrum maybe based on the inertial subrange turbulence theories. Instead of using a three-dimensional refractivity spectrum, an equilibrium one-dimensional refractivity spectrum of isotropic homogeneous turbulence was applied by Atlas et al. (1966). The following analyses seeks an optimum wavelength estimation of a radar for detecting CAT.

Atlas et al. (1966) studied the radar wave reflectivity of a CAT region by applying the reflectivity equation of a refractively turbulent medium (originally from Tatarski, 1961) which is given as

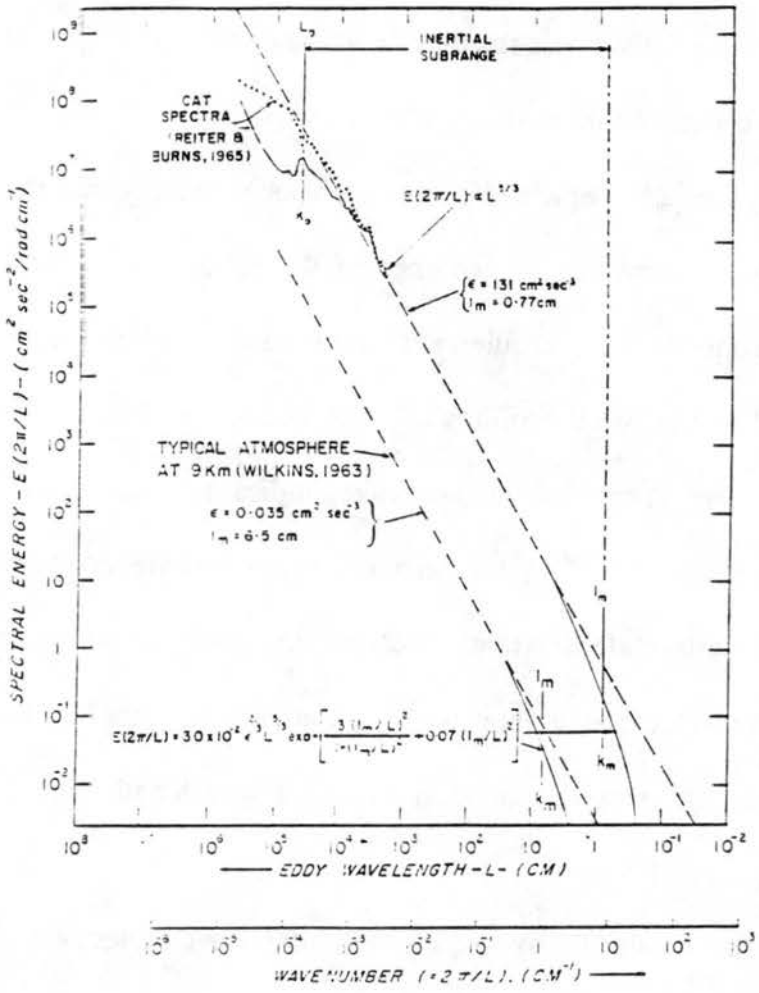

Figure 2.8 One-dimensional kinematic energy spectral of CAT regions and of quiet atmosphere in the inertial subrange (Atlas et al., 1966).

$$\eta = \frac{\pi \sin^2\beta \overline{(\Delta n)^2} k^2 F_n(k)}{\left[8\sin^4\left(\frac{\theta}{2}\right)\right]}, \tag{2.12}$$

where

θ -- Angle between the transmitter and receiver beams. For our wind profilers, $\theta=\pi$

β -- Angle between the direction of the receiver and that of the electric field of the incident wave.

k -- Wavenumber, $k=2\pi/\lambda$

λ -- Wavelength

$(\Delta n)^2$ -- Mean square fluctuation in refractivity

$F_n(k)$ -- One dimensional spectral density of $(\Delta n)^2$, which has a wide distribution over k, however, concentrates at wavenumber $k=4\pi\sin(\theta/2)/\lambda$ or scale $L=\lambda/[2\sin(\theta/2)]$. When $\theta=\pi$, L is the one-half of the wavelength which explains why radar receives backscattering preferentially from irregularities of a size about one-half the radar emitting wave's wavelength.

Tatarski (1961) gives a simplified expression of $F_n(k)$ which is modified by an empirical function $\gamma(\chi)$ to accomplish the extrapolation beyond the small-scale limit of the inertial subrange:

$$F_n(\chi) = \frac{2}{3}\chi_0^{\frac{2}{3}}\chi^{-\frac{5}{3}}\gamma(\chi) \tag{2.13}$$

where, $\gamma(\chi)=exp[-(1.3\chi^2)/(1+\chi^2)-0.07\chi^2]$, $\chi=k/k_m$, $\chi_0=k_0/k_m$, $F_n(k)=F_n(\chi)/k_m$ and k_0, k_m are the wavenumbers at out-scale L_0 and limiting scale (or, inner scale) l_m, respectively.

Substituting into Eq.(2.12), the final expression of the radar reflectivity at $\theta=\pi/2$, $\theta=\pi$ (so, $k=4\pi/\chi$) is:

$$\eta = 2.07\overline{(\Delta n)^2}L_0^{-\frac{2}{3}}l_m^{-\frac{1}{3}}\left(\frac{\chi}{2}\right)^{\frac{1}{3}}\gamma(\chi). \tag{2.14}$$

From the relation between the normalized one-dimensional refractivity spectrum and three-dimensional refractivity spectrum (Hardy et al.,1966),

$$\overline{(\Delta n)^2} = 0.19L_0^{\frac{2}{3}}C_n^2 \tag{2.15}$$

Here, C_n^2 is the structure parameter of the refractive index which represents the variability of n in the inertial subrange. So, the radar reflectivity is derived as,

$$\eta = 0.3933C_n^2\left(\frac{\chi}{2}\right)^{\frac{1}{3}}l_m^{-\frac{1}{3}}\gamma(\chi). \tag{2.16}$$

Hardy et al (1966) and Ottersen (1969a,b) obtained a similar expression except that they did not use the modification function $\gamma(\chi)$. A group of clear air reflectivity spectra are calculated using Equation(2.16) under various inner scales l_m and

structure constants C_n^2 as shown in Figure 2.9, where the dotted, dotted-dash, solid and dash lines represent the reflectivities for the severest, severe, moderate and weak turbulence, respectively. This figure, indicates that the reflectivity is not a monotonic increasing function of wavelength even though the energy spectrum in Figure 2.9 shows the monotonic increasing property in the inertial subrange. Instead, we have the strongest reflectivity at the wavelength close to the inner scale l_m with consistent large η between 1cm and 10cm, and a slow decrease at longer wavelengths with a very deep decrease at η<1cm. The reflectivity, however, does increase with C_n^2. The straight dashed line in Figure 2.6 is the reflectivity spectrum of a cirrostratus cloud, based on the data of Plank et al. (1955), for which there is a -4th power relation.

Considering the maximum sensitivity as a function of wavelength for a radar system, Atlas et al.(1966) studied the minimum detectable reflectivity by the radar equation for distributed targets:

$$\eta_{min} = \frac{8\pi P_{min} r^2}{0.445 \cdot P_t \psi A_e h \cdot 10^{-2L}} \tag{2.17}$$

where,

P_{min}-- the minimum detectable echo power. Pmin=NKTB, and N is the receiver noise figure, K is Boltzmann's constant 1.38×10^{-23}N/K/Hz, T is the temperature in Kelvin and B is the receiver bandwidth in hertz.

Pt -- Peak transmitter power.

Ae -- Effective antenna aperture which is equal to $\lambda^2 G/4\pi$, here, G is the antenna gain.

ψ -- Fraction of the beam filled.

L -- Losses in wave guide and RF components in decibels.

r -- Range between the target and radar antenna.

h -- Pulse length in space.

Using a one-meter diameter antenna of an airborne radar, Atlas et al. (1966) described the minimum detectable reflectivities, with and without maser amplifiers, which are shown by the two lines in the upper half of Figure 2.9. The lines show that, at the range r=18.5km, only the most reflective CAT ($C_n^2=10^{-14}cm^{-2/3}$) can be detected by maser receivers under a limited antenna size and the possibility of detecting CAT at wavelengths less than 2cm is extremely small as η_{min} and η spectrum diverge rapidly in the millimeter region.

Figure 2.10 is the ratio of η_{cat}(l_m=1.0cm, $C_n^2=10^{-15}cm^{-2/3}$) to η_{min}. The amplitude shows that it is impossible for this radar to detect such moderate turbulence as there is an 10dB improvement required, which can be achieved using coherent adding processing or increasing the antenna size without changing the major character of the spectrum. Despite this problem, the shape of the curve in Figure 2.10 suggests that the wind profiler frequency of 403 MHz is reasonably well suited to detect CAT. Noticing that the reflectivity of a cirrus cloud drops dramatically as the turbulence scales increase, Atlas et al. (1966) suggests 5cm-6cm as the optimum wavelength in order to give radar a good potential for detecting both CAT and cirrus clouds turbulence.

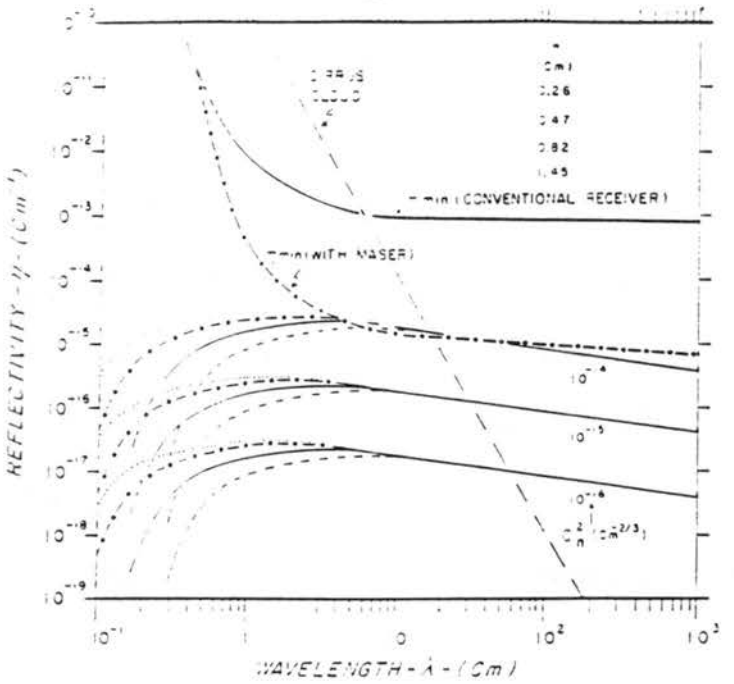

Figure 2.9 Lower half represents clear air η for various l_m and C_n^2 values expected in CAT. Upper half shows the minimun detectable η of a typical cirrus cloud. (Atlas et al., 1966)

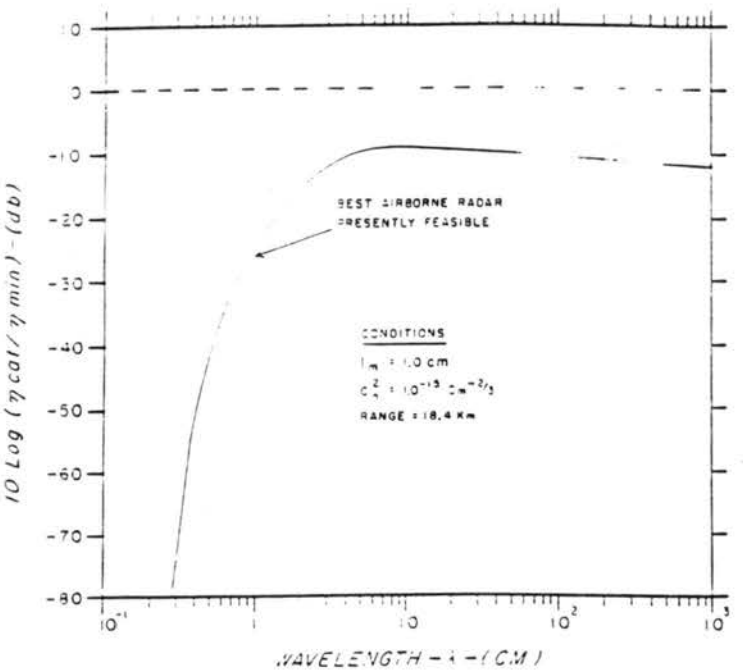

Figure 2.10 Ratio of CAT reflectivity to the minimum detectable reflectivity of an airborne radar.

It is obvious that the one-half wavelength of CSU and NOAA network wind profilers, which is about 37.5cm, is far removed from the optimum wavelength derived above for detecting CAT and cirrus cloud turbulence.

In Figure 2.9, we can also see a comparison between the reflectivities of CAT and cirrostratus clouds. At our 75cm wavelength, the reflectivities of strong and moderate CAT ($C_n^2 = 10^{-14}$ and 10^{-15}, respectively) are stronger than that from a typical cirrostratus cloud. However, when turbulence is weak ($C_n^2 = 10^{-16} cm^{-2/3}$), there is not much difference between the two reflectivity values.

Chapter 3

COMPARISON OF VERTICAL VELOCITY ANALYSIS TECHNIQUES

Before the advent of wind profilers and other Doppler radars in the 1970's, vertical velocities were commonly deduced from methods that relied on other atmospheric parameters. These methods include the kinematic method, the adiabatic method, and the use of omega equation. However due to the uncertainties of the direct radar techniques discussed below, much work has been done in the last decade to compare the direct measurements with other methods for different meteorological cases (e.g., Larsen et al., 1991a, b). In this chapter, we are going to study the vertical velocity fields of the cirrus cloud case on Nov. 26, 1991. The vertical velocities were obtained from direct measurements of the vertical radial velocity; indirect calculations were derived from the quasi-VAD technique based on the CSU five-beam wind profiler and the kinematic method using horizontal winds measured of three or four wind profilers. These three methods effectively take advantage of the high temporal and spatial resolutions of the wind profilers rather than using the lower resolution NWS rawinsonde data. With the higher resolution, smaller scale atmospheric dynamical features are expected to be detected.

3.1 Methods and Observations

In the following analysis, an interpolation technique is required to account for bad and missing data. The bivariate interpolation method developed by Michael

Pernice of NCAR's Scientific Computing Division, based on Akima (1978; 1984), was applied to the direct measurements of CSU wind profilers, NOAA network wind profilers and the quasi-VAD method. A four-point Lagrangian interpolation was applied to the kinematic method. Data quality control was also applied to the CSU wind profiler data.

3.1.1 Direct Doppler Method(DDM)

The Direct Doppler Method utilizes the spectral mean radial velocity of the vertical beam as the vertical velocity. However, from the past experimental studies (e.g., Rottger and Larsen(1989)), it was noted that there are many concerns about the uncertainties in the direct measurements. First, since a radar wind profiler measures the motions of refractive index irregularities, a main concern has been on whether the refractive index structure follows the wind field and on what spacial and temporal scales is this assumption valid. Even though previous assessments of the horizontal wind profiling show that the refractive index motions do follow the wind field (Rottger and Larsen, 1989; Larsen et al., 1991b), some investigations (eg. Larsen et al., 1991b) on vertical velocities have suggested the refractive structure is not moving with the air motion. Larsen et al. (1991b) suggests that this situation could occur when a wave is propagating through the measurement area.

A nonvertical beam may cause a large bias in the measurements by introducing a projection of the horizontal winds on the vertical beam. This contribution from the horizontal winds can be very large since vertical velocities are generally weak in comparison to horizontal winds. For example, if there is a 0.25°

offset from the vertical, a 30m/s horizontal wind can add a component of 13cm/s to the vertical velocity. For a typical cirrus cloud case, this can cause a 100% or greater error in the vertical wind measurements. This error can be even more significant when the wind changes directions frequently, however, it is possible to mitigate this effect by calculating a correlation function between the horizontal wind and vertical wind. By applying a VHF radar with wavelength in the order of meters, Larsen et al. (1991a) found that a nonhorizontal refractive layer can introduce errors in the vertical beam measurements, called the aspect sensitivity effect. Since the strongest echoes are received from an off-vertical direction (1°-2°), radial velocities of the vertical beam are not purely vertical components but have significant contributions from the horizontal wind field. Larsen and Rottger (1991) introduced a correction method by finding the incidence-angle from a "standard spaced antenna technique". Their work showed corrections of 5%-200% in the magnitude of the vertical-beam velocity. The corrected vertical velocities were more consistent with the meteorological conditions. However, the dynamic causes of this nonhorizontal refractivity layer is not yet clear (Larsen and Rottger, 1991) and the spaced antenna method is beyond the capability of a single wind profiler in our case study. There are other concerns about the bias in the measurements from influences such as precipitation, lightning, etc. For more details about the biases, refer to Rottger and Larsen (1989) which gives an extensive review of presently known sources of biases in the Direct Doppler Method.

In the FIRE II experiment, the CSU wind profiler, which has a 25cm/s velocity resolution of the vertical beam, found that the meteorological signals of the vertical

beam were often obscured by the central peaks (zero Doppler shift) which had previously been considered as the echoes from ground clutter. The clutter signal, in these cases, is usually 12dB stronger than the real meteorological signal, so that vertical-beam velocities are barely distinguishable even when there are strong vertical air motions. In this application, we expected to find the upward/downward motion tendency by assuming the clutter signal is symmetric to the zero velocity point and that only the real meteorological echoes cause the asymmetry. The positive (negative) asymmetry is considered to be caused by downward (upward) motions. The reason that we use the word "tendency" is that the power-weighted average will greatly lessen the real velocity due to the much stronger central peak, and only relative velocities can be discerned from the data in this case.

The signal processing algorithms used for the CSU wind profiler were tested with and without the ground clutter removal (GCR). Figures 3.1(a) and (b) show the power values of the central peaks for the vertical beam and the east beam without the ground clutter removed. The shaded areas have relative power values larger than -5dB. There are temporal oscillations of signal power at three layers, 12.25km, 10km and 8.25km for the vertical beam, and 11.75km, 9.75km and an estimated 7.75km for the east beam. After removing the ground clutter using a window of width 2 (GCNUM=1), the central peak power values of the vertical beam (Figure 3.1(c)) show the same structures as the real meteorological signals from the oblique beams such as of the east beam (Figure 3.1(d)). The other three beams, (not shown) exhibit the same features. The similar characteristics shown in the time-height plots of the

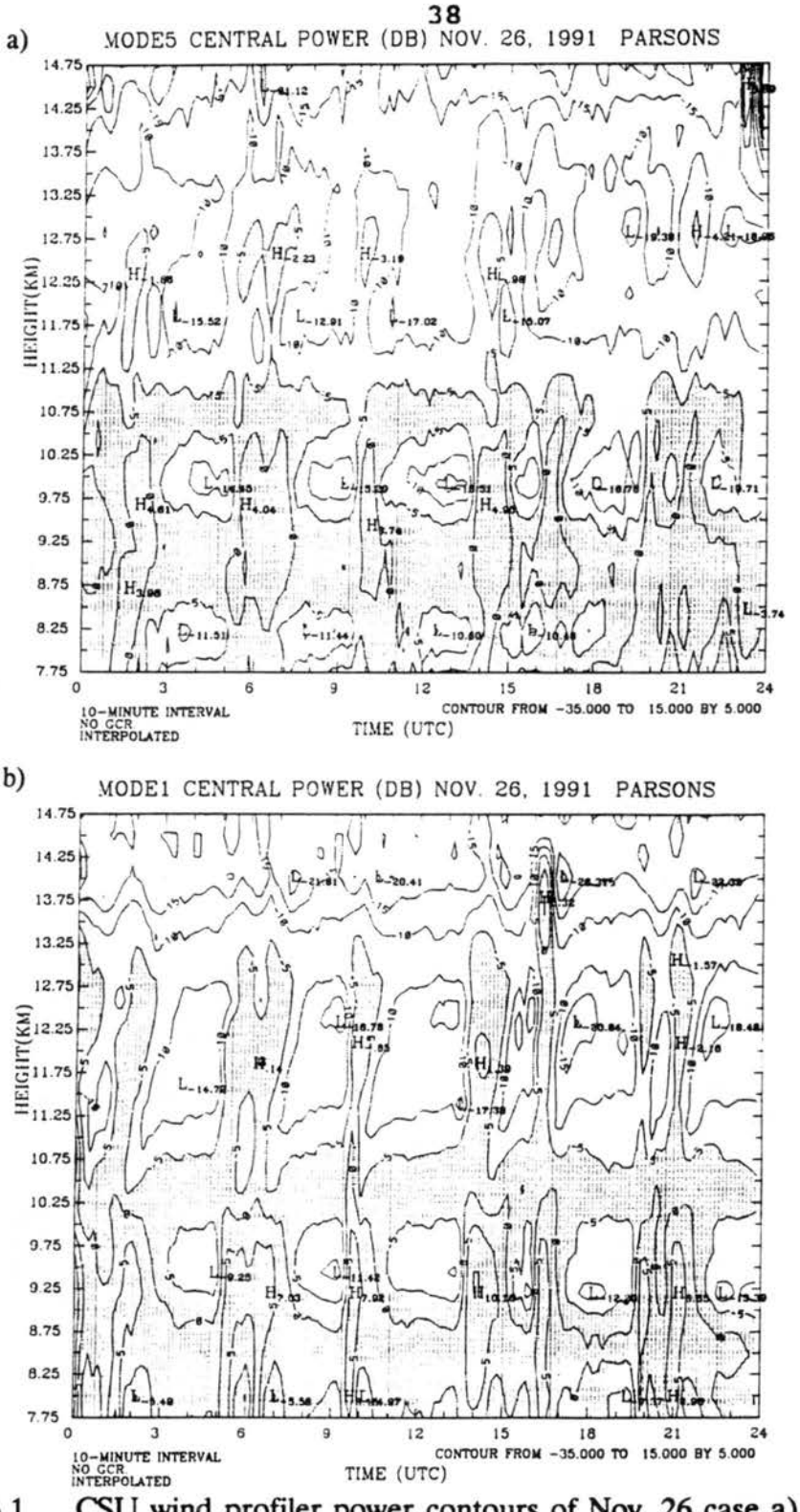

Figure 3.1 CSU wind profiler power contours of Nov. 26 case a) of the vertical beam without GCR (Ground Clutter Removal), b) of the east beam without GCR, c) of the vertical beam with the GCR, and GCNUM=1, d) same as c) but of the east beam.

c)

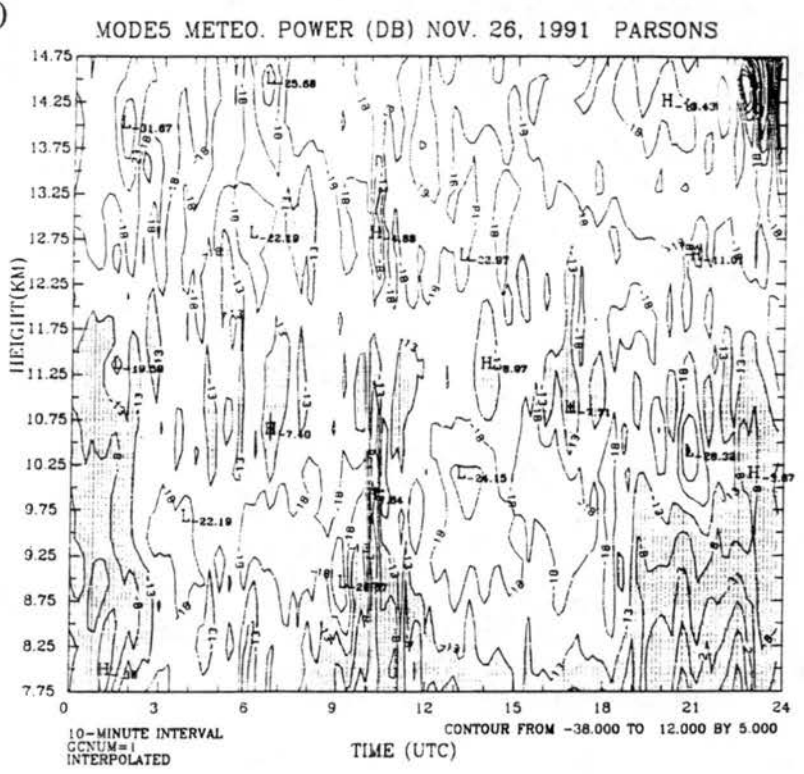

d)

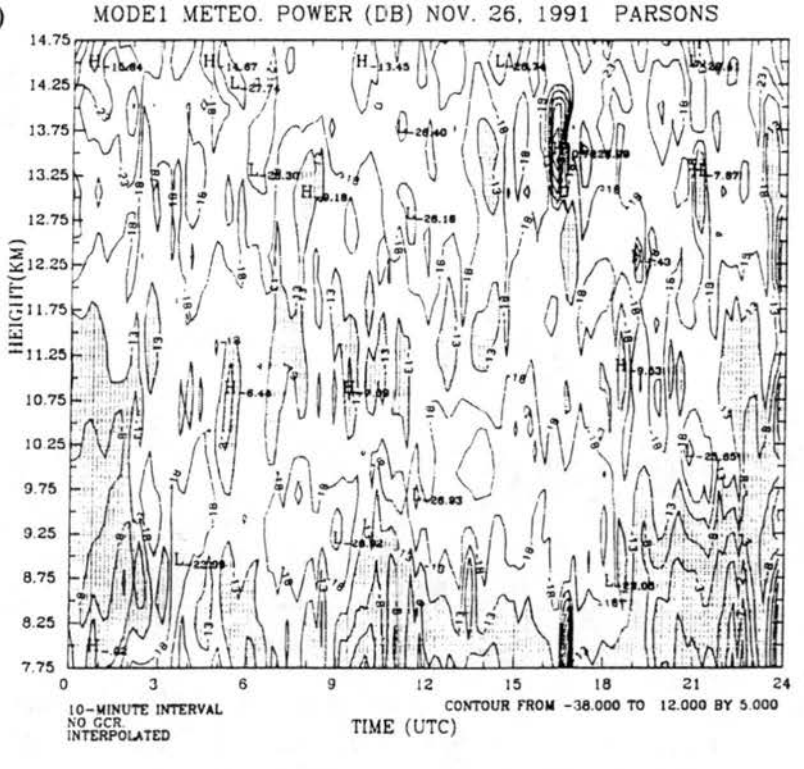

Figure 3.1 continued.

meteorological echoes received by the NOAA network wind profilers at NDS(Neodesha, KS) and HBR(Hillsboro, KS) (Figure 3.2) give one more confidence in the results using the ground clutter removal technique. However, the obtained vertical velocities are still relative values, and may vary with the change of the window width value and velocity resolution. This is one of the major reasons to achieve raw spectra. More details about the structure of the observed meteorological echoes will be discussed in chapter 5.

Since ground clutter does not usually change its scattering properties as a function of time, there must be an atmospheric refractive structure at near zero velocity to generate the oscillating structure of the central peak power return as shown in Figures 3.1(a), (b). Figures 3.3(a) and (b) show the time-height plots of the 10-minute cycle vertical velocity from the CSU wind profiler with and without the ground clutter removal technique, respectively. Shaded areas indicate the upward motion. The plot with the ground clutter removal generally has finer or smaller scale motions than that without the ground clutter removal. It is suspected that the strong "clutter" signals in the upper troposphere are produced by reflection from strong reflectivity gradient layers.

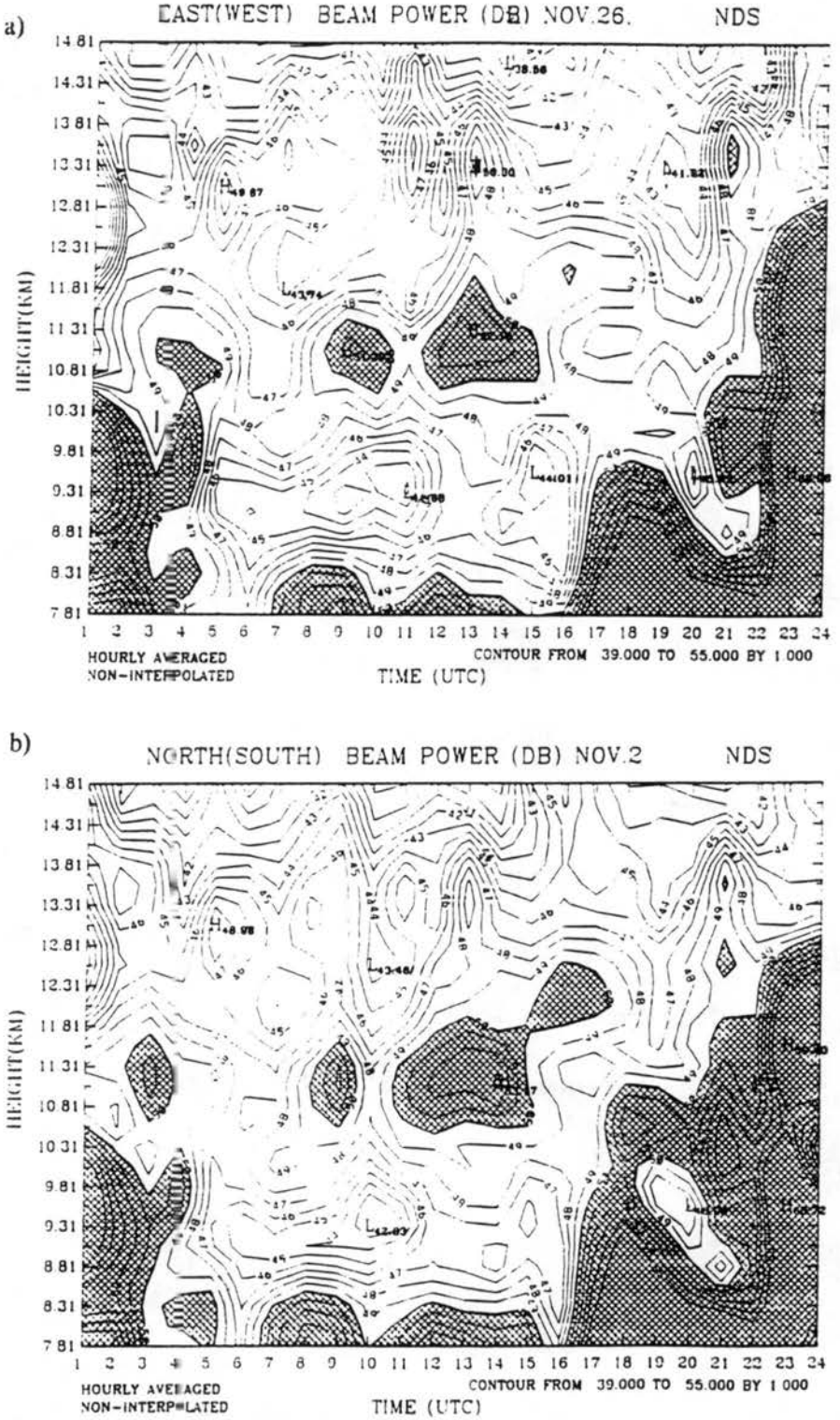

Figure 3.2 Metecrological signal received by NDS and HBR wind profilers of a) & d) east beam, b) & e) north beam, c) & f) vertical beam. Shaded areas present relative power values bigger than 50dB. Data are hourly averaged. 1dB contouring interval.

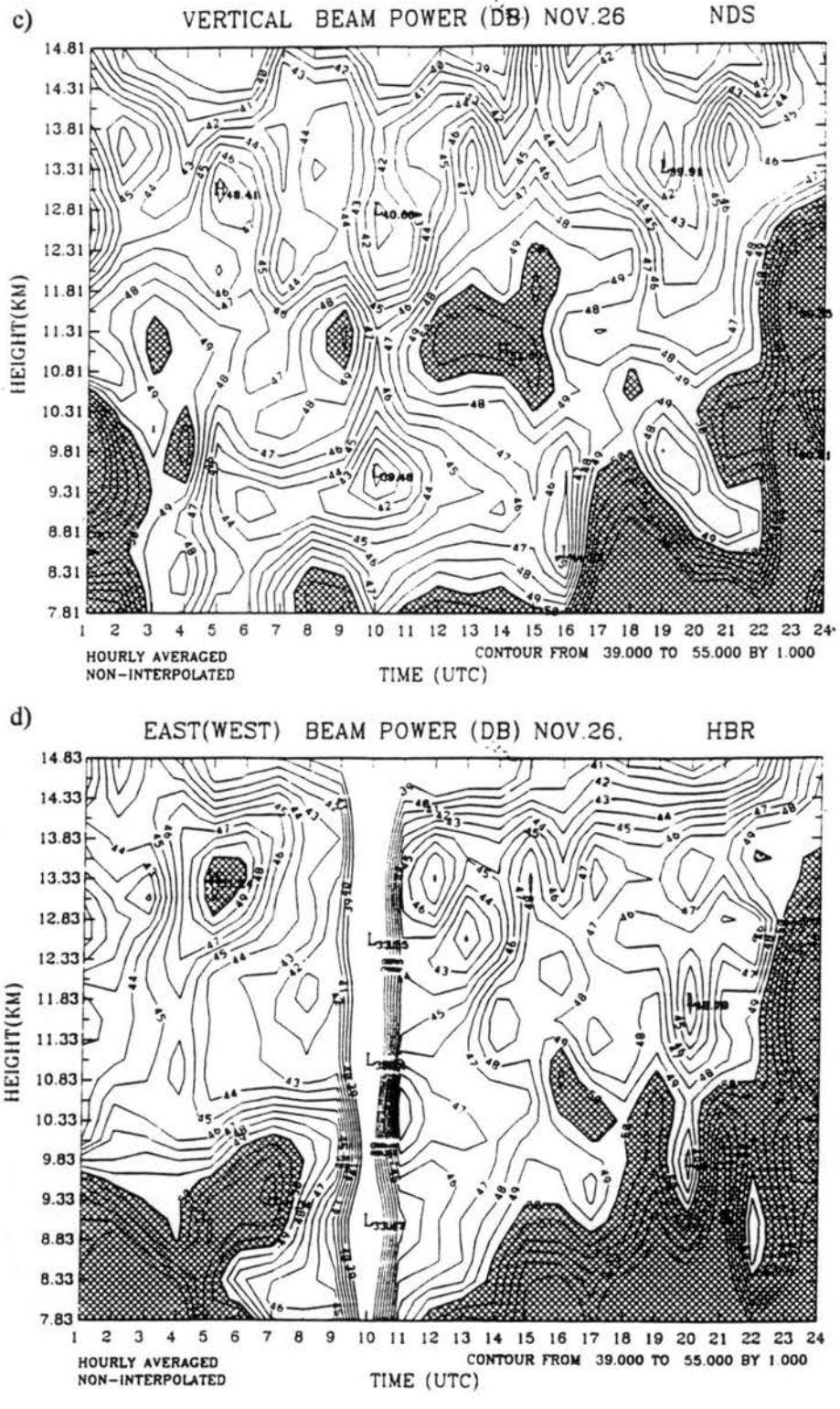

Figure 3.2 continued

e)

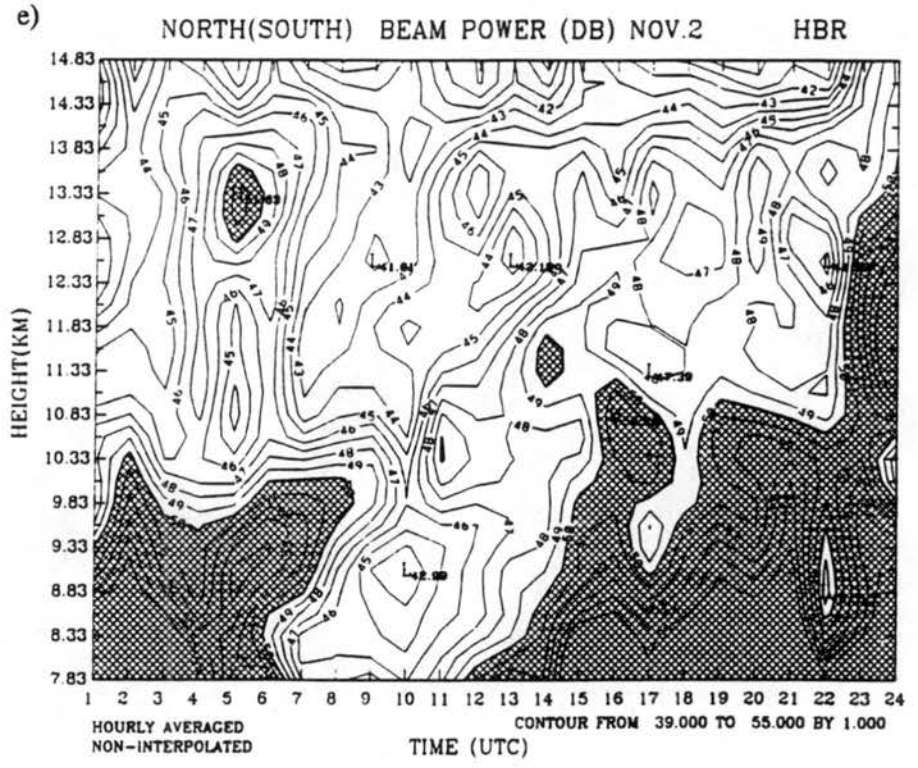

f)

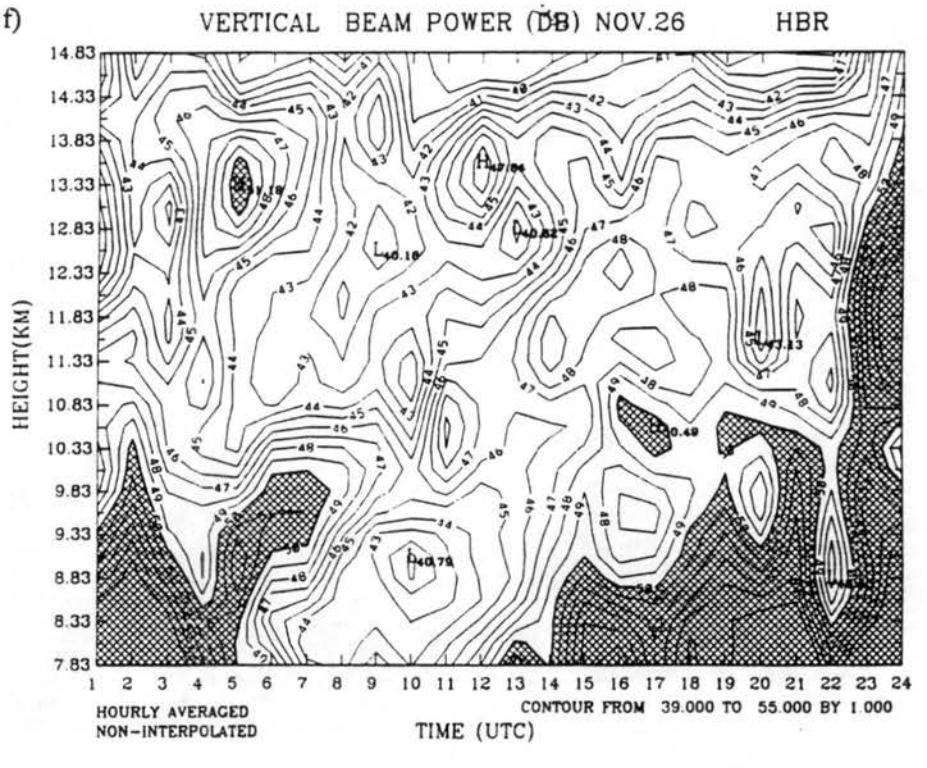

Figure 3.2 continued

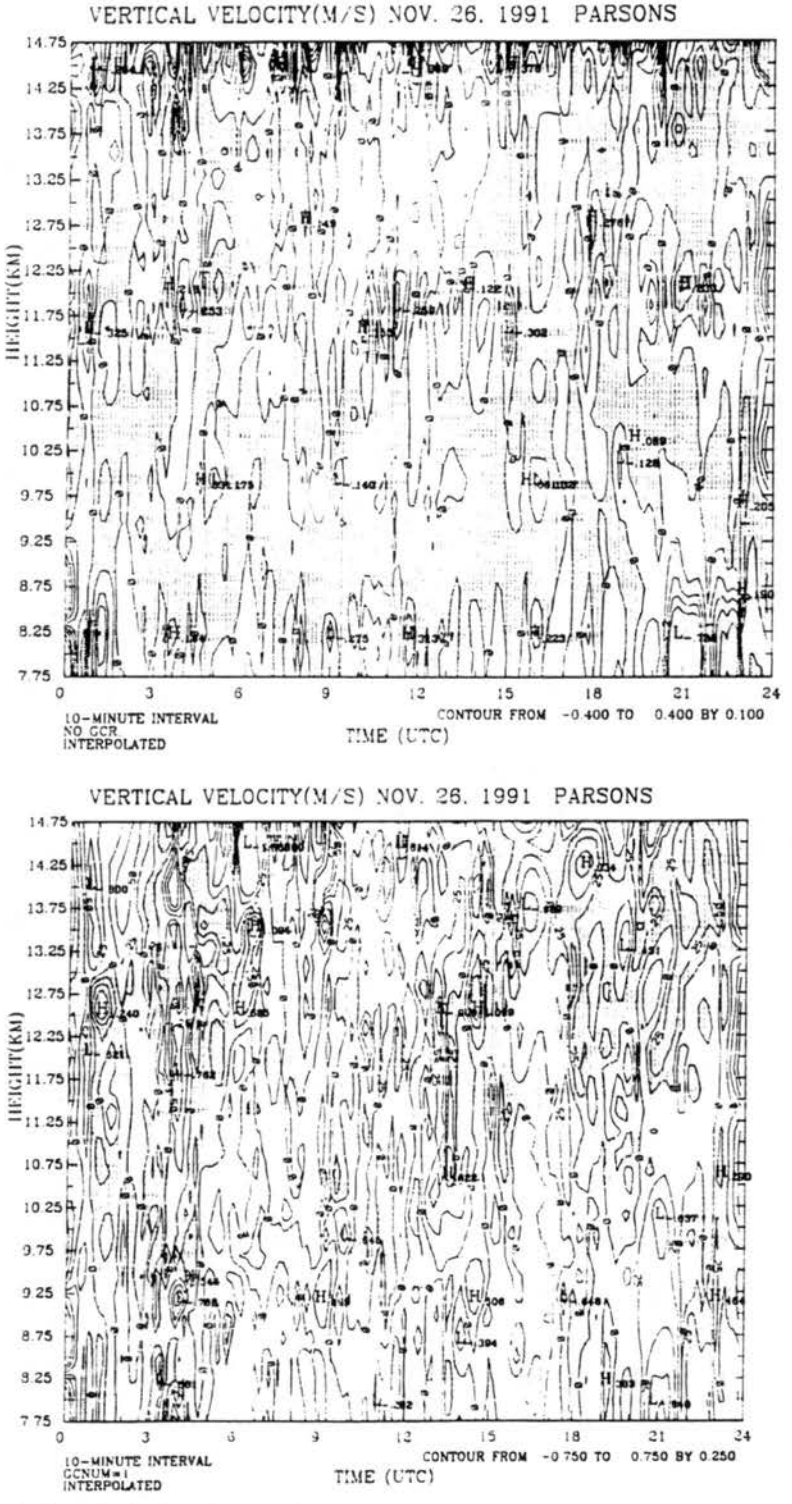

Figure 3.3 Time-height plots of the 10-minute cycle vertical velocities from CSU wind profiler. a) without GCR (Ground Clutter Removal), b) with GCR. Shaded areas are upward motions. 0.1, 0.25 m/s contour intervals for the plot without and with GCR, respectively.

Figure 3.4(a) and (b) show the 0-12Z, 12-24Z and daily averaged profiles of the vertical velocities deduced with and without using ground clutter removal.

The NOAA wind profiler network has been assumed to have better spectral resolution (no exact number is presented in their routine records) and less clutter peak problems. If this is the case, the profiler network averaged radial velocity of the vertical beam may be more accurate, assuming their other operational properties had been same as or better than those of the CSU wind profiler. The 6-minute cycle vertical air motions of a NOAA network wind profiler at NDS(Neodesha, KS) the closest station to the Parsons experiment site, is plotted in Figure 3.5. The temporally averaged profiles at NDS are plotted in Figure 3.6 for the whole atmosphere layer. Comparison between Figure 3.4 and Figure 3.6 indicates the agreement between ground-clutter-removed vertical velocity profiles from the CSU wind profiler and measurements from NOAA wind profiler at NDS. Both measurements exhibit a generally weak vertical motion with varied signs during the period of 00-12Z and a larger vertical motion with nearly consistent negative sign (descending) in the whole upper troposphere during the period of 12-24Z.

One of the major concerns discussed previously, the misaligned vertical beam, should be detectable from a correlation between horizontal and vertical radial velocities. There is a linear relation between the vertical beam radial velocities and one or both of the oblique beam radial velocities if the vertical beam is off from the vertical. The u-w and v-w plots based on the 24-hour data of NDS and HBR wind

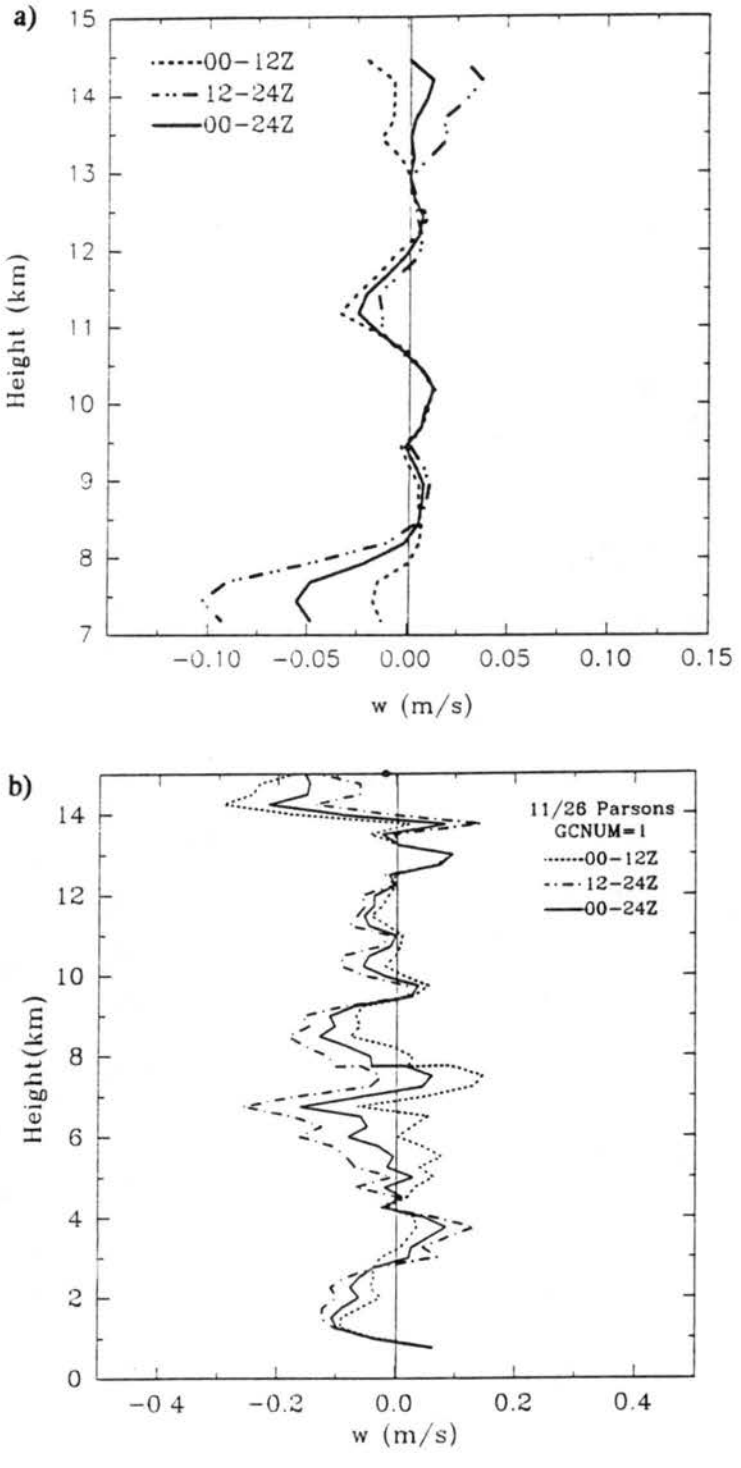

Figure 3.4 The profiles of the averaged vertical velocities from CSU wind profiler a) without GCR (Ground Clutter Removal), b) with GCR and GCNUM=1. Dash line: 00-12Z avraged, dash-dotted line: 12-24Z averaged, dash-dotted line: 12-24Z averaged, and solid line: daily averaged.

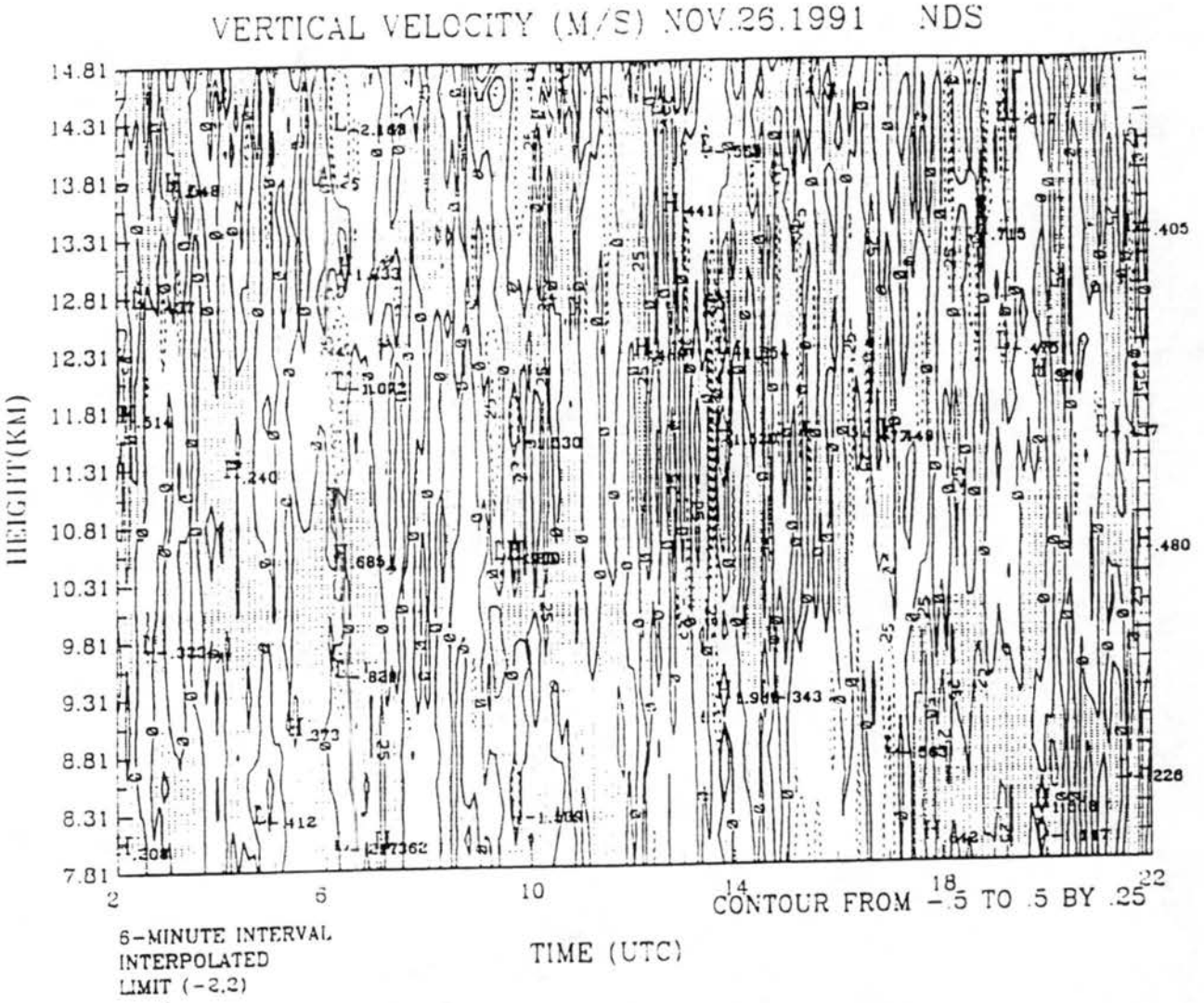

Figure 3.5 Time-height plots of the 6-minute cycle vertical velocities from NDS wind profiler. Shaded areas present upward motions. Contouring interval is 0.25 m/s.

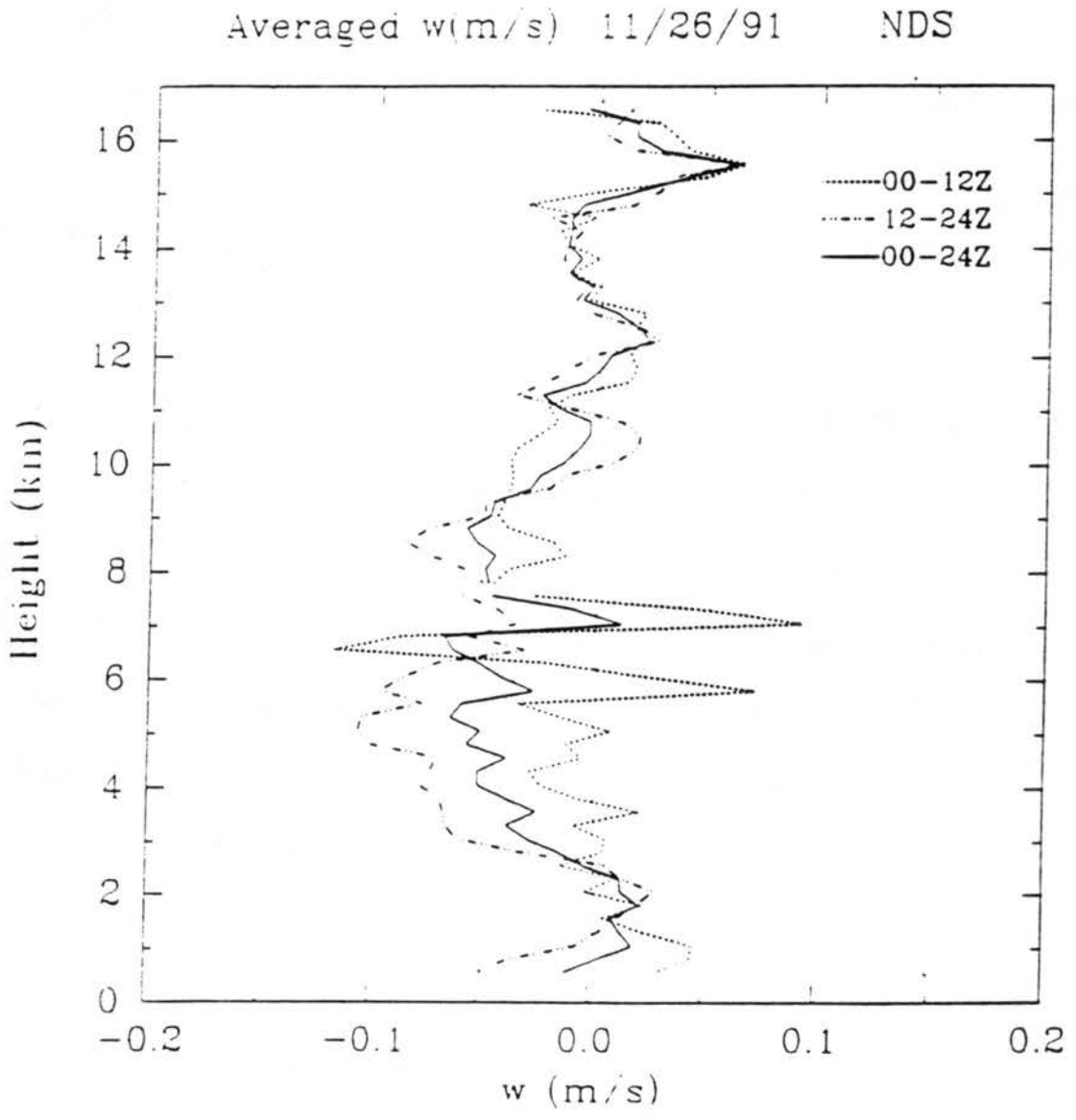

Figure 3.6 Averaged vertical velocity profiles from NDS wind profiler. Dashed line: 00-12Z averaged; dashed-dotted line: 12-24Z; solid line: daily averaged.

profilers show very random distributions between u, v and w (Figure 3.7) which predicts no significant effects from misalignment problem in our study cases.

The comparisons between these direct measurements of vertical velocity give greater confidence in the ground clutter removal algorithm applied on the CSU wind profiler. However, the strong downward motion below 10km during 12-24Z period is unexpected from the synoptic analysis presented in Chapter 5. Further discussion on the causes will be given in the next two sections and in Chapter 5. Questions about the strong central peak signal in a spectrum have not been resolved.

3.1.2 Quasi-VAD Method

The VAD method was originally developed for retrieving horizontal wind components from the radial velocities of a radar azimuth scan (Browning and Wexler 1972; Wilson and Miller 1972). By using the mass continuity equation under a quasi-hydrostatic condition, one can derive the vertical components of wind fields (Larsen et al. 1991; Doviak and Zrnic 1984). In our analysis, the CSU wind profiler's five-beam data were employed in a quasi-VAD technique in which we have only four sampling points in a horizontal circle. The circle radius increases with height.

The VAD sampling scheme is shown in Figure 3.8. U is the horizontal wind vector, w is the vertical velocity, z is the height, θ is the elevation angle of the oblique beams, and ϕ is the azimuth angle which is zero in the north direction and increases in the clockwise direction. Where a nearly linear horizontal wind field exists within the measurement circle so that the components u, v and w are well approximated by the zeroth- and first-order terms of a Taylor series, the measured radial velocity at

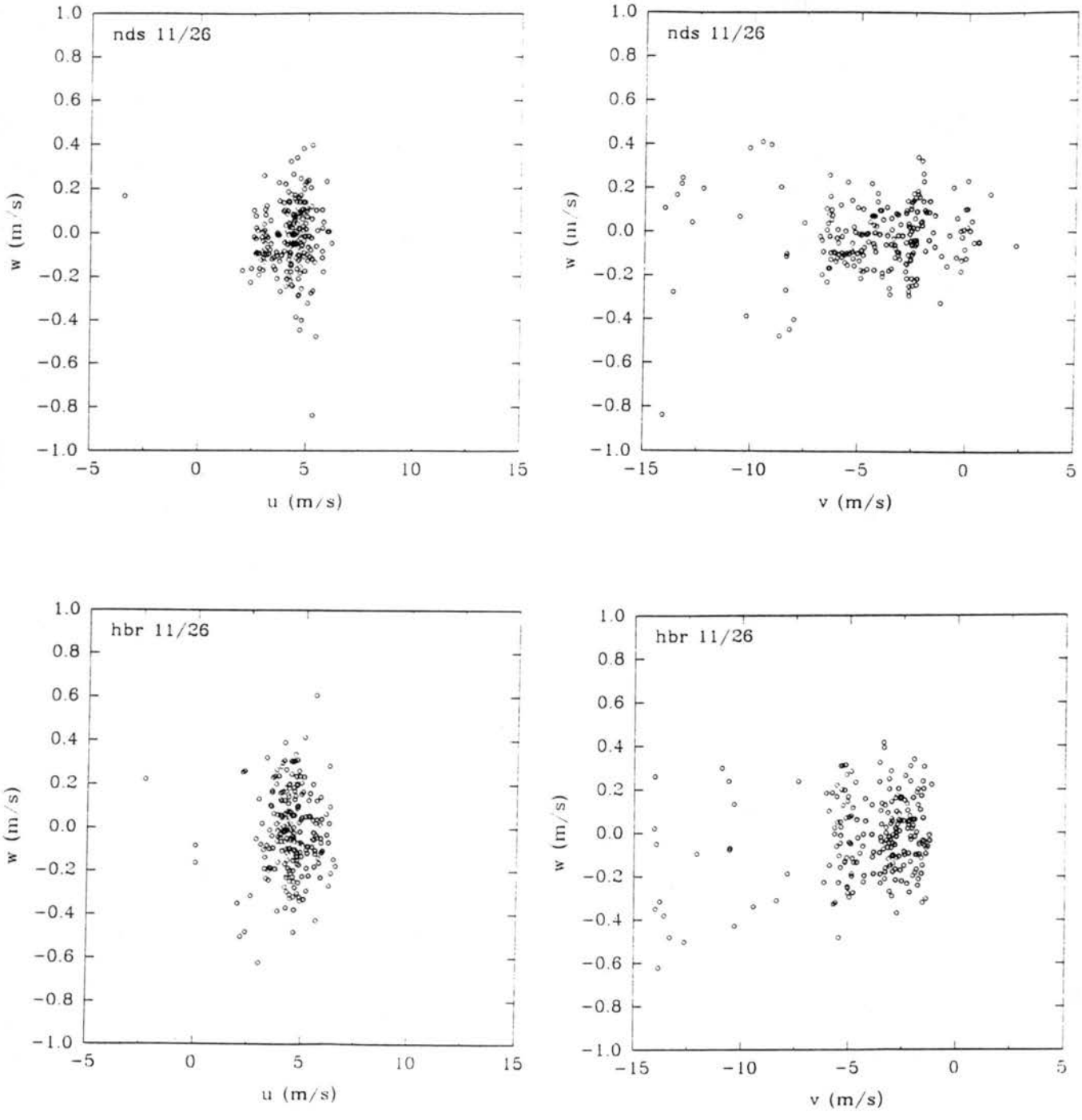

Figure 3.7 u-w and v-w plots from 6-minute cycle data of NDS and HBR wind profilers.

sampling points will fit a sine curve as shown in the lower panel of Figure 3.8. Here, ϕ_0 is the direction of the horizontal winds, and the offset, C_0, at each height is equal to the average radial velocity at all sampling points in one circle at that height. Referring to Browning and Wexler (1972), Dovial and Zrnic (1984), and Larsen et al.(1991), a derivation of the vertical velocity is shown below.

The radial velocity V_r at a sampling point (dots in Figure 3.8) can be expressed as:

$$V_r = w\cos\theta + u\sin\phi\sin\theta + v\cos\phi\sin\theta \qquad (3.1)$$

where, u, v are the east-west and north-south components of the horizontal wind, respectively. According to Taylor expansion theory, a variable A(x,y,z) can be expanded about a point (x_0,y_0,z_0) as

$$A(x,y,z) = A(x_0,y_0,z_0) + \frac{\partial A}{\partial x}(x-x_0) + \frac{\partial A}{\partial y}(y-y_0) + \frac{\partial A}{\partial z}(z-z_0) \qquad (3.2)$$

Assuming that the wind field is nearly linear within the measurement circle, the components u, v, w are well approximated by the zeroth- and first-order terms of a Taylor series about the radar location. In these series, the terms of partial differential of z can be neglected since the circle of the measurement lies on a horizontal plane and, u, v, and w can be expressed as:

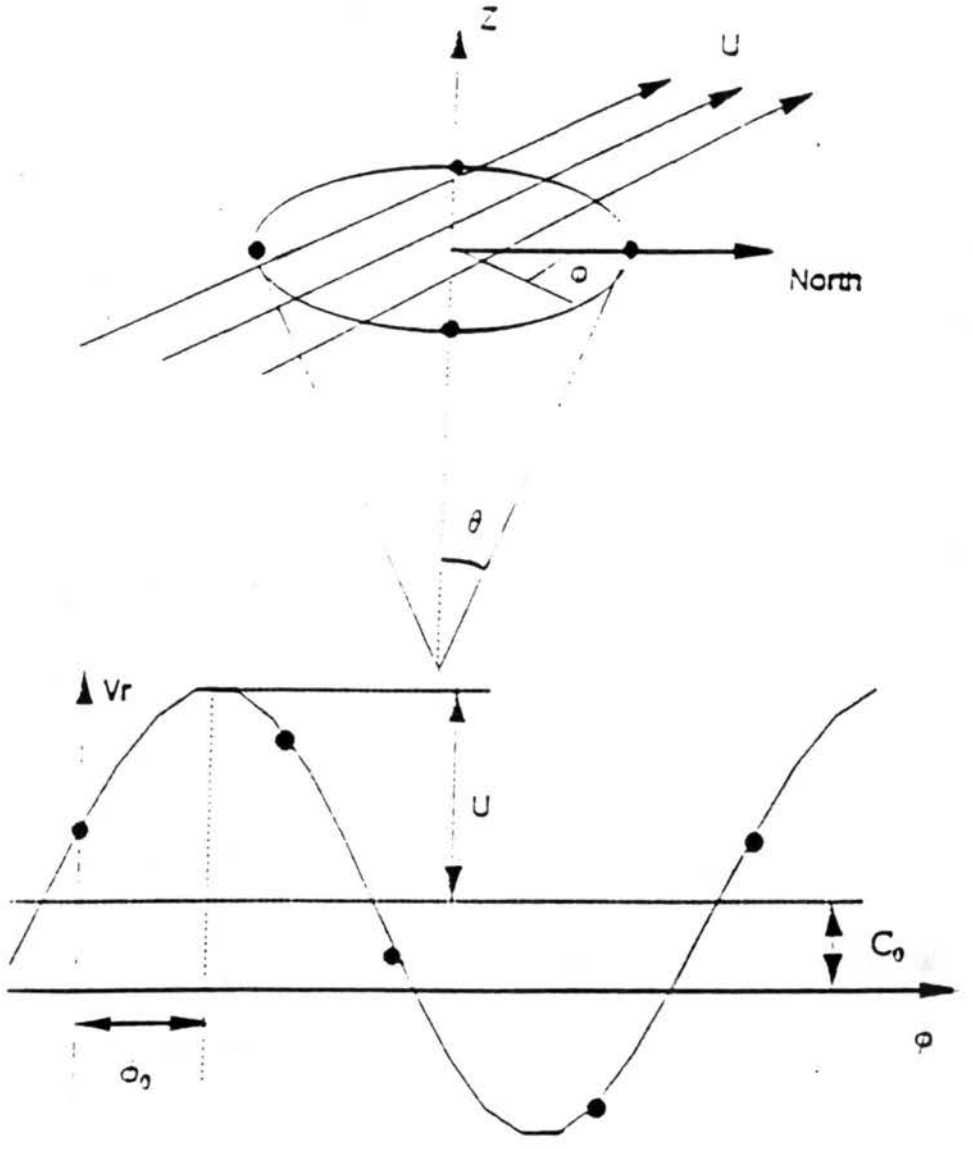

Figure 3.8 Schematic diagram of the quasi-VAD sampling and sine curve fitted by the sampled data.

$$u = u_0 + \frac{\partial u}{\partial x}(x-x_0) + \frac{\partial u}{\partial y}(y-y_0) \qquad (3.3)$$

$$v = v_0 + \frac{\partial v}{\partial x}(x-x_0) + \frac{\partial v}{\partial y}(y-y_0) \qquad (3.4)$$

$$w = w_0 + \frac{\partial w}{\partial x}(x-x_0) + \frac{\partial w}{\partial y}(y-y_0) \qquad (3.5)$$

where, u_0, v_0, and w_0 are the u, v, and w components above the radar site, respectively, and

$$x-x_0 = r\sin\theta\sin\phi, \qquad y-y_0 = r\sin\theta\cos\phi \qquad (3.6)$$

Substituting Equations 3.3 to 3.6 into Equation 3.1, yields

$$\begin{aligned} V_r = {} & w_0\cos\theta + \frac{\partial w}{\partial x} r\sin\theta\sin\phi\cos\theta + \frac{\partial w}{\partial y} r\sin\theta\cos\phi\cos\theta \\ & + u_0\sin\phi\sin\theta + \frac{\partial u}{\partial x} r\sin^2\theta\sin^2\phi + \frac{\partial u}{\partial y} r\sin^2\theta\cos\phi\sin\phi \\ & + v_0\sin\theta\cos\phi + \frac{\partial v}{\partial x} r\sin^2\theta\sin\phi\cos\phi + \frac{\partial v}{\partial y} r\sin^2\theta\cos^2\phi \end{aligned} \qquad (3.7)$$

Using trigonometric identities, we can combine the terms in the above equation and obtain a final equation for V_r,

$$\begin{aligned} V_r = {} & w_0\cos\theta + \frac{1}{2}\left(\frac{\partial u}{\partial x} + \frac{\partial v}{\partial y} \right) r\sin^2\theta + \left(\frac{\partial w}{\partial x} r\cos\theta + u_0 \right)\sin\theta\sin\phi \\ & + \left(\frac{\partial w}{\partial y} r\cos\theta + v_0 \right)\sin\theta\cos\phi + \frac{1}{2}\left(\frac{\partial u}{\partial y} + \frac{\partial v}{\partial x} \right) r\sin^2\theta\sin 2\phi \\ & + \frac{1}{2}\left(\frac{\partial v}{\partial y} - \frac{\partial u}{\partial x} \right) r\sin^2\theta\cos 2\phi \end{aligned} \qquad (3.8)$$

Expressing V_r with a Taylor series:

$$V_r = \frac{1}{2}c_0 + \sum_{n=1}^{\infty}(c_n\cos n\phi + d_n\sin n\phi) \qquad (3.9)$$

According to an orthogonal expansion,

$$c_0 = \frac{1}{\pi}\int_{-\pi}^{\pi} V_r d\phi = \frac{1}{\pi}\sum_{i=1}^{N} V_r(i)\cdot\frac{2\pi}{N} = \frac{2}{N}\sum_{i=1}^{N} V_r(i) \qquad (3.10)$$

$$c_n = \frac{1}{\pi}\int_{-\pi}^{\pi} V_r\cos n\phi d\phi = \frac{2}{N}\sum_{i=1}^{N} V_r(i)\cos n\phi_i \qquad (3.11)$$

$$d_n = \frac{1}{\pi}\int_{-\pi}^{\pi} V_r\sin n\phi d\phi = \frac{2}{N}\sum_{i=1}^{N} V_r(i)\sin n\phi_i \qquad (3.12)$$

where, N is the number of sampling points in a circle. In our application, N=4.

Comparing Eq. (3.10) with Eq. (3.8), we can find the relation in Eq.(3.13) from the zeroth order term of ϕ:

$$w_0\cos\theta + \frac{1}{2}\left(\frac{\partial u}{\partial x} + \frac{\partial v}{\partial y} \right) r\sin^2\theta = \frac{1}{2}c_0 = \frac{1}{N}\sum_{i=1}^{N} V_r(i) \qquad (3.13)$$

Instead of neglecting the contribution of the local vertical motion w_0 in the traditional manner, Larsen et al.(1991) relates the contributions from w_0 and the divergence term by writing the mass continuity equation, under the assumption that the air density is stationary in time locally and the medium is horizontally stratified, as,

$$\nabla_h \cdot \rho U = \rho \nabla_h \cdot U = -\frac{\partial}{\partial z}(\rho w) \qquad (3.14)$$

Combining the above equations and integrating the differential equation from an upper height boundary z_T by assuming zero w at z_T, we have Eq.(3.15),

$$-(\rho w)_z + \frac{2\sin\theta}{\cos^2\theta}\int_z^{z_T} \frac{\rho C_0}{z} dz - 2\tan^2\theta \int_z^{z_T} \frac{\rho w}{z} dz = 0 \qquad (3.15)$$

The vertical velocity can then be deduced from Eq.(3.15) numerically by dividing the whole layer into m-1 layers as shown in Figure 3.9; w at level k can be calculated by a recursion equation as,

$$w_k = \frac{A \sum_{j=1}^{k} \frac{\rho_j}{z_j} \left(\frac{1}{N} \sum_{i=1}^{N} V_r(i) \right)_j \Delta z - B \sum_{z_j}^{k-1} \frac{\rho_j w_j}{z_j} \Delta z}{\rho_k \left(1 + \frac{B\Delta z}{z_k} \right)} \qquad (3.16)$$

where, ρ_k is the air density at kth level, and

$$A = \frac{2\cos\theta}{\sin^2\theta} \qquad B = 2c\tan^2\theta \qquad (3.17)$$

In this method, it should be noted that any large gradient of the horizontal wind or horizontal wind variation with a scale smaller than the circle formed by those four beams (e.g., 5.36km diameter at 10km height) might lead to large errors to the w calculations.

Figure 3.10 presents the hourly averaged vertical velocities deduced from the quasi-VAD technique based on the CSU wind profiler data with the bottom and top

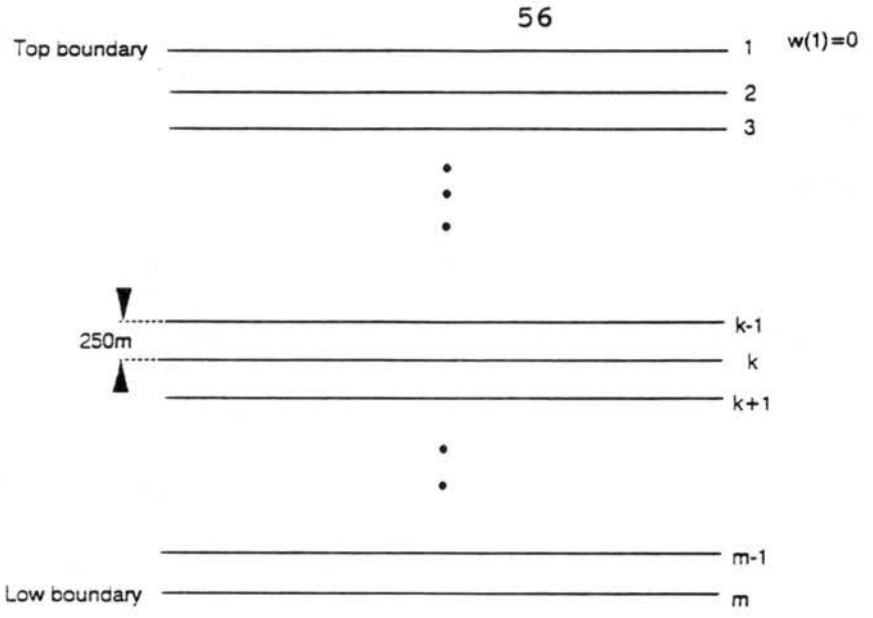

Figure 3.9 Schematic of the definition of the layers used by Equation (3.16).

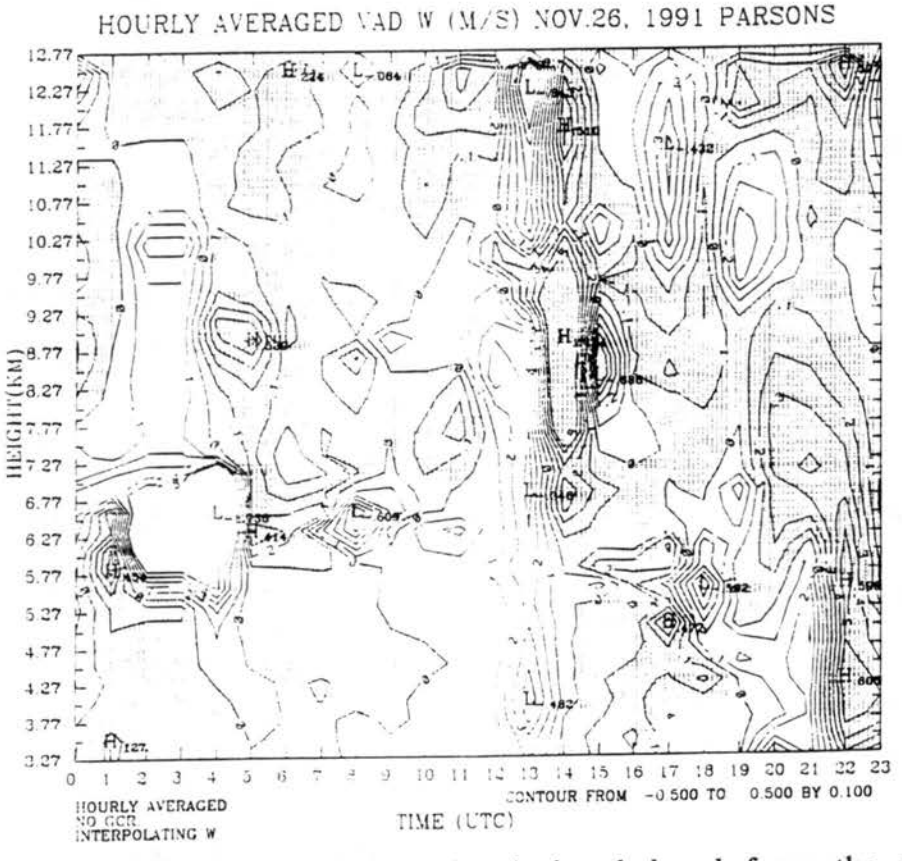

Figure 3.10 Hourly averaged vertical velocity deduced from the quasi-VAD technique based on the CSU wind profiler data. Shaded areas are upward motions. Contour interval is 0.1m/s.

boundaries set at 3.3km and 12.7km, respectively. The resultant vertical velocities are generally smaller than those obtained from the direct measurements which suggests that small scale features might have been averaged out. Long time period downward and upward motions are evident. However, there are some extremely large values, (e.g. 6.5km at 03Z) which could be caused by the bivariate interpolation. Figure 3.11 shows the 12-hour and 24-hour averaged vertical velocity profiles. During the 00-12Z averaging period, there was a strong downward motion (0.25m/s peak value) between 6km and 7km. This downward motion was replaced by an upward motion (0.1m/s peak value) in the 12-24Z averaging period. Above 7km, the 00-12Z averaged profile has a upward motion all way up. The 12-24Z profile shows a stronger upward motion between 7km and 10km, however, a weak downward motion above the tropopause. The averaged vertical velocities mainly range between -0.1m/s and 0.1m/s.

Comparisons between the vertical velocity profiles deduced from the quasi-VAD method (Figure 3.11) and the directly measured profiles (Figure 3.4b, Figure 3.6) show strong disagreements. Particularly, during the 12-24Z period, the direct measurements present a downward motion below 10km instead of an upward motion as seen in the results of the quasi-VAD method. This difference is discussed further in Chapter 5.

3.1.3 Kinematic Method

The kinematic method was first developed as an objective calculation of divergence and vertical velocity by Bellamy(1949). The general idea of the kinematic method is to calculate the divergence of a horizontal wind field by using one of the

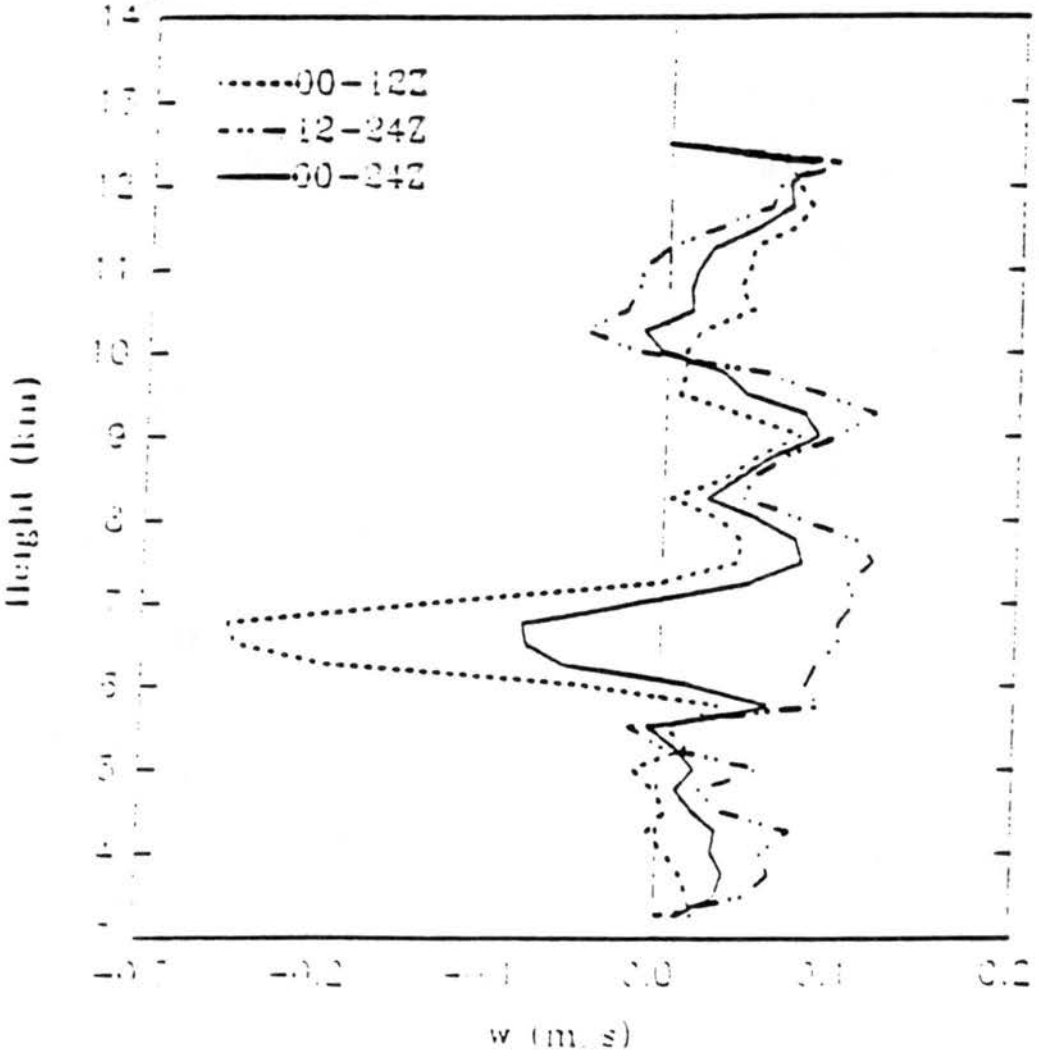

Figure 3.11 Average vertical velocity profiles from the quasi-VAD tech.

following methods: Bellamy's objective method; the line-integral method (Ceselski and Sapp 1975; Schaefer and Doswell 1979); multiple-station fitting method (Endlich and Clark 1963); or the linear vector point function method (Zamora et al. 1987), and Doswell and Caracena 1988). The vertical velocity is then calculated from the divergence based on the mass continuity equation.

From its definition, the divergence can be expressed as a relative rate of change of a horizontal area:

$$D = \frac{\partial u}{\partial x} + \frac{\partial v}{\partial y} = \lim_{\substack{\Delta x \to 0 \\ \Delta y \to 0}} \left(\frac{\Delta u}{\Delta x} + \frac{\Delta v}{\Delta y} \right) = \lim_{\substack{\Delta x \to 0 \\ \Delta y \to 0}} \frac{\Delta u \Delta y + \Delta v \Delta x}{\Delta x \Delta y} \qquad (3.18)$$

$$= \lim_{\substack{\Delta x \to 0 \\ \Delta y \to 0}} \frac{\Delta y \frac{\delta \Delta x}{\delta t} + \Delta x \frac{\delta \Delta y}{\delta t}}{\Delta x \Delta y} = \lim_{\substack{\Delta x \to 0 \\ \Delta y \to 0}} \frac{\frac{\delta}{\delta t}(\Delta x \Delta y)}{\Delta x \Delta y} = \frac{1}{\sigma} \frac{\delta \sigma}{\delta t}$$

where, σ is an area unit in a horizontal surface. If there are more than two noncollinear observation points, the averaged divergence can be calculated by using the relative rate of the area change of a polygon formed by these points. In our study, a simplified calculation of the area change is applied by using matrices, however, with any calculation of the polygon area by analytic geometry, an assumption of a linear wind distribution between each pair of vertices must be made in order to retain the shape of the polygon. In analytic geometry, the area of a triangle can be simply expressed as a matrix formed by the coordinates of three vertices. Defining σ and σ'

as the original area and the area after a time period Δt of a triangle, respectively, yields,

$$\sigma = \frac{1}{2}\begin{vmatrix} x_1 & y_1 & 1 \\ x_2 & y_2 & 1 \\ x_3 & y_3 & 1 \end{vmatrix} \qquad \sigma' = \frac{1}{2}\begin{vmatrix} x_1' & y_1' & 1 \\ x_2' & y_2' & 1 \\ x_3' & y_3' & 1 \end{vmatrix} \tag{3.19}$$

$$x_i' = x_i + u_i \Delta t \qquad y_i' = y_i + v_i \Delta t \qquad i = 1,2,3$$

By using this method, an inefficient nomograph method given by Bellamy (1949) is avoided.

After obtaining the horizontal divergence, vertical velocity is derived from the mass continuity equation:

$$\frac{1}{\rho}\frac{d\rho}{dt} + \frac{\partial u}{\partial x} + \frac{\partial v}{\partial y} + \frac{\partial w}{\partial z} = 0 \tag{3.20}$$

Assuming the air is incompressible, i.e., $d\rho/dt=0$, the vertical velocity can be solved numerically from the following equation with a zero velocity, w_N, at the top boundary (Fig. 3.12).

$$w_k = w_N + \sum_{i=k}^{N-1} \overline{D_i} \Delta p \qquad k = 1,2,\ldots.N-1 \tag{3.21}$$

$\overline{D}_i$ is the mean divergence of the layer between zi and zi+1.

Due to this integral, the errors of the divergence at upper layers will be added and transferred to vertical velocities calculated at the lower layers. Therefore

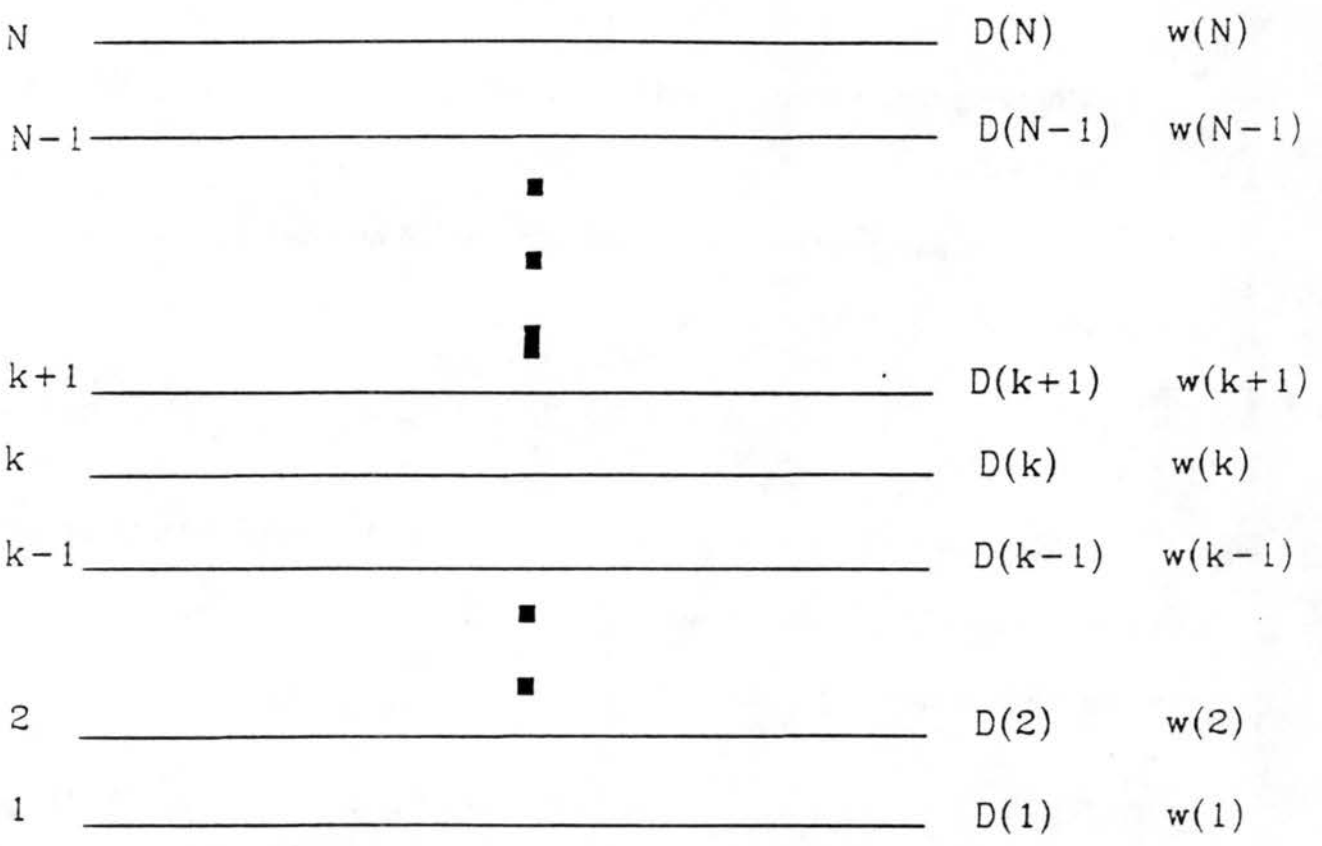

Figure 3.12 Schematic of the definition of the layers used in Equation (3.21).

corrections must be applied and should have stronger weights at lower layers which have larger errors. Here, we use a linear correction function which means the correction of the velocity at height z is a linear function of the distance between the top boundary and z. Defining w′ and D′ as the corrected vertical velocity and divergence, respectively and substituting w′ and D′ into Eq.(3.22) and using ΔD_k as the divergence adjustment at kth layer, Eq.(3.23) is obtained:

$$w_k' = w_k + \sum_{i=k}^{N-1} \frac{\Delta D_{i+1} + \Delta D_i}{2} \Delta z \qquad (3.22)$$

where, we use a constant adjustment to the divergence, i.e.,$\Delta D_k = \Delta D$ (k=1,2....N). At the lower boundary, $w_1' = \alpha w_1$, and α is an adjusting parameter and ranges between 0 and 1.0. If $\alpha=1$, there is no correction, and if $\alpha=0$, the correction is the strongest. The adjusted vertical velocities and divergences are then expressed as:

$$w_k' = w_k + \frac{N-k}{N-1}(\alpha-1)w_1, \quad \Delta D_k = \Delta D = \frac{(\alpha-1)w_1}{(N-1)\Delta p} \qquad k=1,2...N \quad (3.23)$$

As well as defining zero vertical velocity at the top boundary, the resulting divergence and vertical velocity will make the total divergence and convergence in the whole layer equal assuming a constant air density profile. Since the air density does decrease with height, the total air mass in the whole air column is not truly conserved.

Figure 3.13 shows the results of w calculated from the horizontal winds of wind profilers at NDS(Neodesha, KS), HBR(Hillsboro, KS), and LMN(Lamont, OK) on

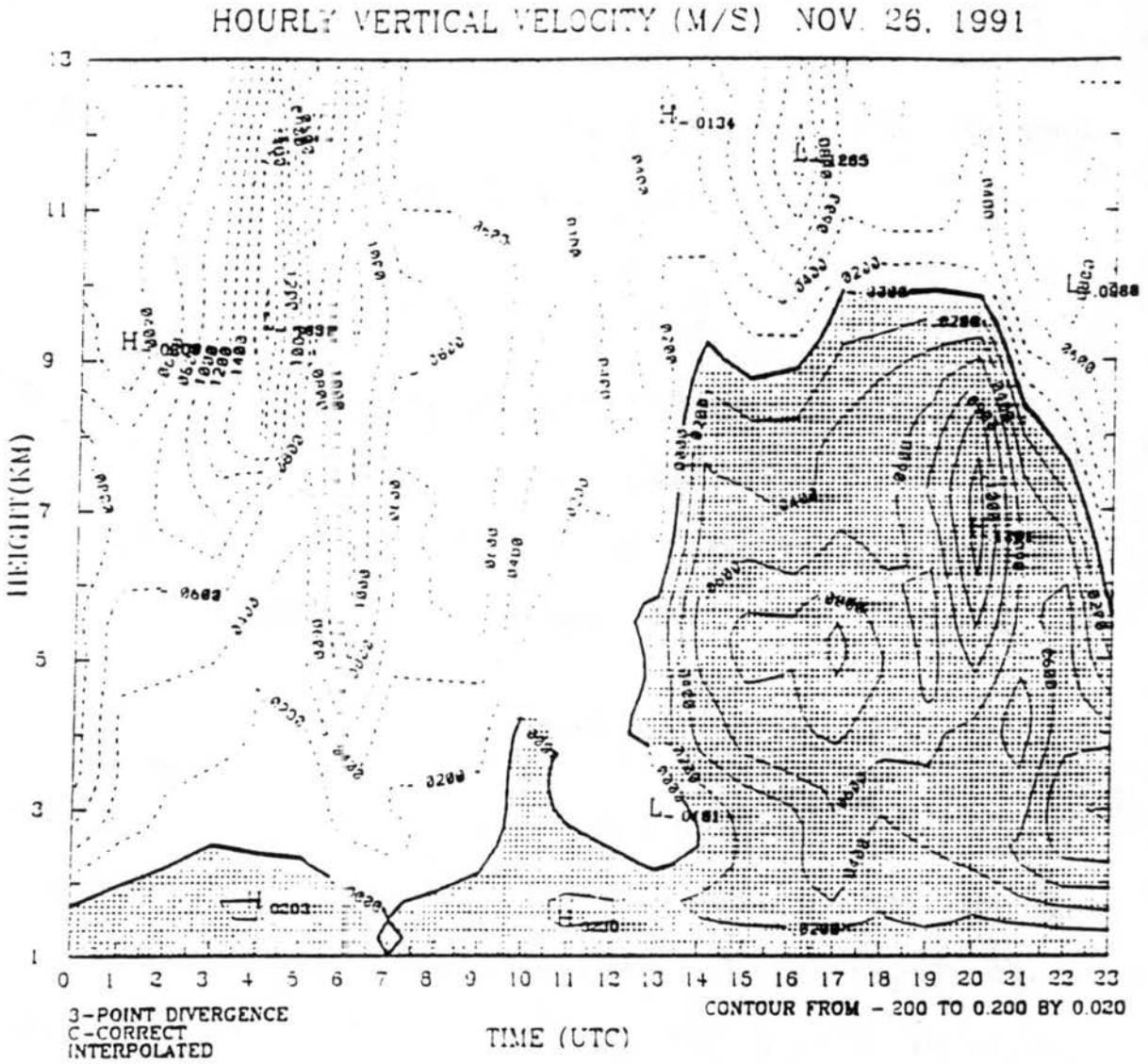

Figure 3.13 Hourly averaged vertical velocities from the kinematic method. Contour interval is 0.02m/s. Shaded areas indicate upward motions. Dark solid line is the zero line.

November 26, 1991. There is a clear separation between the downward and upward motions. Generally speaking, the downward motions predominate in the wholeatmosphere from 00Z until 13Z. Then the upward motions became prevalent, especially in the troposphere. The strength of both the upward and downward motions are generally between -0.1m/s to 0.1m/s, which are weaker than those determined from the previous two methods. Figure 3.14 gives the 12-hour and 24-hour averaged vertical velocity profiles. Comparisons with the observations from the previous two methods show regions of both agreement and disagreement. The negative mean vertical velocity profile from 00-12Z is consistent with the direct measured profile (Figure 3.4b, and Figure 3.6). During 12-24Z, the profile in Figure 3.14 has a positive mean profile in the troposphere, which is also evident in the profile deduced from the quasi-VAD technique (Figure 3.11), however, the negative mean profile dominating the layer above 9km (Figure 3.14) corresponds to a weaker downward motion confined to the layer between 10km and 11.5km in the results from the quasi-VAD method (Figure 3.11).

When a fourth station was included in the polygon (not shown) the resulting difference is very small from the results of the triangle.

Bellamy (1949) presumed that the vertical velocities deduced from this method are the values at the centroid of the polygon, however, Davies-Jones (1993) have shown that the calculated value is a much closer estimate of the mean value over the polygon area rather than the value at the centroid.

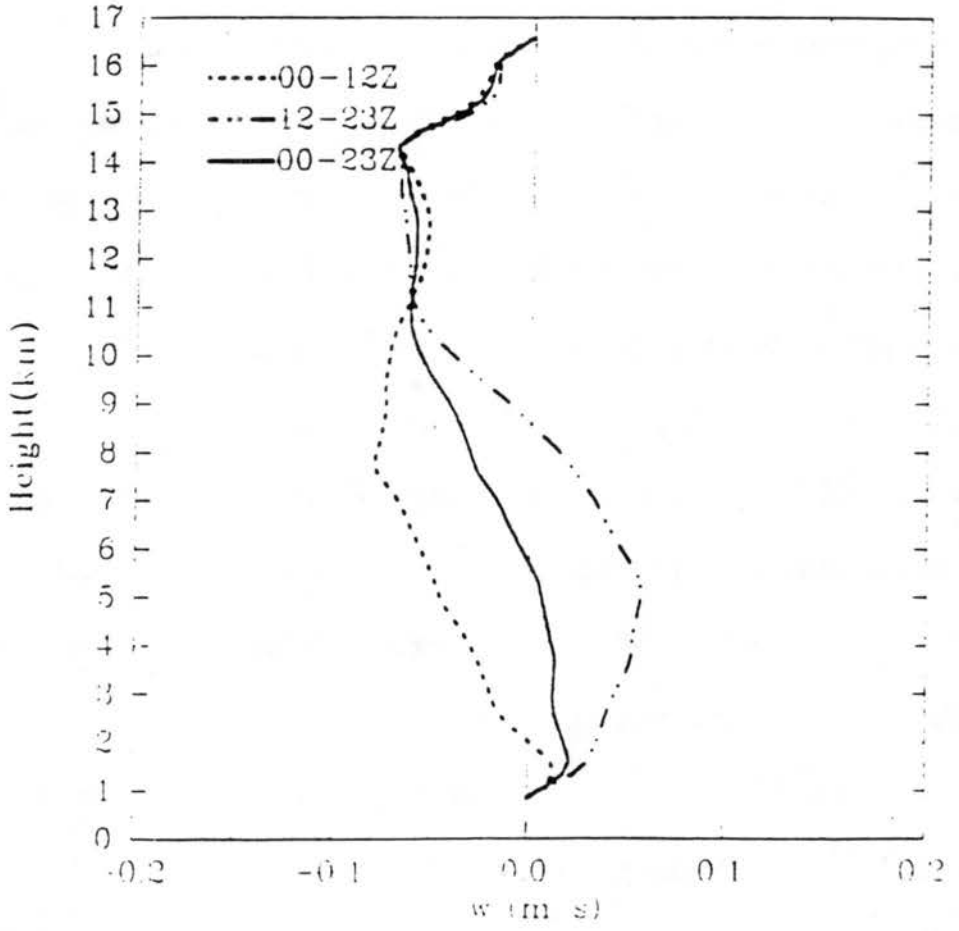

Figure 3.14 Averaged vertical velocity profiles deduced from kinematic method. Dash line: 00-12Z averaged, dash-dotted line: 12-23Z averaged, solid line: daily averged.

3.2 Discussion

A simple comparison of these three methods is given in Table 3.1. It shows that assumptions of linear wind field, certain constrains on the air mass field and boundary condition are applied to KM and QVAD, which do not happen to DDM. The scale of observed vertical wind fields from each methods are quite different. KM produces vertical wind field averaged over three radar area, which has a scale about 100km. QVAD produces average vertical wind field over four radar beams area which changes with height, eg. 5km at 10km height. DDM is the method to measure vertical wind field of the point over the radar site. Factors which affect the accuracy of measurements are considered in the last column. It shows that the accuracy of measurement of horizontal wind have influence on both KM and QVAD. And KM calculates small divergence from change of large areas. This may cause large error. The most significant concerns to DDM are probably concluded as the effect from ground clutter and precipitation, and the sensitivity to small scale air motions.

The observational comparison between the averaged profiles deduced from direct measurements of the CSU wind profiler (Figure 3.4b) and NOAA wind profiler at NDS (Figure 3.6) illustrates good consistency except that the magnitudes of the vertical velocities are larger for the CSU measurements, indicating the width of the ground clutter removal window applied to the CSU wind profiler might be too large and the velocity resolution not fine enough.

Table 3.1: Comparison of Methods Used to Deduce Vertical Velocity

Method	Assumptions	Horizontal Spatial Scale	Temporal Scale	Limitations
Kinematic NWS Rawinsonde	•Linear V_H; •Incompressible air; •w_{top}=0.0	Average over three rawinsonde stations (300 Km)	Twelve hours	•Balloon advection 60 minute flight duration •Apply change of large number (area) to calculate small number (divergence)
Kinematic (KM) Profiler	•Linear V_H; •Incompressible air; •w_{top}=0.0 •Echo producing gradients move with mean horizontal wind	Average over three profiler sites (100km) radius.	6 minutes to 1 hour	•Affected by accuracy of V_H; •Apply change of large number (area) to calculate small number (divergence)
QVAD	•Linear V_H; •Locally stationary air field; •Horizontally stratified air field. •w_{top}=0.0 •Echo producing gradients move with mean horizontal wind	Average over four radar beams (about 5km radius at 10km height)	10 minutes	•Affected by accuracy of V_H
Direct Doppler Method (DDM)	•Echo producing gradients move with mean vertical air motion	1 Km	2 minutes	•Affected by ground clutter & precipitation; •Sensitive to small scale motion

Comparisons of the time-height plots of the vertical velocities deduced from these three methods (Figures 3.3, 3.5, 3.10 and 3.13) show that the DDM measurements include many more small scale air motions which are even evident after hourly averaging has been performed (not shown here). Questions about whether the wind profilers can provide synoptic wind data were raised by Larsen (1983) and Nastrom (1984; 1985). A temporal averaging process is strongly recommended and it is expected that a 9-hour averaging can produce good subsynoptic-scale data (Nastrom, 1985). A time-domain filter may be also useful in

extracting the large scale features from those wind data. On the other hand, the kinematic method deduces only the large scale structure which, in our case, was dominated by a jet streak dynamical process. The scale of the vertical motions measured by the quasi-VAD method is more complex (cf. Figure 3.3, 3.5, 3.10 and 3.13).

Both agreement and disagreement is found among the direct measurements of the vertical velocities and the indirect measurements from the quasi-VAD method (Figure 3.11) and the kinematic method (Figure 3.14). During the period from 00-12Z, when there was clear sky, directly measured profile (Figure 3.6) shows a weak upward vertical motion, however, the profile derived from the kinematic method has a large consistent descending motion. Between 12-24Z, when there were clouds appearing, direct measurements show a downward motion in the whole atmosphere rather than the pattern resulting from the indirect methods, which showed an upward motion in the troposphere and a change of the velocity sign near the tropopause. As will be discussed in Chapter 5, from the synoptic conditions, ascending motions in the upper troposphere and descending motions in the stratosphere are expected at the experiment site during the period from 12-24Z. We may expect that motions of different scales were measured by different methods and cause the discrepancies.

Chapter 4

STUDIES ON A JET STREAK AND CIRRUS CLOUD SYSTEM

Cirrus cloud systems associated with the jet stream are a commonly observed feature of the upper troposphere. While studies of jet streak secondary circulations have progressed significantly during the past decades, the internal characteristics of cirrus clouds and their dynamical structures are still largely unknown. In order to investigate the related momentum, heat and moisture budgets associated with cirrus cloud systems, a set of dependable in situ measurements and multi-scale analysis techniques are required. In this chapter, we will give a general survey of previous research on jetstream cirrus cloud systems. This background will be used to provide insight into the data analysis in the next chapter.

4.1 Jet Streak (Ageostrophic Circulation)

A jet streak is defined as a region that has the strongest local winds inside a Polar-Front jet or a subtropical jet and moves through the axis of the jet stream with a speed less than that of the wind. Air parcels accelerate in the entrance region of the jet streak and decelerate in the exit region. Along the jet streak axis, both the entrance and the exit areas can be divided into a left and a right area, or a warm and a cold side. The definition of the direction is given with respect to an observer who is facing downstream. The concept of the "warm" and the "cold" side is defined by

the thermal field in the troposphere. Temperature structure in the stratosphere is reversed.

Even though the study of the mechanism of a jet streak and its related dynamical features, such as upper level front, has progressed greatly in the last fifty years due to advances in both the observations and numerical modeling, questions concerning the accurate dynamical description of a jet, a jet-front system, their life-cycle, and scale interactions still exist. The fundamental dynamical processes of a jet streak and jet-front system have been successfully studied by partitioning the mass and momentum budgets into their geostrophic (primary) and an ageostrophic (secondary) components. The observational, diagnostic and theoretical studies of the ageostrophic cells have shown that a two-dimensional theory of the ageostrophic circulations, in the absence of the along-jet ageostrophic winds, fits very well with the cases of straight jet streak. In the presence of curvature, a three-dimensional model of the ageostrophic circulations has to be considered, in which the along-jet ageostrophic winds are superimposed upon the cross-jet ageostrophic circulations using the concepts of the gradient wind (Shapiro and Kennedy, 1981; Keyser and Shapiro, 1986); these ageotrophic circulations may significantly modify the divergence structure in the vicinity of the jet from a two-dimensional model.

Namias and Clapp (1949), in their pioneering study of the ageostrophic circulation and the associated vertical wind field proposed the "Confluence Theory". Through qualitative analysis, they concluded that a confluence of northerly cold air flow and southerly warm flow (in the northern hemisphere) upstream from a jet

streak would result in upward motion on the warm side and downward motion on the cold side of the jet streak in the middle, upper troposphere and lower stratosphere. A schematic diagram of this two dimensional direct circulation is shown in Figure 4.1. Through this direct circulation, potential energy is transformed into kinetic energy responsible for the zonal wind acceleration. The possibility of the existence of a stratospheric reverse circulation cell above this direct circulation was also suggested. However, as mentioned in Keyser and Shapiro (1986), this confluence hypothesis of the origin of jet streaks has never been demonstrated due to the lack of necessary observations in the area where the confluence process is preferred (e.g., the Gulf of Alaska and western Canada).

Uccellini and Johnson (1979) simulated the mass and momentum adjustments in the jet streak entrance and exit areas using the geostrophic momentum approximation in isentropic coordinates. In terms of mass transfer, a four-cell, two-layer pattern was defined in the upper troposphere; there is divergence in the warm-entrance and cold-exit areas of a jet streak, and convergence in the cold-entrance and warm-exit areas. In the lower troposphere, these four cells have reversed signs of the mass transfer. This pattern agrees with Namias and Clapp's (1949) confluence hypothesis applied to the entrance region of a jet streak. Partitioning the mass flux divergence into a geostrophic and ageostrophic components, Uccellini and Johnson (1979) predicted that the ageostrophic mode of the mass flux divergence dominates the mass adjustment process in the whole troposphere. A further analysis of the ageostrophic flux mode in their study demonstrated that the cross-stream component

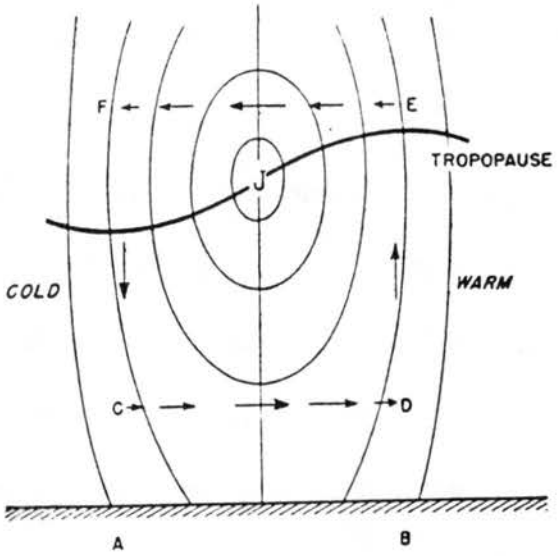

Figure 4.1 Two dimensional ageostrophic circulation of a jet streak. Jet is indicated by J, and tropopause is indicated by a heavy line. The arrows represent direction and relative strength of ageostrophic circulation. (Namias and Clapp, 1949)

generally dominates in the lower troposphere, however, with almost equal contributions from cross-stream and along-stream ageostrophic components in the upper troposphere. The derivation of the transverse ageostrophic wind illustrated that ageostrophic winds direct toward cold (warm) side in the entrance (exit) region in the upper troposphere, and have opposite direction in the lower tropospheric layer. The same structure of the mass flux and the transverse ageostrophic winds was also produced in Bluestin (1993) using the parcel method and diagnostic omega equation based on the quasi-geostrophic and semi-geostrophic assumptions. Assuming that the jet streak is located close to the tropopause level where the vertical wind motion can presumably be zero (strictly saying, vertical velocity at the

tropopause is not necessarily zero, especially when there is tropopause folding which produces mixing between the troposphere and stratosphere), vertical wind circulation is therefore deduced by using the continuity equation. Ascending motions form in the warm-entrance and cold-exit area of a jet streak, and descending motions in the cold-entrance and warm-exit area.

Until now, the discussions of the air flux and ageostrophic circulation have been limited to the area below the jet core. Questions are raised about what pattern of the ageostrophic circulation can be expected above the jet core. A brief description of a two dimensional ageostrophic circulation model was given by Mattocks and Bleck (1986), where an ageostrophic circulation above the jet streak develops with an opposite direction as the circulation below the jet core.

Using in-situ observations and diagnostic analyses based on upper-air sounding data, airplane data, radar wind profiler data and satellite ozone measurements, several works (eg. Shapiro,1981; Shapiro and Kennedy, 1981; Keyser and Pecnick, 1985a,b; Keyser and Johnson, 1984; Keyser and Shapiro, 1986) presented a more complex process of the origin and development of a jet-front system and a more sophisticated circulation structure in the vicinity of a jet streak. Shapiro (1981) reveals that a primary geostrophic circulation and a secondary ageostrophic circulation both dominate the frontogenetical forcing processes. It is concluded that frontogenesis in the vertical and horizontal gradients of absolute momentum and potential temperature can be defined as a purely ageostrophic process, which acts to maintain the geostrophic balance between the absolute momentum and the horizontal

thermal gradient destroyed by the geostrophic deformation. Using the Sawyer-Eliassen secondary circulation equation, Shapiro (1981) further divided the geostrophic deformation effects into geostrophic stretching deformation Q1 and shearing deformation Q2. Geostrophic stretching deformation Q1, which is proportional to $\partial Vg/\partial y\ \partial\theta/\partial y$ on an isobaric surface p, represents the effect of a geostrophic confluence (difluence) $\partial Vg/\partial y$ in strengthening (relaxing) cross-front (jet stream) thermal gradients, $\partial\theta/\partial y$. Geostrophic shearing deformation Q2, which is proportional to $\partial Ug/\partial y\ \partial\theta/\partial x$ in an isobaric surface p, represents the cross-front (jet stream) geostrophic wind shear $\partial Ug/\partial y$ effect in rotating along-front thermal gradients $\partial\theta/\partial x$ into (out of) the cross-front direction. The so-called geostrophically forced secondary circulations are introduced in response to these deformations of the cross-front thermal gradient (Shapiro, 1981).

Figure 4.2 exhibits several patterns of the potential temperature field relative to a straight upper-tropospheric jet wind field summarized in Keyser and Shapiro (1986); this shows the effects of the stretching deformation Q1 and shearing deformation Q2. Figure 5.1a gives the response purely from the stretching term Q1, i.e., only confluence/difluence effect. Q2 is zero due to along-jet thermal advection $\partial\theta/\partial x$ equals to zero. This is the case which agrees with a classical confluence/difluence model. Figure 4.2b is the pure response from the shearing term Q2 (Q1 is zero due to $\partial\theta/\partial y=0$) under a along-jet cold advection condition, in which two indirect circulations are produced on the warmer side of the jet streak with two direct circulation cells existing on the colder side. Circulations with opposite

directions are expected for the purely shearing deformation forcing in a warm advection case. Figure 4.2c,d give the ageostrophic circulation resulting from the combination of the stretching and shearing deformations, in which the superposition of the responses from both forcings shows an asymmetric ageostrophic wind field to the jet axis. Upward motion is strengthened and the direct circulation is moved toward the warm side of the jet, for example, in the confluent entrance region of the cold advection case. However, in this case the forcing of the shearing deformation (or due to thermal advection) is not as strong as the case in Shapiro (1984) to have one direct and one indirect circulation in the entrance or exit area, and only cause imbalance between the downward and upward motions and shift the zero vertical velocity line away from the jet streak axis. Figures 4.2e and f show the cases in which the thermal structures are not simply cold or warm advection, but have a thermal ridge and trough, respectively. In the thermal ridge case, the jet entrance and exit regions are advected by cold and warm air, respectively. This structure shifts both the direct circulation in the entrance area and indirect circulation in the exit area toward the warm side. In the thermal trough case, this structure is reversed.

As well as the direction of the transverse ageostrophic circulations, Keyser and Shapiro(1986) qualitatively related the shape of the ageostrophic elliptical cell in a transverse cross section to the coefficients of the response terms in the Sawyer-Eliassen equation according to Eliassen's earlier work in 1960s. It is concluded that (1) large (small) potential vorticity and small (large) inertial stability suppress (favor) vertical motions and favor (suppress) horizontal ageostrophic motions, resulting in an

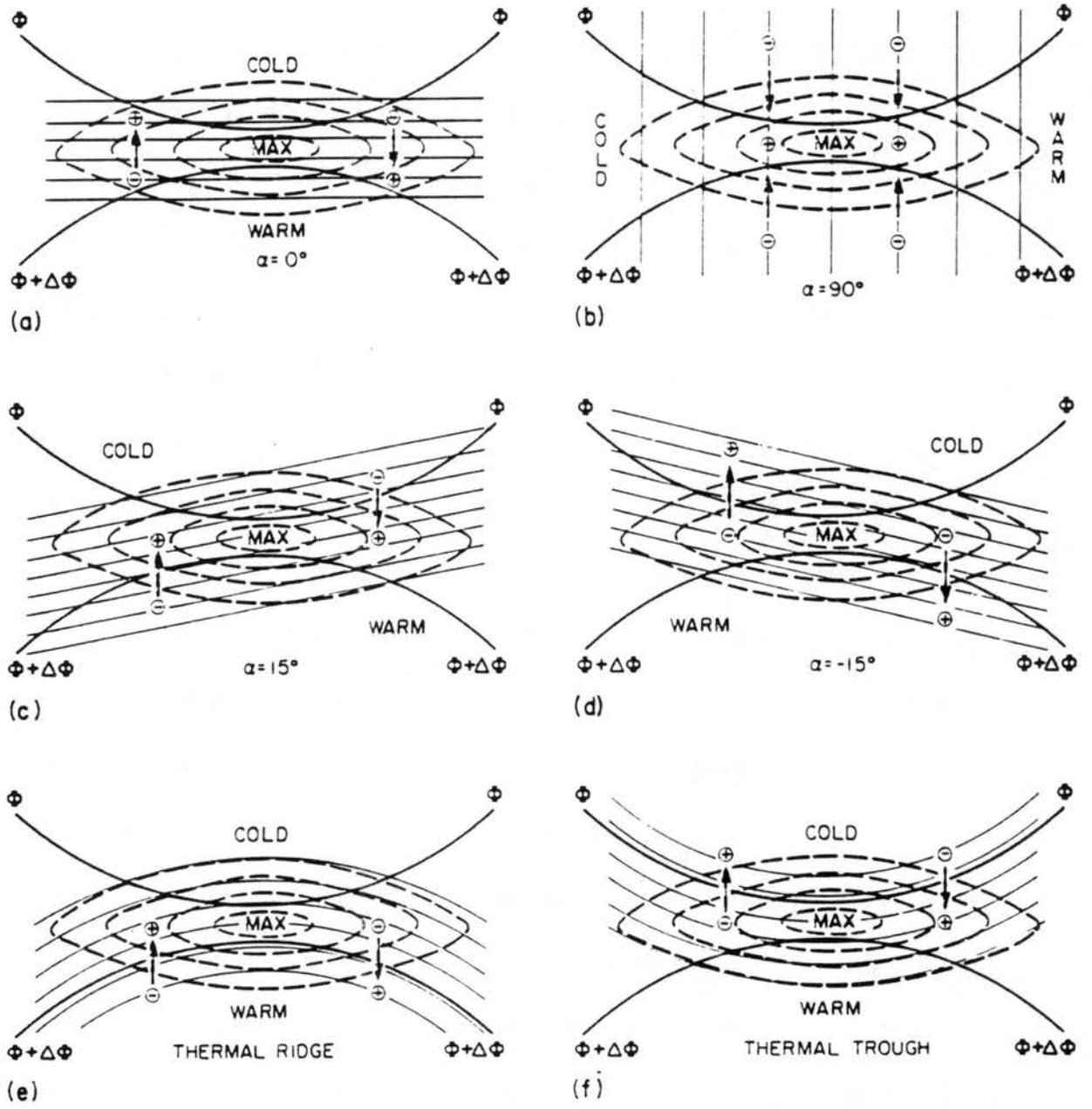

Figure 4.2 Schematic of various idealized configurations of potential temperature field for a straight jet streak system. Thick solid lines, geopotential height; thick dash lines, along-jet geostropic wind; thin solid lines, isentropes; thick solid arrows, transversely ageostrophic wind at level of jet streak core; + and -, pressure-coordinated vertical velocity. (From Keyser and Shapiro, 1986; originally adapted from Shapiro, (1983).

elliptical circulation with a relatively small (large) aspect ratio; (2) the baroclinicity determines the tilt of the circulations from the vertical. The interpretations of the forcing terms in the Sawyer-Elliassen secondary circulation equation shows the importance of the contributions from the geostrophic advection of wind and thermal fields (Shapiro (1981), Keyser and Shapiro (1986)).

In Shapiro (1981) the diagnostic analysis of frontal evolution forced by a strong geostrophic stretching deformation shows a clearly-defined direct circulation cell in the troposphere and lower stratosphere (as shown in Figure 4 of Shapiro, 1981). The cross-jet distance between the maximum ascent ($\leq$ -0.7 μb/s) and maximum descent ($\geq$ 0.8 μb/s) was about 1100km. Analyzing a case forced by strong shear, Shapiro (1981) further shows a thermally indirect circulation forced by a negative shearing deformation which has the same magnitude as the thermally direct circulation produced by the positive stretching deformation, and therefore qualitatively shows the significance of the shearing deformation of along-front thermal gradients as a secondary circulation forcing factor. However, in this latter case the cross-jet distance is only 250km between the maximum upward motion ($\leq$ -4.9 μb/s) and the maximum downward motion ($\geq$ 5.6 μb/s), Shapiro (1981) also presents a typical jet-front divergence value of order $10^{-4}s^{-1}$ associated with cross-jet ageostrophic air motions migrating over a cross-jet distance of 100km at the speed on an order of 10m/s.

The above studies have adopted the common assumption that the ageostrophic circulations are confined to the cross-jet plane and the along-jet wind is approximately geostrophic in cases of straight jet. Shapiro and Kennedy (1981)

questioned the application of this assumption based upon aircraft observations of a jet-streak system entering a sharply curved trough of a large amplitude synoptic wave. Along-jet ageostrophic motions can be produced by along-flow variations of the curvature by using the concept of gradient winds. In Figure 4.3b, an idealized case of a jet stream with constant speed is embedded within the trough of a stationary synoptic wave. The cross-jet ageostrophic circulation in a conventional model(Figure 4.3a) does not exist any more, instead, an along-jet ageostrophic circulation is produced. Air converges on the left side of the trough and diverges on the right side of the trough. So, if a jet streak exit area is close enough to the trough, the convergence upstream of the trough can compensate the divergence on the cold side and strengthen the convergence on the warm side of the jet streak in the upper troposphere. The validity of the geostrophic assumption should be carefully considered in this kind of case.

Japan is located in an active cyclogenetic area. The jet stream, a major factor in the evolution of cyclones, is frequently observed above this area, especially in the winter and spring seasons. Fukao et al (1991) utilized this geographic advantage and carried out measurements of vertical circulations associated with jet stream systems for 14 cases near Kyoto, Japan. In most of the observations, a clear reversal of the vertical velocity sign at or near the maximum horizontal wind speed with a descent motion below the jet and ascent motion above the jet was revealed. The magnitude of the 4-day averaged ascending and descending motions based on the radar observations generally fell into the range of 10-20 cm/s when the horizontal speeds

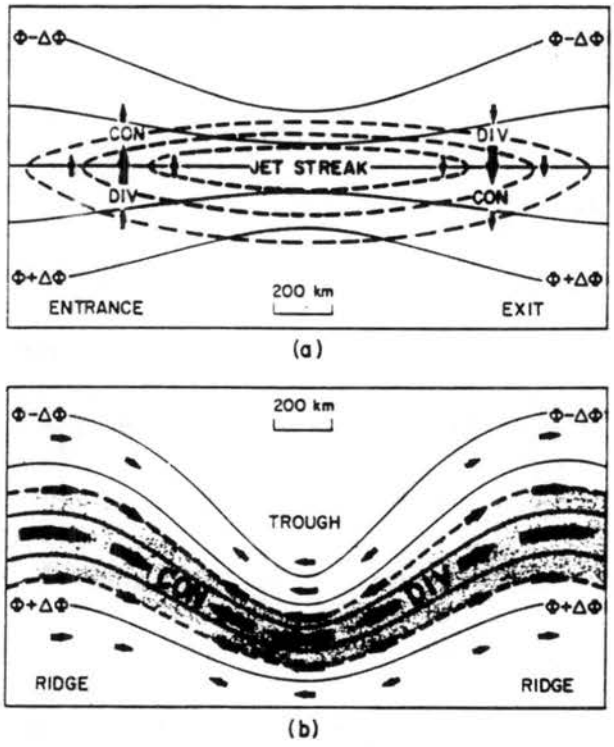

Figure 4.3 Schematic of the ageostrophic winds (heavy arrows) and the divergence structure in the vicinity of a)straight jet-streak system, and b) uniform jet within a stationary synoptic wave. Solid, geopotential height; dash, isotachs; shaded area, area of wind speed > 50m/s. (Shapiro and Kennedy, 1981).

exceeded 60m/s. Both these ascending and descending motions have depths larger than 5km. Since the locations of the observation site relative to the jet were not defined in the paper, we can not compare these observations with the conceptual model of a jet streak mentioned previously. The four-day averaged vertical velocity profiles may also cancel out some of the vertical circulation features of a jet streak since the life-cycle of a jet-streak or jet-front system is usually shorter. In spite of this, the discovery of strong vertical motions above the jet is consistent with the hypothesis of Namias and Clapp (1949), and Mattocks and Bleck (1986) about the

existence of stratospheric ageostrophic circulation above the jet besides the tropospheric ageostrophic circulation below.

The recent observations of the transverse circulation of a jet stream by Yoe and Ruster (1992) were carried out using a 5-beam VHF radar at the frequency of 53.5MHz. Due to the errors caused by a misaligned vertical beam and to the short time period (< 1day) average of w, a VAD technique was applied to calculate w based on the four oblique beam radial velocities. As well as giving the same vertical velocity reversal features as those in Fukao et al (1991), the authors took a closer look at the temporal change of the vertical circulations. It was concluded that the magnitude and sign of the averaged vertical motion is strongly time-dependent, which indicates the importance of the location of the observation site relative to the jet system. It is also noted that the maximum vertical velocities observed in this case were about three times larger than that reported by Fukao et al. (1991). The observed vertical motions above the jet occupied a layer about 6-7 km depth. The maximum horizontal wind speed for onset of the reversal of w was lower (down to 30m/s); Fukao el al. (1991) reported 60 m/s. Yoe and Ruster (1992) attribute this discrepancy to the fundamental differences of the jet system in those two cases and to the different length of the data averaging period.

In the next chapter, analysis of the ageostrophic motion and the associated vertical motion in the exit area of a jet streak will be given based on the wind profiler and rawinsonde data. The comparison between these observations and the previous

studies will further establish the validity of the jet streak conceptual model and the specific characteristics of the 26 November jet streak case.

4.2 Cirrus Clouds

While each stage of cirrus cloud evolution is decidedly affected by the temperature structure, moisture distribution, microphysical characteristics and air motions complex and interactive physical processes complicate a complete understanding of the cloud layer development. The static stability, relative humidity structure, vertical velocity and horizontal shear found in cirrus cloud systems will be discussed.

Yagi (1969) using stereophotogrammetric observations of cirrus clouds at Sapporo, Hokkaido during the fall season concludes: 1) cirrus clouds are located in a layer with dry adiabatic lapse rate and strong vertical shear of horizontal wind; 2) cirrus uncinus has remarkably stable layers above and below the neutral cloud layer and the trails are in the lower stable layer; and 3) cirrus fiblatus and spissatus have a very stable layer just above the cloud, however, the layer below the clouds is not as stable as upper stable layer. In a study by Heymsfield (1975), the cirrus uncinus head was reportedly found to exist in a region with a dry adiabatic lapse rate and with two stable layers directly above and below. Analyzing 3600 middle and high cloud cases from rawindsonde data at 24 locations in U.S.A. during 1977, Starr and Cox (1980) reported that, for thick cloud (cloud depth > 50mb), there is a decrease of static stability with height from subcloud layer to the above cloud layer, with a typical potential temperature change of 5K/km in the subcloud layer, and 3K/km near

the cloud top. However, for thin clouds (cloud thickness < than 50mb), an opposite result was found with the greatest stability above the cloud layer (possibly the tropopause) and lesser stability in and below the cloud layer. Among recent studies, Starr and Wylie (1990) investigated the thermal structures of several distinct mesoscale cirrus cloud cases. One of the significant features found was the existence of an upper stable zone (USZ) between the tropopause and the cloud top, and a lower stable zone (LSZ) below the cloud fallstreak layer. A vertical gradient of horizontal temperature advection was offered as the explanation for of this type of static stability structure. Combining vertical motion patterns and regional atmospheric thermodynamic structures, Starr and Wylie (1990) summarized; below a LSZ, relatively cool and dry air was descending and above the LSZ, relatively warm and moist air was ascending. Mesoscale cirrus clouds were produced in the upward motion layer above the LSZ.

In a mesoscale model of cirrus clouds reported by Starr and Cox (1985a), the initial temperature profile was set up with a lapse rate equal to the pseudoadiabatic lapse rate Γ_m=8.7°C in the cloud layer, a weakly stable lapse rate $\Gamma=\Gamma_m$ -1.5°C km^{-1} below the supposed cloud layer, and a more stable layer with $\Gamma=\Gamma_m$-4.0 °C km^{-1} above the cloud layer. The simulated cirrus cloud structure produced by their model agrees quite well with comparable observations.

A general picture of the atmospheric thermal stability associated with cirrus clouds emerges: cirrus clouds are usually located in a layer which is statically unstable with a very stable layer above and a slightly stable layer below; thick cirrus

clouds, as defined in Starr and Cox (1980), may grow in a near stable layer with more stable layer below and less stable layer above. Considering the cirrus cloud types, Cotton and Anthes (1989) conclude that absolutely stable layers are associated with cirrostratus clouds, while cirrus and cirrocumulus clouds occur when the lapse rate exceeds the moist adiabatic lapse rate.

Effects of vertical shear of horizontal winds have been frequently found in cirrus cloud cases. Heymsfield (1975), concludes that wind shear can strongly modify the structures of cirrus clouds by blowing ice particles out of the generating cells. Many variations of cloud trails can be produced depending on the wind shear (Cotton and Anthes, 1989). Other studies have been concentrated on the microscale effects of shear on the cirrus clouds. By producing TKE (Turbulent Kinetic Energy), shear enhances the vertical mixing at cloud boundaries and therefore the entrainment/detrainment process. Studies on the role of the shear in stratocumulus turbulent kinetic energy budgets were performed by Brost et al. (1982). However, there is a lack of this kind of direct study for cirrus cloud cases, although this effect may be important for understanding cirrus cloud formation/dissipation processes.

Nevertheless, the turbulent structures in cirrus clouds have been reported. In their studies of aircraft data on perturbations of temperature, horizontal and vertical wind field, Dmitriev et al.(1984) found that the profiles of these three parameters have a similar pattern in a cirrus cloud system. The intensity of these perturbations is highest in the middle of the cirrus cloud and lowest at the top and bottom. The mean turbulence intensity above the cloud is slightly higher than that below the cloud.

It is also noticed that the cloud itself dominated by turbulence 75-90% of the time.

Flatau (1990) studied two data sets: Global Atmospheric Sampling Program(GASP) data set and FIRE I data set. Their results were: the cirrus clouds develop in a stably stratified upper troposphere; the wind perturbation is the strongest inside the cloud and close to the cloud base; strong shear effects do exist, but the strength may change with seasons and latitude; and the convection induced buoyancy may change with seasons and latitude also.

Quante and Brown (1993) also showed stronger turbulence (variabilities both in the vertical and horizontal winds) at lower levels inside and beneath the cloud layer than that at and above cloud top. They concluded that environment of cirrus clouds in the vicinity of a jet stream or a front is most likely conducive to Kelvin Helmholy Instability (KHI). A detailed study of the relation between high level billow clouds and clear-air turbulence driven by strong vertical shear in a stably stratified fluid is given by Ludlam (1967). He concluded that, besides developing in a layer with large- or intermediate-scale ascending motions or orographic waves, billow clouds can also form in a statically stable, but, dynamically unstable (due to the existence of wind shear) layer with a group of amplifying waves present. K-H waves can cause a cat-eye structure (Figure 15 in Ludlam, 1967) and actually produce lifting condensation. Billow clouds form at the top of the cat-eye. In a layer which is very dry, Ludlam (1967) concludes that the waves can barely produce clouds, but still produce clear-air turbulence.

Vertical velocity considered as one of those important forcing factors has been carefully studied. It is generally considered that ascending motions correspond to cloud forming process via transferring moisture upward and cooling air temperature through expansion. An opposite process happens to descending motions which correspond to the cloud dissipating process.

Starr and Cox (1985b) performed a sensitivity analysis of large scale vertical motions in their numerical experiments on the formation and maintenance of cirrus clouds. Only strong large scale vertical motions, (>10cm/s) produced cloud structures consistent with the observations. The simulations of the negative and zero vertical motion cases show that there are significant variations of the ice water content due to microphysical effects. It was concluded that large-scale ascending motion of 2cm/s is sufficient for maintenance of a cirrus cloud layer. However, when dry air entrainment at cloud top is considered, Starr and Wylie (1990) argues that a mean upward motion of between 2cm/s and 5cm/s is quite reasonable for mesoscale cirrus clouds.

Starr and Wylie (1990) applied an adiabatic method to derive the vertical wind velocity of cirrus cloud cases from sounding data. Their results demonstrate a good correspondence between ascending (descending) motions and clear/clearing (forming/maintaining) conditions. They reported the approximate range of ± 10cm/s for the large scale vertical motion. Starr et al.(1993a,b) applied the same adiabatic method to study the cirrus cloud cases during FIRE II. The results exhibit the

existence of cloud-scale horizontal variations of the vertical wind field. In these cases, upward motions dominate the cloud layers with a maximum value of 14cm/s.

Gultepe et al. (1990) calculates cloud scale vertical velocity of FIRE I cirrus cloud cases. They utilized the mass continuity equation and divergence measurements from aircraft spiral descents and conical Doppler lidar scans. Large magnitude vertical velocities were found with a maximum value of about 40cm/s. Gultepe and Starr (1992) attempts to utilize total water mass conservation and heat conservation equations to calculate vertical air motion required to balance those budgets. Their results indicate cloud-scale vertical velocities of the order of a decimeter; this is similar to that reported by Heymsfield (1975) based on the aircraft and Doppler radar measurements. Heymsfield (1975) reported horizontal variations of the vertical velocity field for a case of cirrus uncinus; updraft velocities were generally in the cloud head and downdraft velocities were found in the cloud trail.

While studying the effect of large scale vertical motion forcing, Cotton and Anthes (1989) reported that cirrus clouds with precipitation will develop under large adiabatic cooling effects caused by long period, strong ascending motions (>=10cm/s); when vertical motion is weak (1-2cm/s), radiative effects become relatively more significant and internal convective circulations in the cloud layer are created by the radiative cooling at cloud top and warming at cloud base, which will destablize the cloud layer.

Chapter 5

OBSERVATIONS AND ANALYSIS OF 26th NOVEMBER, 1991 CASE

In this chapter, jetstream-cirrus cloud system of November 26, 1991 will be analyzed. Specifically, moisture structure, and static and dynamical instability structures of this cloud system will be analyzed from rawinsonde data. The correlation between the atmospheric thermodynamical structure and wind profiler signal return will be used to interpret the radar echo mechanisms. The ageostrophic circulation of a jet streak system and the vertical air motion transfer property associated with the cirrus cloud system are of particular interest in this chapter and will be studied by utilizing NWS rawinsonde network data and high temporal and spacial resolution wind profiler data. Meanwhile, the wind profiler performance in vertical wind field measurement will be tested through the intercomparison among different methods of deducing vertical velocity and comparisons with previous observational and theoretical studies.

5.1 Synoptic Features

The surface weather on November 26, 1991 was dominated by a cold front over the state of Wyoming and a warm front in the Kansas and Missouri area. The 200 mb chart (Figure 5.1) shows a low amplitude large scale trough over the central U.S. and a ridge on the west coast. This trough-ridge structure began to strengthen at 00Z on November 27th. A jet streak approaching Kansas-Oklahoma-Texas region

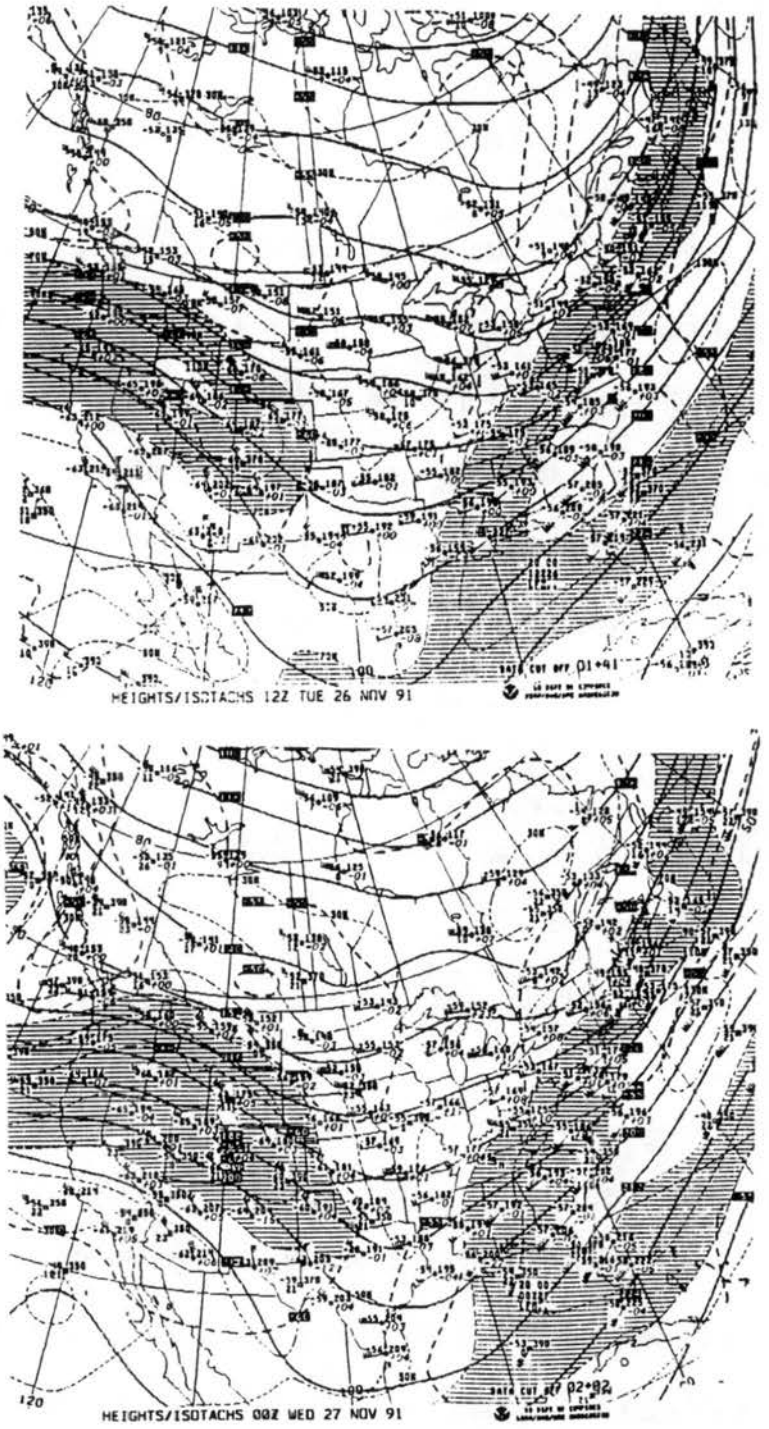

Figure 5.1 NWS upper air sounding of a) 12Z, Nov. 26th; b)00Z, Nov. 27th

was visible on the 1200Z 200mb map. This system reached the central part of Texas by 0000Z of November 27. A cross-section analysis normal to this jet streak (Figure 5.2) shows a maximum wind of 36m/s at 250mb at 1200Z of November 26. This maximum wind increased to 40m/s by 0000Z of November 27 and the upper level subtropical jet was between 250mb and 200mb at this time. These features are consistent with the daily mission summary of the FIRE II project, which states that the upper level winds were generally northwesterly over the western U.S. on November 26. While a shift to southwesterly wind was reported at Topeka, Kansas around noon of November 26 with the maximum wind speeds of 25m/s at the tropopause, the wind at Dodge City, Kansas remained northwesterly. At 1800Z, wind speeds had increased to 65 knots at Topeka and 115 knots at Dodge City with almost no change in direction. At the same time, the tropopause height increased to the 11.5km. In association with this dynamical feature, a baroclinic leaf feature also developed over the central U.S. with its tail extended into western Oklahoma. Cirrus, middle level, and low level clouds were observed accompanying this baroclinic system.

5.2 Observations of Clouds

NASA Langley's 8" cloud lidar system at the Parsons site received its first detectable cloud signal at about 1655Z on November 26 (Figure 5.3). The cloud had a uniform thickness of 200 to 300m in the first 20 minutes of the observation, and then developed rapidly in thickness but the cloud top height remained constant at about 10km till 2010Z on November 26. Video-All-Sky camera observations also indicated that the clouds were optically thin at the beginning and blue sky was visible

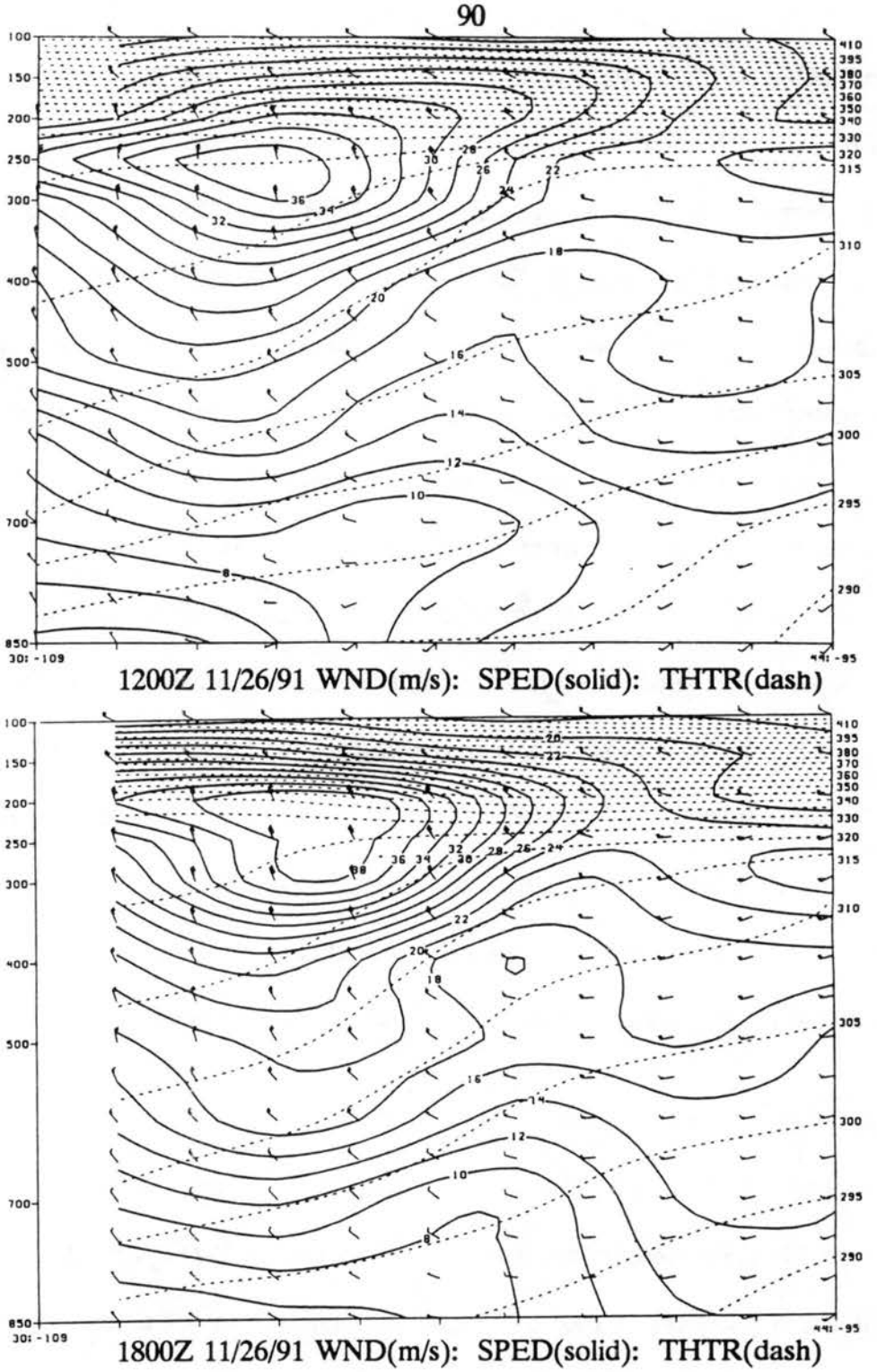

Figure 5.2 Cross section normal (30°; -109° to 44°; -95°) or horizontal wind apeed (m/s, solid), potential temperature (°K, dash) and wind bar (m/s).

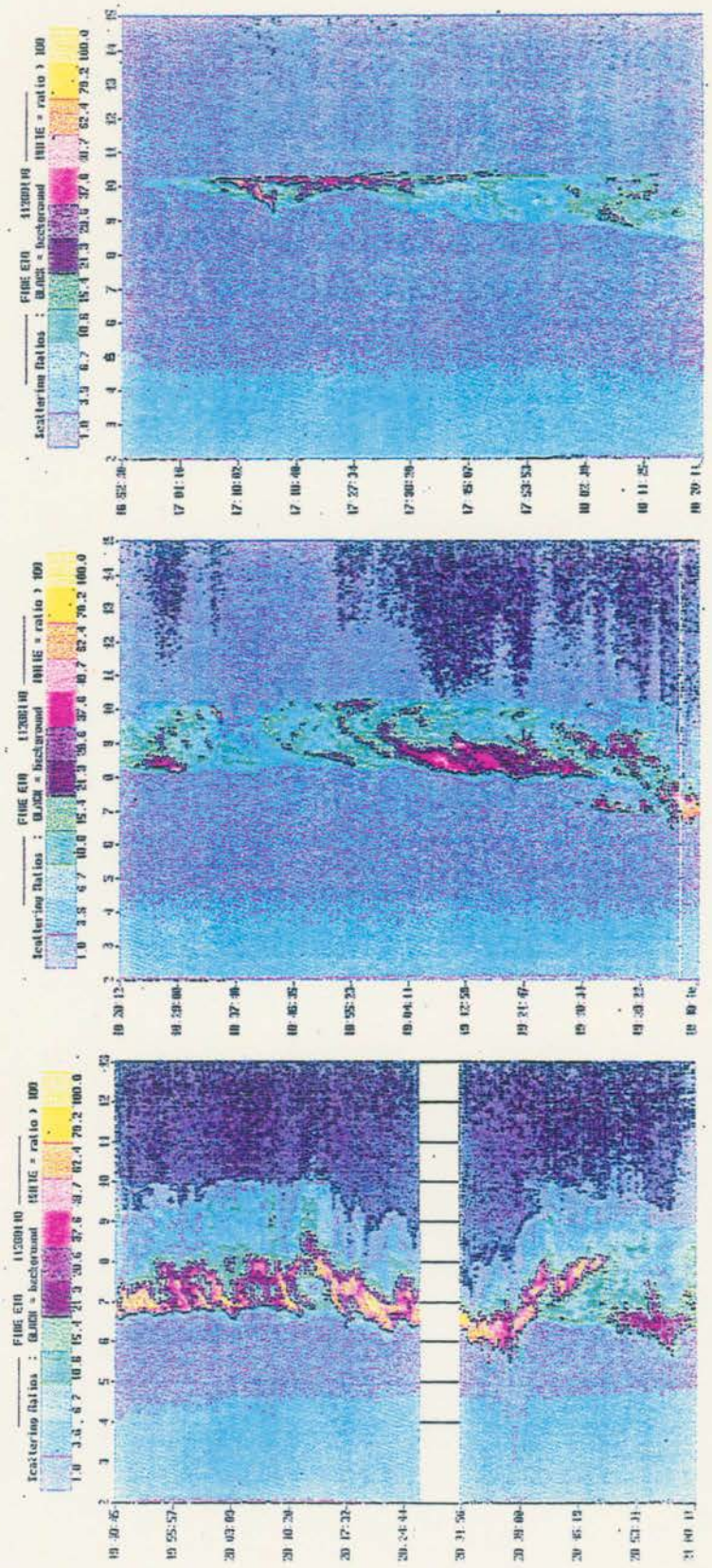

Figure 5.3 Time-height observations of the cloud layer from NASA Langley 8" lidar system at Parsons, Kansas on November 26th, 1991.

behind it. From about 1704Z to 1730Z, the cloud had a depth of 500m with a high lidar backscattering ratio. By 1800Z, the cirrus cloud was located approximately between 8.7km and 10.1km, and became much thicker in the local afternoon. By 1930Z, multi-layered cloud conditions and middle clouds were reported by the lidar. About 40 minutes earlier, the CO_2 lidar at the Coffeyville experiment site (southwest of Parsons) started reporting cirrus cloud returns at 10km AGL (Above Ground Level) with an approximate depth of 200m (Intrieri et al., 1992). Their later observations of the cloud system change based on a K- band radar, CO_2 lidar and infrared radiometer show a general agreement with the observations of NASA Langley's 8" cloud lidar.

The GOES 7 satellite infrared images showed that this high cloud system was approaching the central U.S. from the north-west in the early morning on Nov. 26 with another cloud system trailing behind. No high cloud conditions were observed in the area for several hundred kilometers between these two high cloud systems. The first system of high clouds corresponded to the jet streak system. It was moving at a slower speed on the northern edge and a faster speed on the southern edge, and finally passed through the trough and headed toward north-east. By 1600Z on the 26th, the cloud was mostly over Nebraska and Iowa, with only a narrow band extending over eastern Kansas with the southern edge close to the Oklahoma and Texas boundary.

5.3 Sounding and Stability/Instability

Rawinsonde data from Coffeyville were used to calculate the static stability, the vertical shears of the horizontal wind and the Richardson number. This data set

has a 5 mb vertical resolution which corresponds to a thickness range from 50m to 150m in the atmosphere between 13km and the surface. The larger layer thicknesses in both the upper troposphere and lower stratosphere can strongly affect the Richardson number calculation and therefore the K-H instability estimate.

There are six soundings, at 0054Z, 0537Z, 1415Z, 1716Z, 2025Z and 2330Z, from the November 26 case. The sounding taken before and at 1415Z did not have cirrus cloud present, while the sounding at 1716Z was in the middle of the most significant cirrus cloud event. The sounding at 2025Z contained middle level clouds as well. Figure 5.4 presents the temperature and dew point profiles for these sounding. The tropopause was located at 10.1km, 10.4km, 10.25km and 9.4km in the 1415Z, 1716Z, 2025Z and 2330Z soundings, respectively. At 1415Z an average lapse rate of 8.93 °K/km between 7.2km inversion and the tropopause was found. The average lapse rates between the temperature inversion in the middle troposphere and the tropopause for 1716Z and 2025Z soundings were 8.89 °K/km and 8.36 °K/km, respectively. While cirrus cloud tops generally stayed near a temperature of -56°C, the cloud base temperature varied with height. The cloud base temperatures increased from -48°C to -30°C when the cloud base moved from 9km at 1716Z to about 7km at 2025Z. At 2330Z, high cloud disappeared and the remaining cloud had a cloud top temperature of -50°C and a cloud base temperature of -35°C.

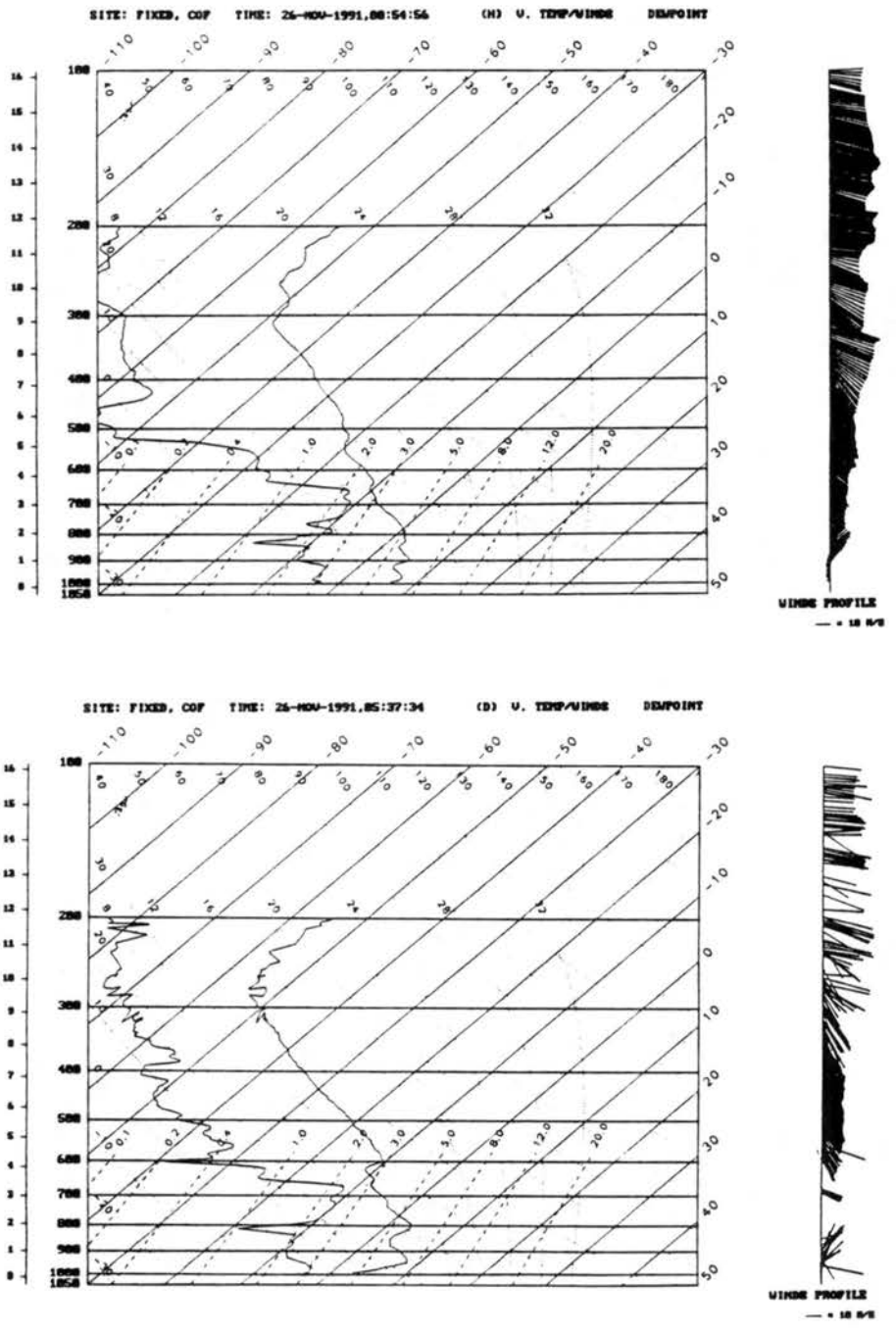

Figure 5.4 Sounding at Coffeyville (Kansas) on November 26, 1991.

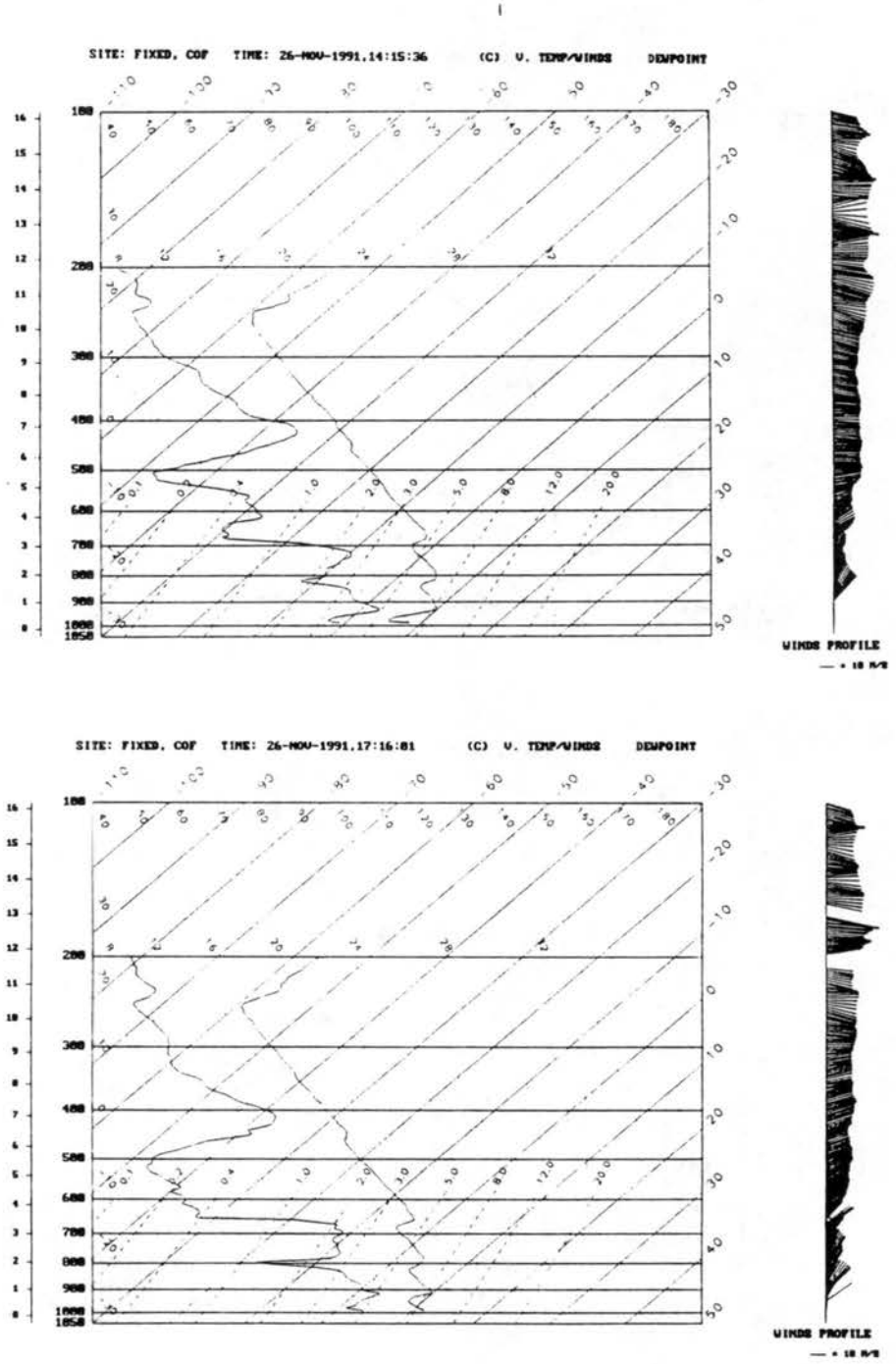

Figure 5.4 continued

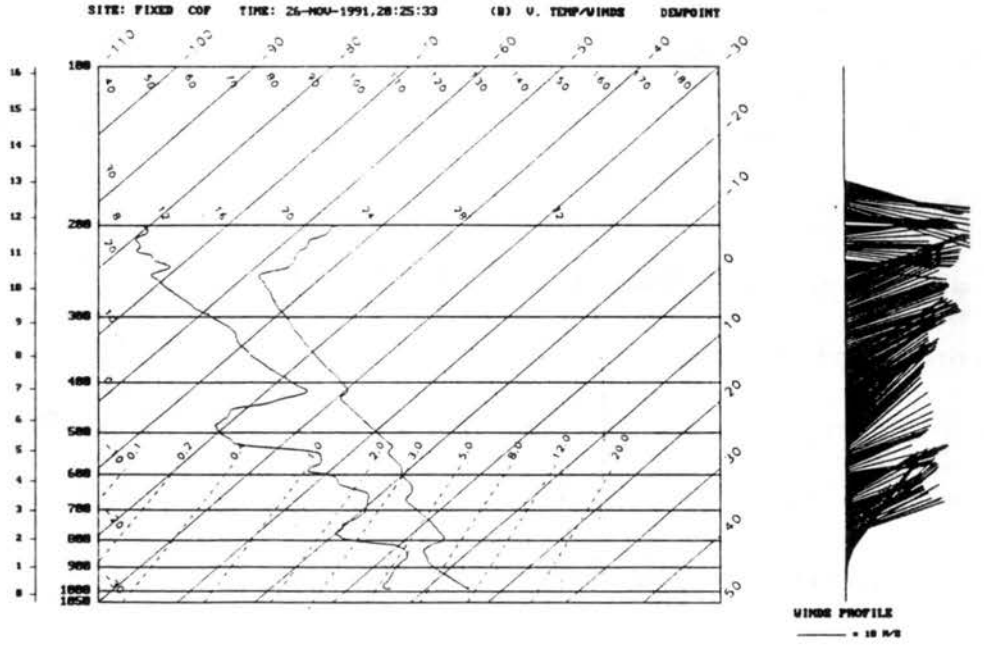

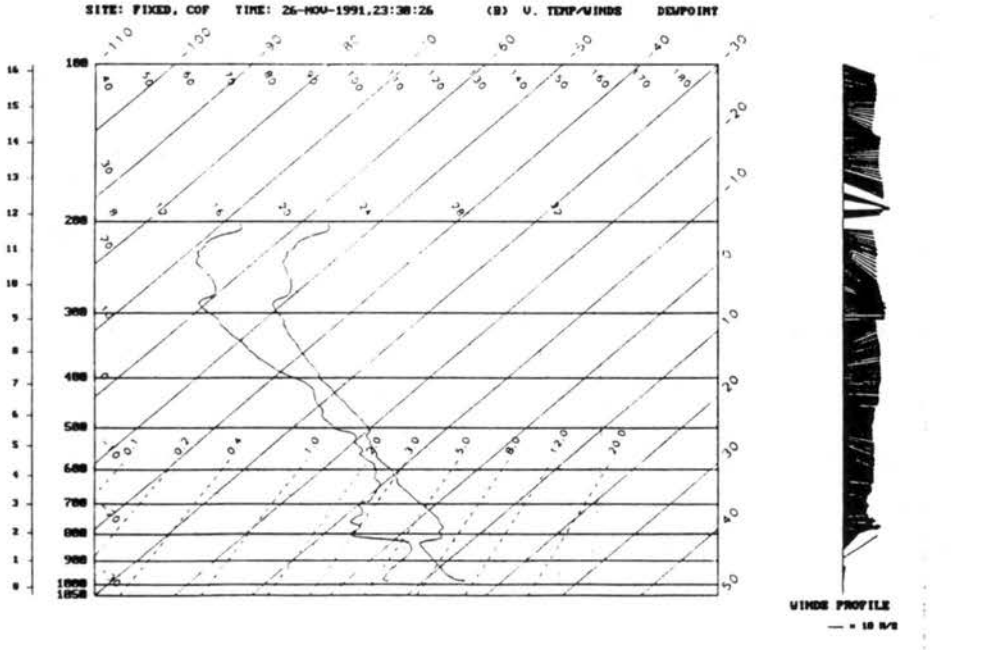

Figure 5.4 continued

The soundings at 0054Z and 0537Z exhibit a dry atmospheric layer above 650mb. Starting from about 1100Z (sounding of ARK, not shown here), a relatively humid layer above 420mb (at about 7km) developed with a much drier layer below; these features are apparent in the 1415Z, 1716Z and 2025Z soundings. The relative humidity (RH) profiles in Figure 5.5 shows a minimum at 5.5km and rapid increases of RH above serving as a precursor to developing cirrus clouds. The maximum RH was located around the 7km level which was below the cirrus cloud layer. During the entire period, the temperature profiles did not change very much and only weak warm air advection could be marginally detected. Uccellini and Johnson (1979) state: "advection of cool, dry air associated with strong westerly winds in the middle troposphere and the rapid northward movement of a tongue of warm, moist air in the low troposphere creates favorable conditions for deep convection. ... The likelihood of convection is increased with strong veering of winds...". The conditions of November 26 do not favor convection according to the above description and the vertical wind field which will be discussed later does not show any supporting features either. It is therefore anticipated that horizontal advection brought moisture into the upper layer. The relative humidity contours at 400mb (Figure 5.6) show a maximum RH above Idaho at 1200Z and moving into South Dakota at 1800Z. Therefore, the RH values generally decreased toward the southeast and moisture was advected by the northwesterly winds into the dry area during the precursive and the developing periods of the cirrus clouds over southeastern Kansas. By 2330Z, the dry

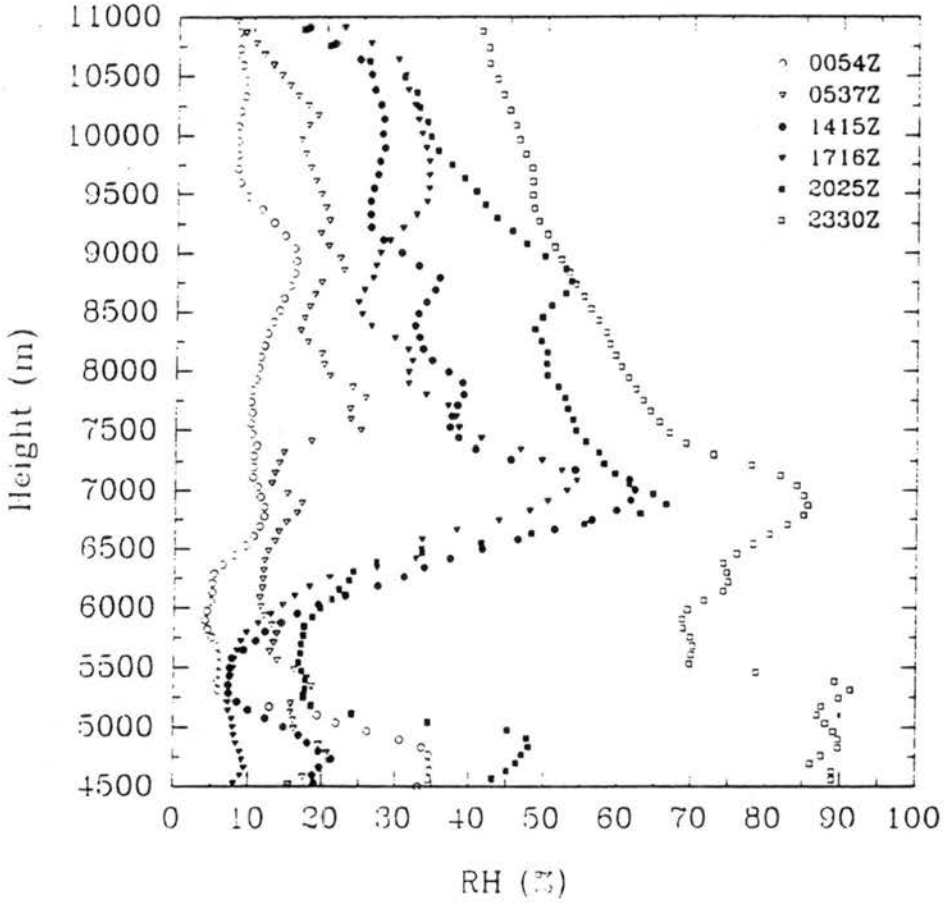

Figure 5.5 Relative Humidity (RH) profiles from the soundings at Coffeyville on November 26, 1991. The filled symbols presents the RH profiles during the period of cirrus clouds.

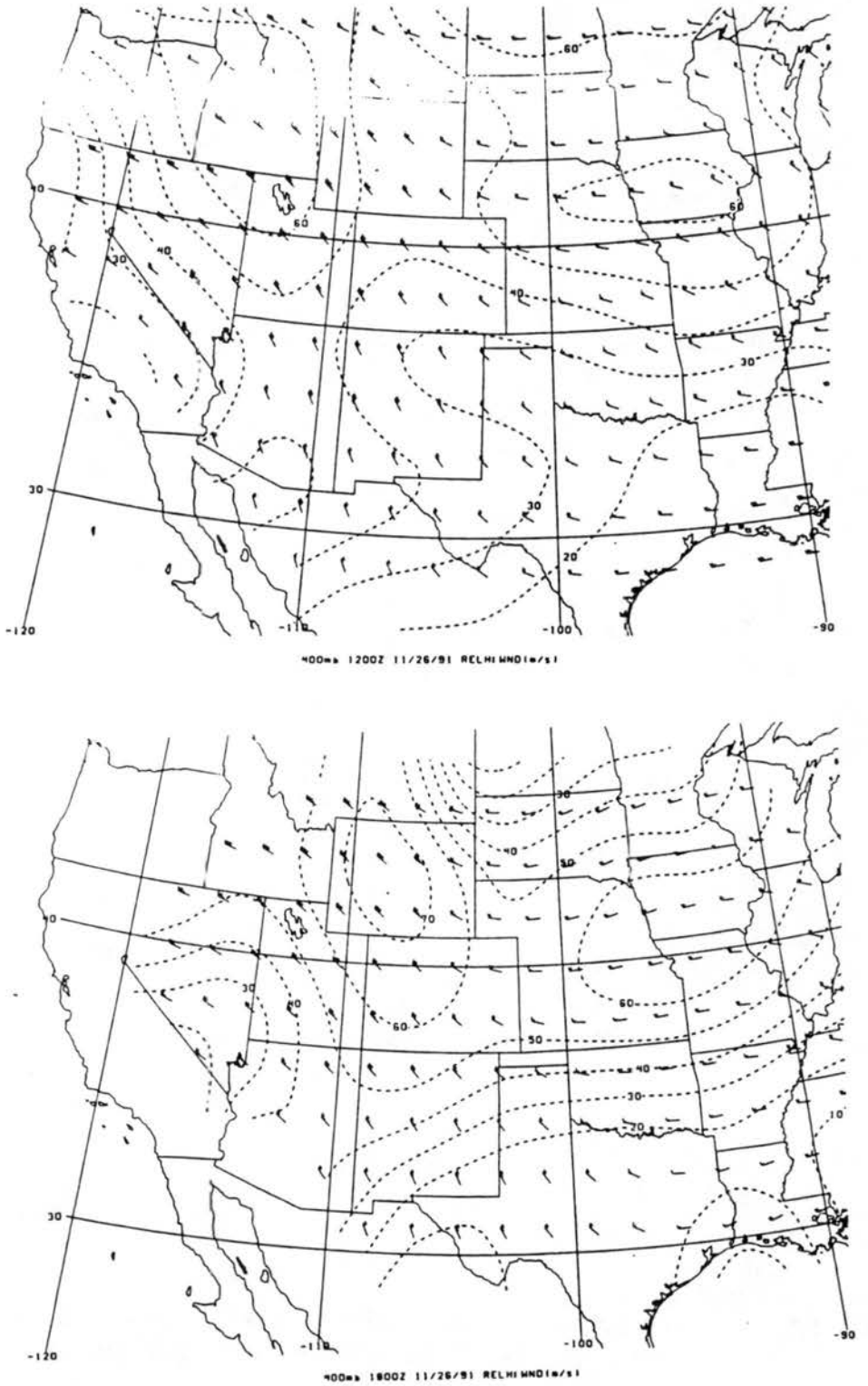

Figure 5.6 Relative humidity (dash lines) and winds on the 400mb surface from the upper air sounding data at 1200Z, 1800Z on November 26, 1991.

atmospheric structure in this region had been replaced by a nearly saturated atmosphere.

Potential temperature profiles were calculated from the six soundings shown in Figure 5.7. A step-like potential temperature gradient is evident at about 10.4km from 1415Z, 1716Z and 2025Z sounding (solid symbols) which are closely related to the cirrus cloud system. Below 10.4km, the atmosphere is nearly well-mixed in a 3.5km thick layer with a potential temperature gradient of only 1.4 °K/km; this is consistent with the initial value of 1.67 K/km at the cirrus cloud layer used by Starr and Cox (1985). The potential temperature lapse rate above 10.4km is about 34°K/km; this is significantly larger than the gradient of 7.1°K/km above the cloud layer reported by Starr and Cox (1985). The potential temperature lapse rate of the layer below the nearly neutral layer is still quite low and is close to the (Starr and Cox) value of 4.33°K/km Recalling from the mechanism of radar echoes, large radar refractivity gradient is expected around the 10.4km layer. Strong buoyancy effect, which is proportional to the potential temperature gradient, is also anticipated at this level.

Figure 5.8 shows the vertical shear profiles of the horizontal winds. While there are very strong shears throughout the atmosphere at 0054Z, the 0537Z sounding shows a stronger wind shear between 8.5km and 12km with relatively weaker shear below. The 1415Z and 1716Z plots, corresponding to the presence of cirrus, show an obvious decrease of shear below the 10.5km level, which is just above the cloud top. This weaker shear was present in a deep layer from 6km to 10.2km

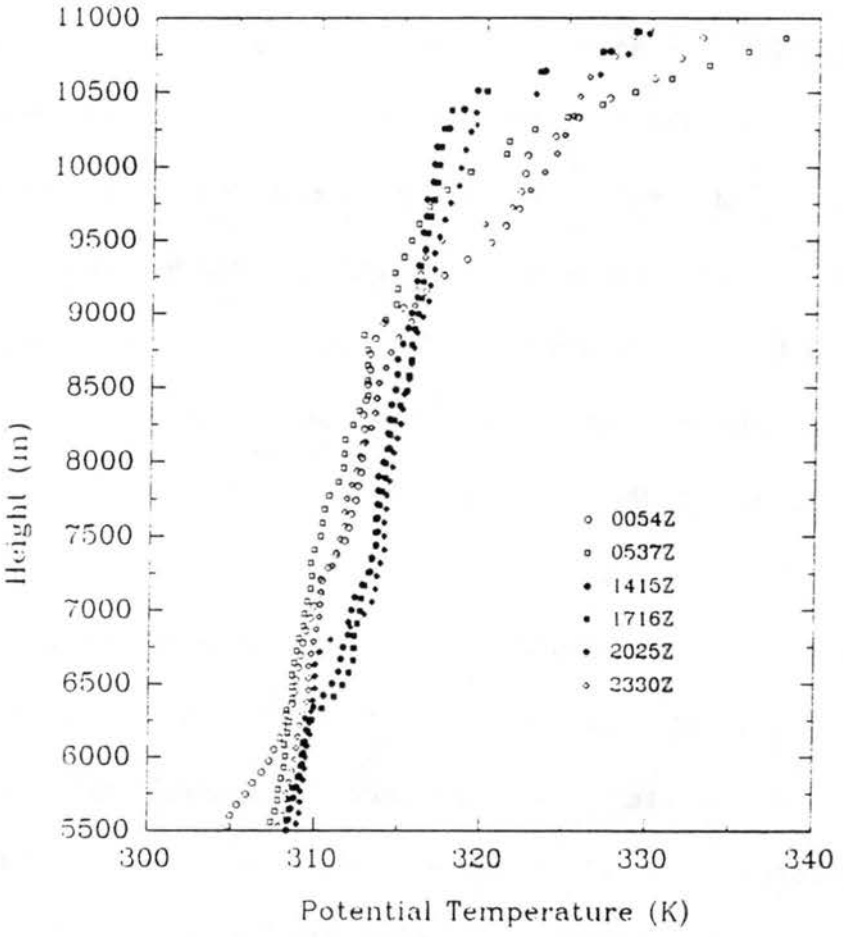

Figure 5.7 Potential temperature from the sounding at Coffeyville, November 26, 1991. The solid symbols represent the profiles measured when there was a cirrus cloud system.

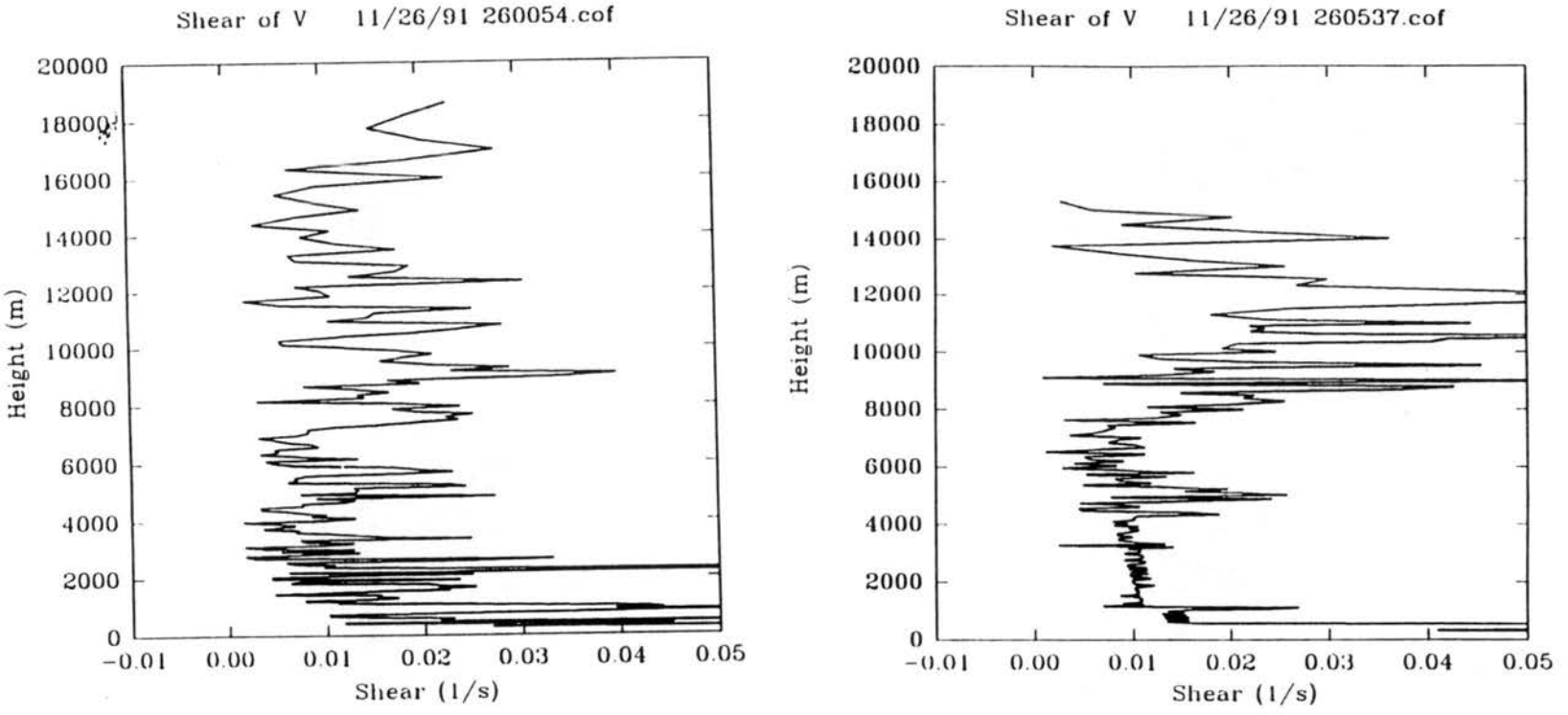

Figure 5.8 **Wind shear profiles calculated from the sounding in Figure 5.4.**

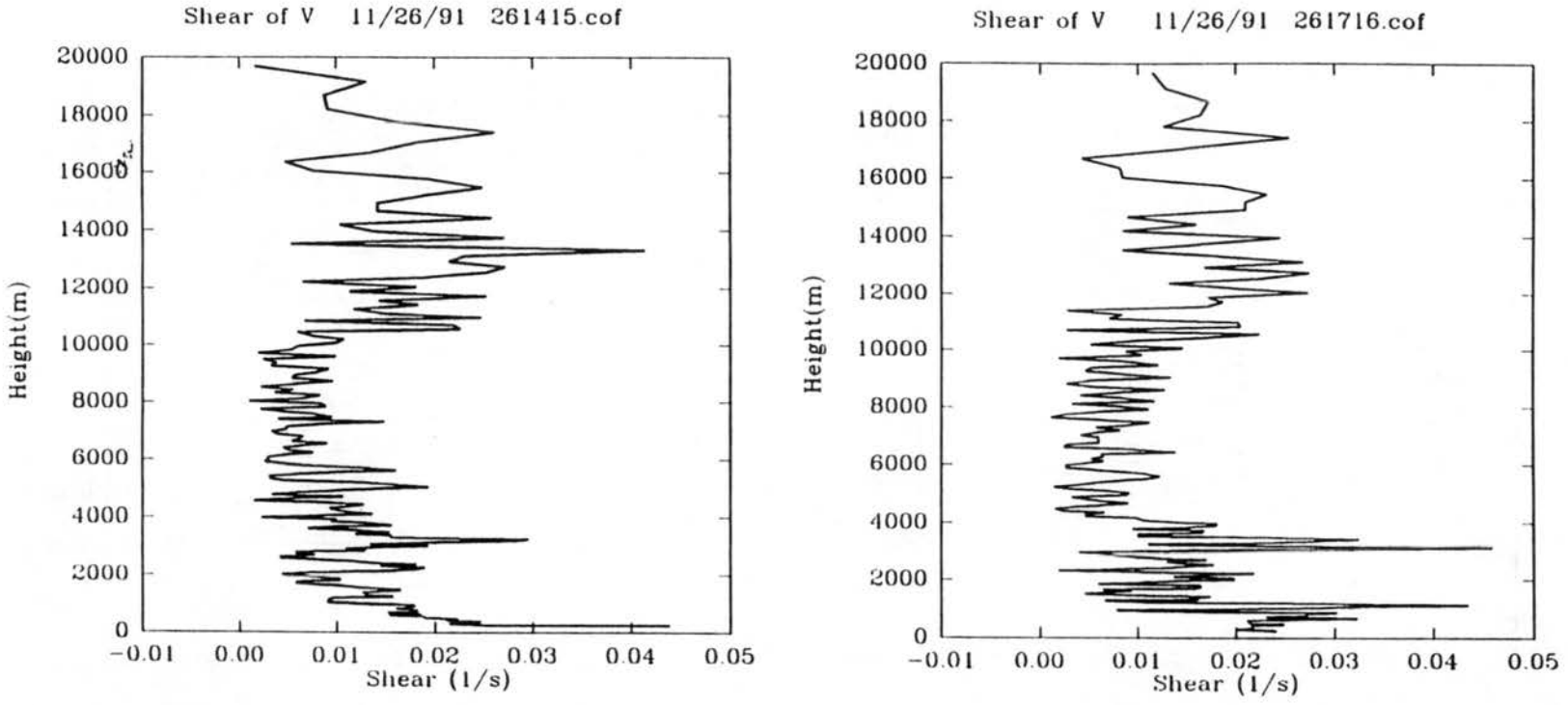

Figure 5.8 continued.

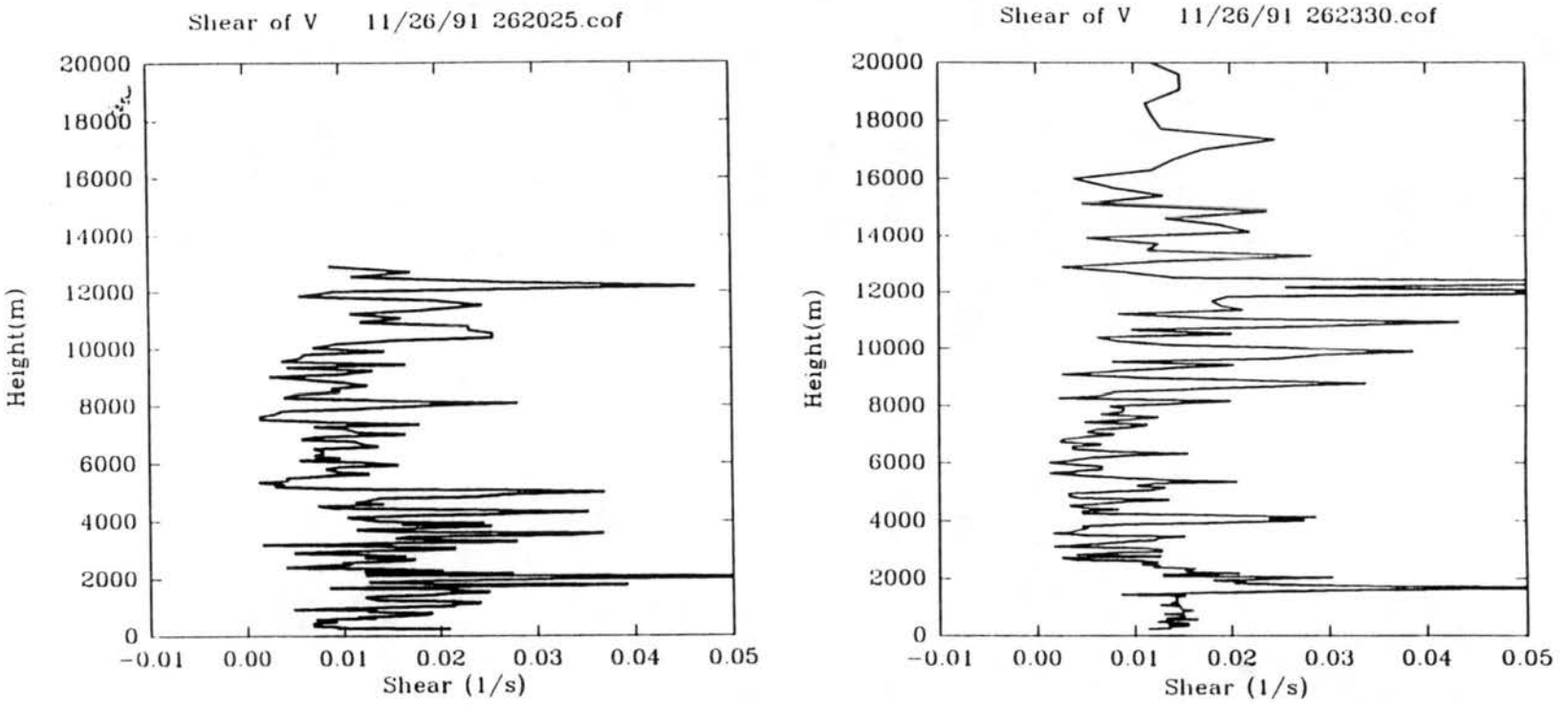

Figure 5.8 continued.

at 1415Z, and from 4km to 10.2km at 1716Z. At 2025Z, a weak shear layer still resided between 6km and 10km, but with an increased shear strength of 0.003 1/s. The 2330Z plot shows large changes in the shear profile compared to the previous plots and the weak shear layer is formed only between 6km and 8km. Above 8km, the shear is again stronger and has a layered structure, i.e., four relatively weaker wind shear layers are separated by three strong shear layers with thicknesses ranging from 0.5km to 0.8km. During the entire observation period, shear in the lower stratosphere had been much stronger than that in the middle and upper troposphere. Based on these observations, it is expected that there will be weaker shear-induced turbulence inside the cirrus cloud layers and stronger shear-induced turbulence above the cloud top level. However, the small buoyancy force in the cloud layer and large buoyancy effect in the lower stratosphere have made these interpretations quite uncertain.

Since the bulk Richardson's number is calculated using 5mb vertical resolution in this analysis, the critical value of 0.25 for the local gradient Richardson's number can not be applied directly to this case. In general, this critical value approaches 0.25 as the thickness of the layer decreases. In the study of Gyakum and Cai (1990), a critical Richardson's number of 1.0 is proposed for a reasonable probability for onset of turbulent activity when the average Richardson's number is calculated using 25mb thickness layers. Therefore, a critical Richardson number somewhat less than 1.0 should be applied in our study for the onset on turbulence.

Figure 5.9 shows the Richardson number profiles calculated from the six soundings of November 26. The three vertical dash-dotted lines are the 0.0, the 0.25 and the 1.0 lines, which are used to highlight the distribution of the Richardson number values in the sounding. The tropopause, the clouds tops and the cloud bases are marked based on both the sounding and the lidar observations.

The Ri profile at 0054Z shows a very deep layer ranging from 7.5km to 9.0km with Ri value less than 0.25. Above 9.0km, the Richardson number shows a slight increase until hitting the 10km level where Ri increases dramatically due to the increase of potential temperature gradient. By 0537Z, the deep layer with small Ri generally disappeared with only a small part remaining, and the Ri profile became highly variable. At 1415Z and 1716Z, Ri values changed dramatically from layer to layer and negative Ri values, which correspond to static instability, were found. From 2025Z, Ri profile became less varied again, but still quite active. The large Richardson numbers often found right above the tropopause, are explained by the large potential temperature gradients compensating the large wind shear effect in this region; therefore stratified flow should be expected in these layers.

While the Richardson numbers at the tropopause simply change between 0.25 and 1.5 during the period of these six sounding (indicating large vertical shear counterbalances the strong buoyancy effects), the Richardson number profiles related to the cirrus cloud system are more complicated. During the precursive and the developing period of the cirrus clouds, the 1415Z Richardson number profile shows large variations with height. Several layers with static instability are indicated (Figure

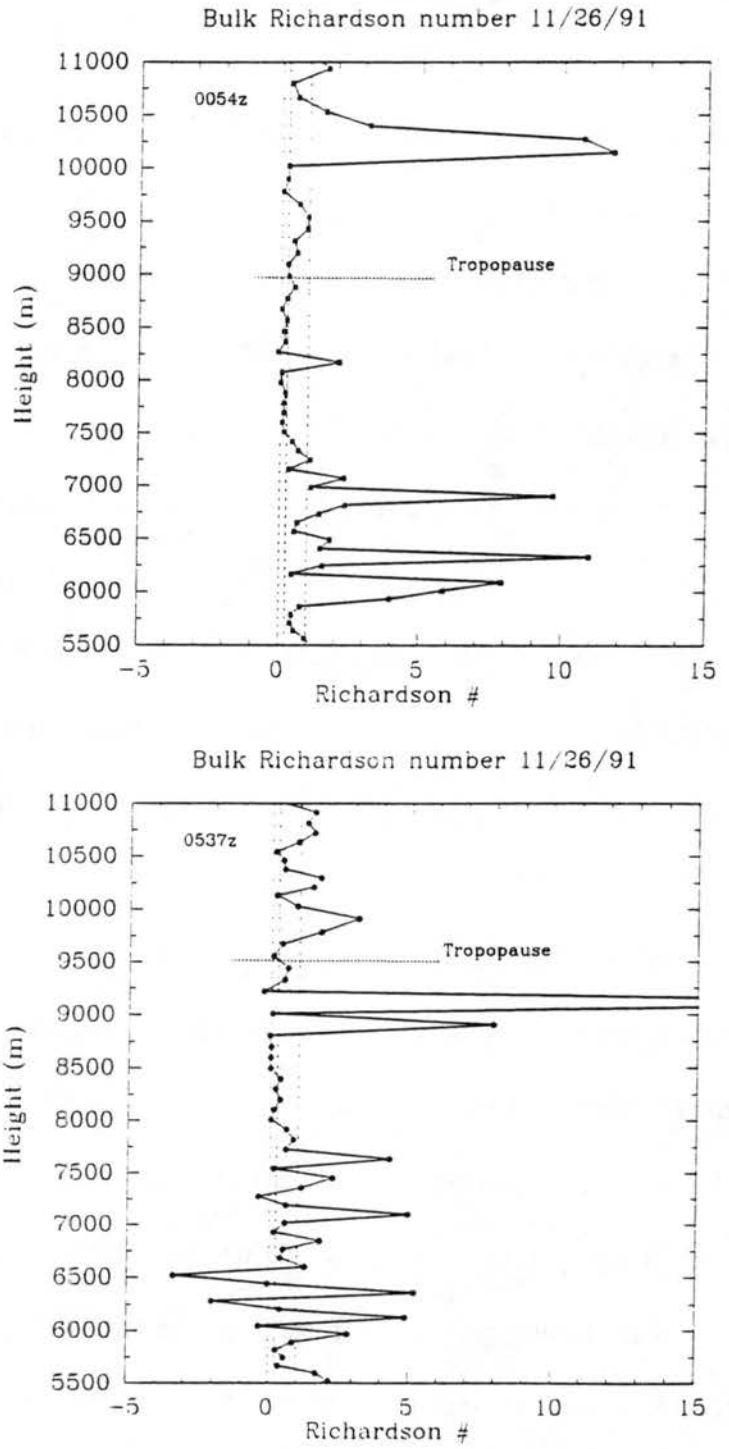

Figure 5.9 Bulk Richardson number calculated from the sounding in Figure 5.4.

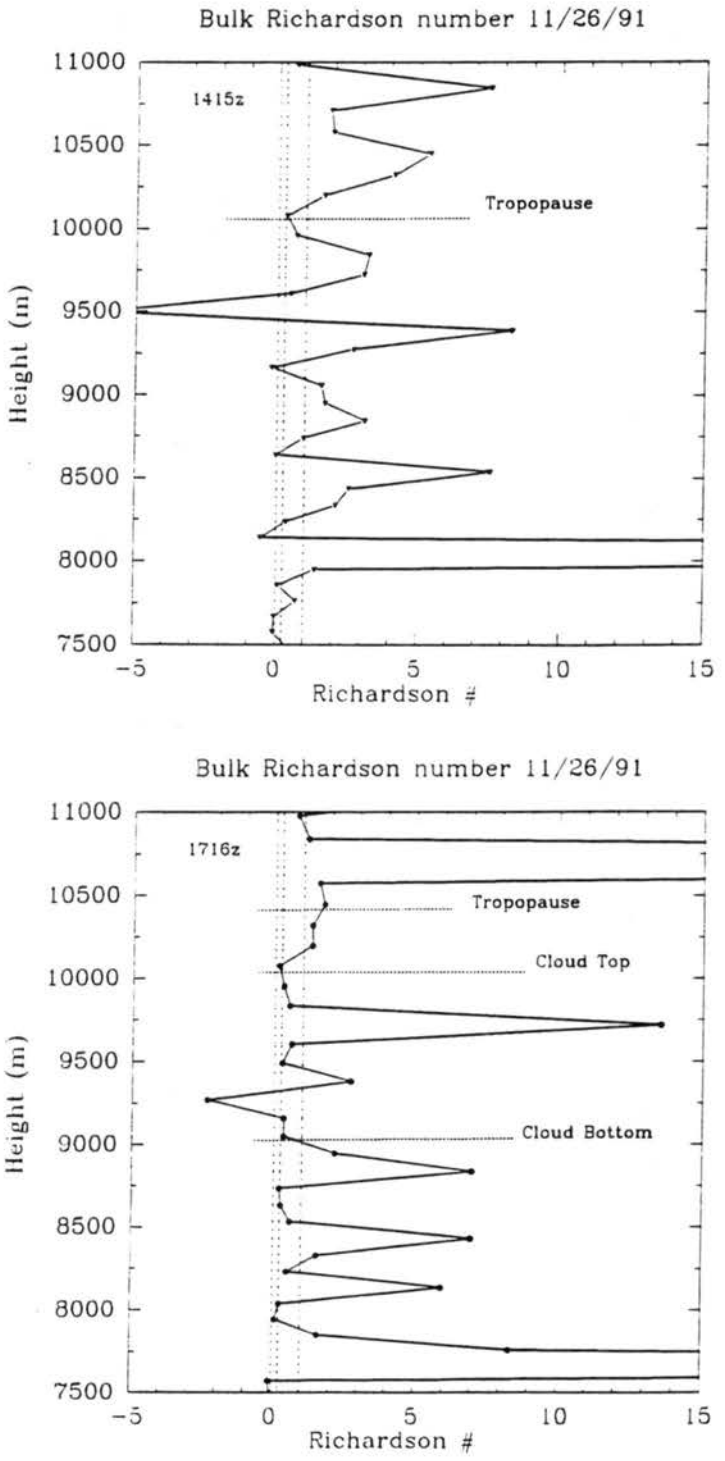

Figure 5.9 continued

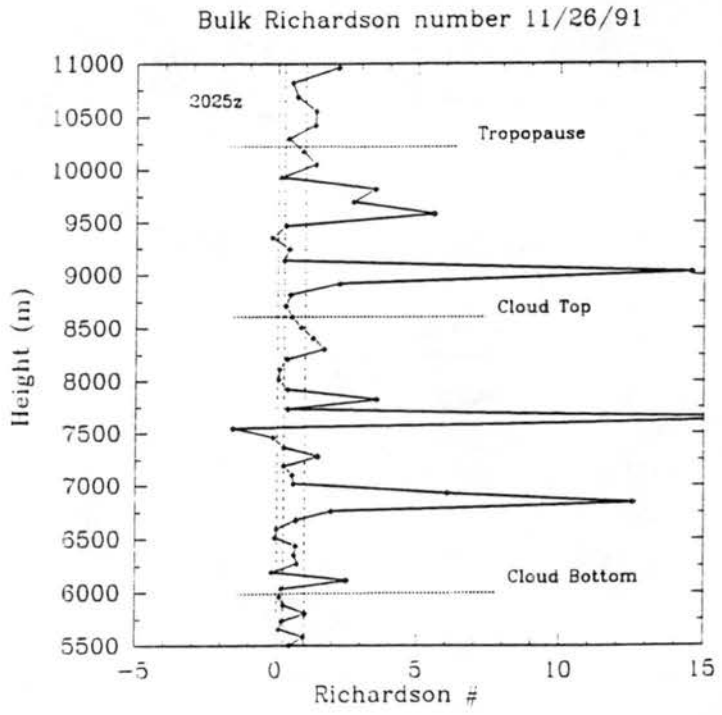

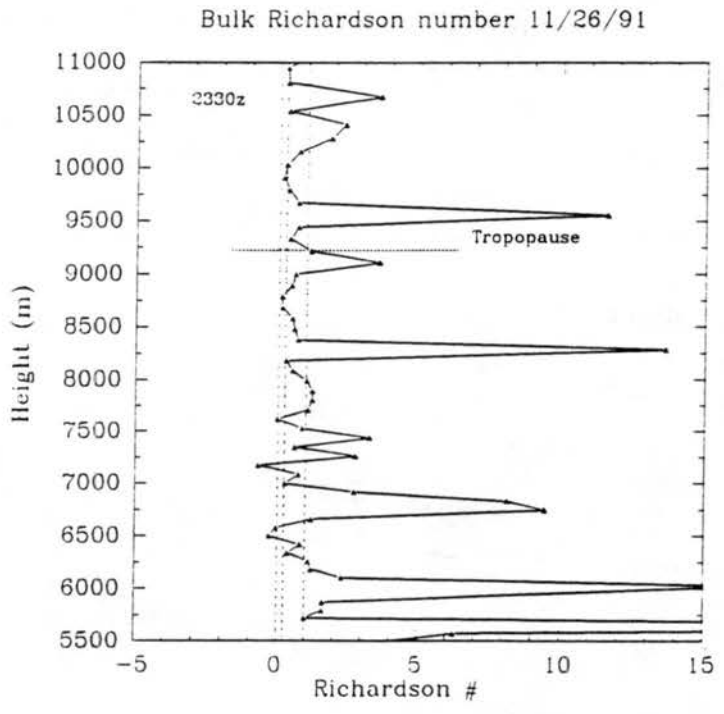

Figure 5.9 continued

5.9). Richardson number of the cloud top is generated from the sounding after the cloud was detected and has values less than 0.5 at 1716Z and 2025Z. The sounding associated with the middle cloud layer still reflects the small Ri at the cloud top and base. As time progressed, a deep layer with Ri values less than 1.0 appeared again in the evening (cf. 2330Z Ri profile). Even though small Richardson numbers are often found around the cloud layer, it is still difficult to interpret those layers as turbulent layers. The reason is that both small shear and vertical gradient of potential temperature (small buoyancy effect) exist, in particular at 1415Z and 1716Z. This can result in a small Richardson number, but under a very weak shear driven force. There is also a deep layer with small Richardson number located around the cloud top at 1716Z and 2025Z. The potential temperature and Richardson number profiles for these two soundings are quite similar. The difference of cloud structure, however, is clearly evident with the growing feature at 1716Z and an irregular cloud top after 2015Z. So it may be that no strong shearing features are involved in the cloud development. If the shear-driven turbulence does modify the cloud structure, its effect may be positive or negative on the cloud's growth/dissipation; it is not possible to make a definitive statement based upon the observation considered here.

Generally, the fine thermal stability structure related to cirrus uncinus (Yagi, 1969) is barely evident from our sounding data taken every three hours. In the 1716Z sounding, there is indeed a very thin layer with a nearly dry lapse rate at 10km level where a thin cirrus cloud was observed by the Parson's lidar. The next sounding at 2025Z does not reveal this fine structure for either the high or middle clouds.

However, for a longer period, the static stability structure shows a deep (about 3.5km) and nearly neutral, well-mixed cloud and subcloud layer with a thermally very stable layer above and an at-least slightly more stable layer below. This pattern is similar to the static stability structure of so-called cirrus fiblatus and cirrus spissatus clouds reported by Yagi (1969). It may be also concluded that the layers of and below the cirrus clouds have smaller vertical shear of horizontal wind and are characterized by a nearly well-mixed feature. The resulting Richardson number profiles suggest the existence of several dynamically turbulent regions in the cloud layers, which is also reported by Quante and Brown (1993) in their study of jet stream cirrus clouds turbulence using aircraft measurements. Commonly, at and near both the cloud top and the cloud base, there is the significant probability of KHI, which would favor entrainment/detrainments processes. However, in the cases that both shear and buoyancy effects are weak, shear forcing may be weaker than the forcing by large-scale vertical motion even if the Ri values were small enough for the onset of dynamical turbulence. Advection instead of vertical convection appear to be the source of moisture necessary for the developing cirrus cloud system in this case.

5.4 Wind Profiler Signal Power

As discussed in the chapter 2, the wind profiler echo mechanism has drawn significant attention by radar meteorologists. The theoretical and experimental studies using this new technology are important for understanding the real atmosphere. In this section, we will concentrate on analysis of the radar echo distributions and their relationship to meteorological conditions by examining the

time-height plots of the wind profiler signal power. Since there were no absolute signal power calibrations for the profilers used, the signal power discussed here is only in the terms of relative values.

The time series of the signal power of the NOAA wind profiler at NDS and HBR are shown in Figure 3.2. The time resolution used in this figure is six minutes, and the shaded areas of the figures represent a signal power equal to or greater than 50dB. Transversely (in temporal space), two distinct periods of strong echoes are observed from all beam directions at these stations. The first set of strong echoes are located in the upper troposphere and lasted for several hours after 0001Z. After this period, the signal strength in the upper troposphere began to decrease and a minimum was evident. The second set of strong echoes was received from the upper troposphere in the local morning, and from both upper troposphere and lower stratosphere in the evening of November 26. At NDS, there was a layer with extreme maximum radar reflectivity just above the tropopause. However, at HBR this phenomena was not obvious and only a very weak maximum of radar reflectivity was apparent at an altitude of 10.33km earlier in the day and at 10.5km sometime later.

The first set of maximum signal returns could be generated by strong shear-driven turbulence. As shown in the last section, a strong dynamically unstable layer caused by extremely strong wind shear was present in the upper troposphere between 0054Z and 0537Z. No cloud was reported during this period by the FIRE II daily mission records. Therefore strong Bragg scattering produced by the clear air

turbulence would dominate the radar signal echoes and be responsible for the maximum signal returns.

The atmospheric features related to the second set of strong echoes are more complicated. As was already shown earlier in this chapter, a jet streak was approaching Kansas in the morning. From the upper air sounding, the propagation speed of the jet streak is estimated to be on the order of 25 knots. Since HBR is roughly 165km upstream of NDS, the jet streak should arrive at HBR about three and half hours before it reached NDS. This time period is close to the time difference between the onset of the second set of strong echoes at HBR and NDS (shown in Figure 3.2). It suggests that there is a strong correlation between the jet streak and the radar reflectivity structures. The enhancement of radar echoes might be explained by large clear air turbulence in a jet streak area; it also might be caused by Fresnel scatters which are corresponding to multiple layers with large temperature gradients in the late of the day. There is also the possibility of cloud effects on this second set of strong radar echoes since cirrus clouds developed after 1600Z. However, a correlation study between the cloud vertical structure and the radar echoes indicate that the profiles were relatively insensitive to high and middle cloud particles; therefore Rayleigh backscattering from ice particles will be therefore neglected in this case. Yet studies on the vertical beam radial velocities in section 5.6 do a correlation between clouds and wind fields, which must be explained by causes other than Rayleigh scatter. The contribution to the radar signal of daytime heat convection is generally considered as a minor factor.

According to radar reflectivity theory, a large temperature gradient, such as those found at the tropopause, can cause a strong radar reflectivity gradient. Strong reflected echoes might be expected from the tropopause, however, in our case, there was a maximum of echo strength evident slightly above the tropopause (Figure 3.2). This is similar to the cases studied by Gage and Green(1978; 1979), where they investigated VHF radar echoes backscattered from the stratosphere and found maxima of signal returns in the stable lower stratosphere. A concept of aspect-sensitive (i.e., signal of the vertical beam is stronger than that of the oblique beams) Fresnel reflection was applied to explain this enhanced echo structure in the hydrostatically stable regions and to locate the tropopause. According to Larsen et al. (1991), the larger the ratio between signal power received by the vertical beam and the oblique beams, the stronger the aspect-sensitivity. But the ratio values in Figure 5.10 are mainly around the value of 0dB which indicates that the oblique beams received as much signal as the vertical beam. It is then concluded that the aspect-sensitive characteristic was not strong in our case, or the signal values of the vertical beam is not accurate enough to reveal this aspect-sensitive structure due to the clutter uncertainty.

The layer of minimum radar signals in the upper troposphere during the period of 0500Z to 1600Z at NDS and 0700Z to 1300Z at HBR (Figure 3.2) is considered as a reflectively quiet area, which possibly means small spacial changes of the atmospheric thermodynamic properties and weak clear air turbulence. There was no cloud reported during that period.

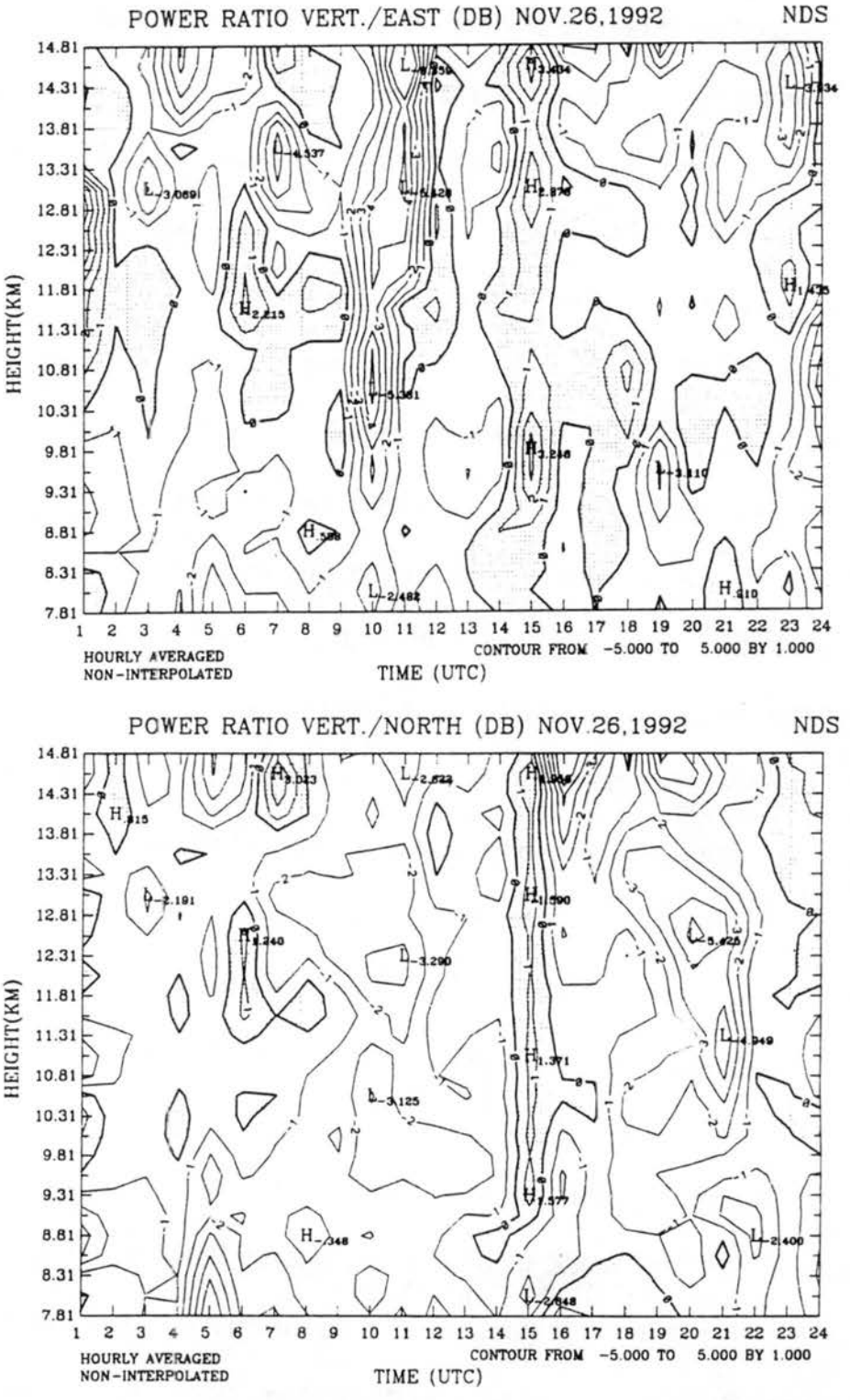

Figure 5.10 The time-height contours of the signal power ratio between the vertical beam and the oblique beams from wind profilers at a)NDS and b) HBR on November 26, 1991. Unit is dB and the shaded area represents positive ratio.

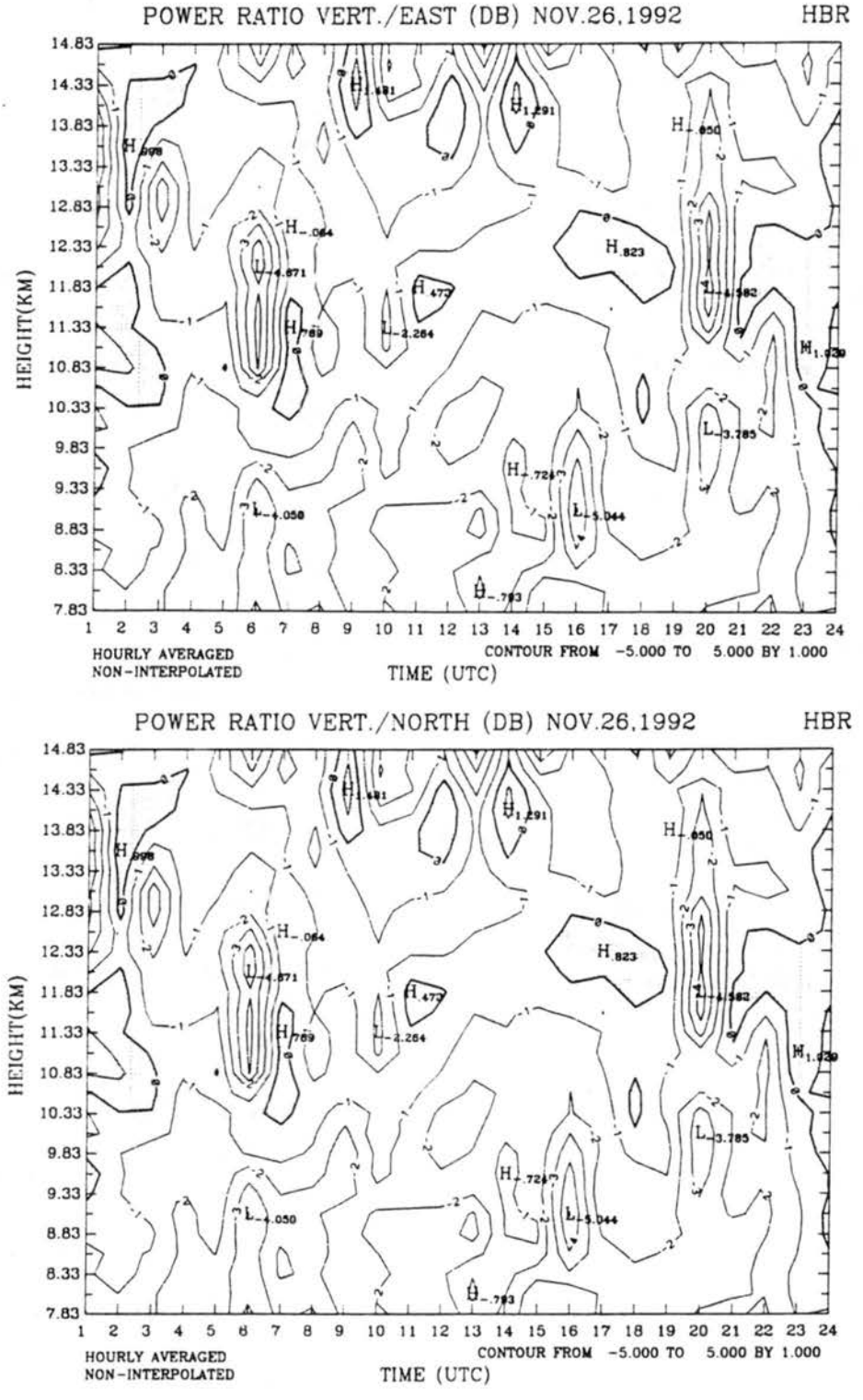

Figure 5.10 continued.

5.5 Horizontal Thermal Advection and the Ageostrophic Wind Field

As suggested by the previous theoretical studies, the effects of shearing deformation and curvature and geostrophic stretching deformation (confluence/diffluence) must be considered in explaining the jet streak dynamical process. Figure 5.11 shows temperature, geostrophic wind and potential height contours on isobaric surfaces deduced from NWS sounding data at 1200Z and 1800Z on November 26th, 1991. It is evident that, at 1200Z, no obvious thermal gradient existed along the jet on the 400mb isobaric surface, but there was weak warm advection downstream of the jet streak exit region over Kansas, Oklahoma, Texas and southeast of New Mexico. At 250mb, a cold center was present over Iowa with the presence of a warm advection in the left-exit area of the jet streak over Colorado. At 1800Z, weak warm advection still existed in the left-exit area of the 400mb surface. The warm advection on the 250mb surface was largely increasing in strength. By 1800Z the entire jet streak exit area at 250mb surface was generally covered by warm advections with the maximum advection locating on the left side. And the front of this jet streak system was entering the trough region of the synoptic wave.

In the terms of shearing deformation, the meridional gradient of the zonal geostrophic wind is negative on the left side of the jet so that, combined with the warm advection, it yields a positive shearing deformation effect which supports a direct circulation in the left-exit area of the jet streak. This direct circulation will be superimposed on the indirect circulation produced by the geostrophic stretching

deformation. Figure 5.11 shows that the along-jet thermal gradient was very weak in the right-exit area; this indicates that the downward motion produced by the geostrophic stretching deformation was not as significantly modified by the effect of shearing deformation as that in the left-exit area. As a result the cross-jet circulation in the exit area becomes asymmetric to the jet axis with a shift of the maximum upward and downward centers, eg. the maximum of upward motion on the left side moves toward the jet core. In this case, it is possible for the shearing deformation to be large enough to even cause a downward motion on the left side of the jet streak, with a maximum upward motion beneath the jet streak core.

The wind field observations on the 250mb surface indicate the nearly linear orientation of this jet streak system, which suggests the applicability of the two-dimensional model which excludes the along-front ageostrophic component. While this may be appropriate for the 1200Z situation, it may not be valid when the exit area of the jet streak was entering the trough region at 1800Z. The three-dimensional features caused by curvature effects described by Shapiro and Kennedy (1981) would have to be addressed.

Figure 5.12 shows that at 1200Z, the ageostrophic winds were northeasterly between the 150mb and 500mb with a maximum around 300mb. This nearly normal-to-jet direction illustrates the domination of the transverse ageostrophic circulation as expected by the classical conceptual model. On the 600mb and 700mb charts, meridional components of the ageostrophic wind disappeared and the ageostrophic winds became either easterly or westerly with an enhanced meridional gradient. This

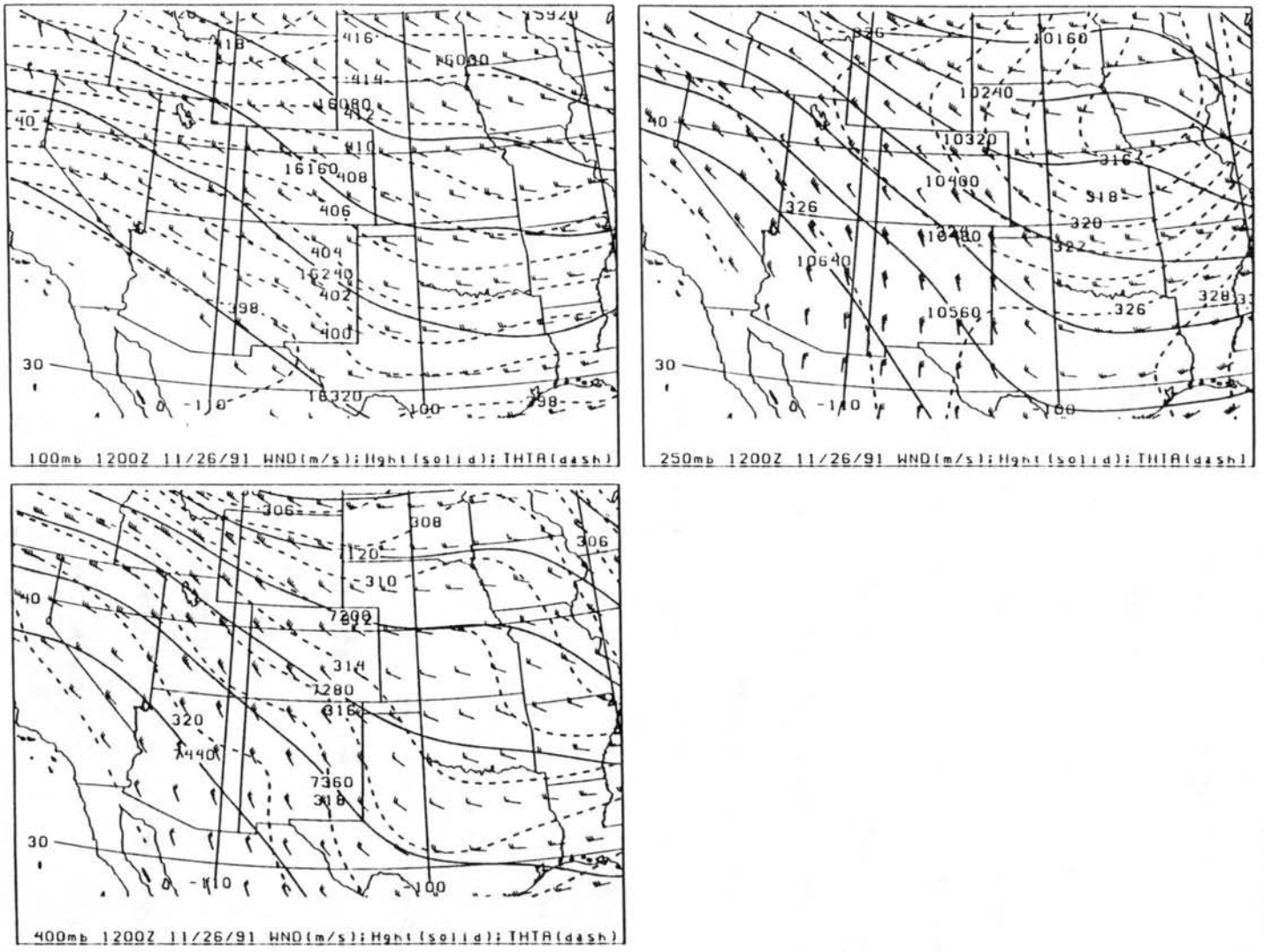

Figure 5.11 Contours of potential temperature (dashed), potential height (solid) and geostrophic winds represented by wind bars m/s, November 26th.

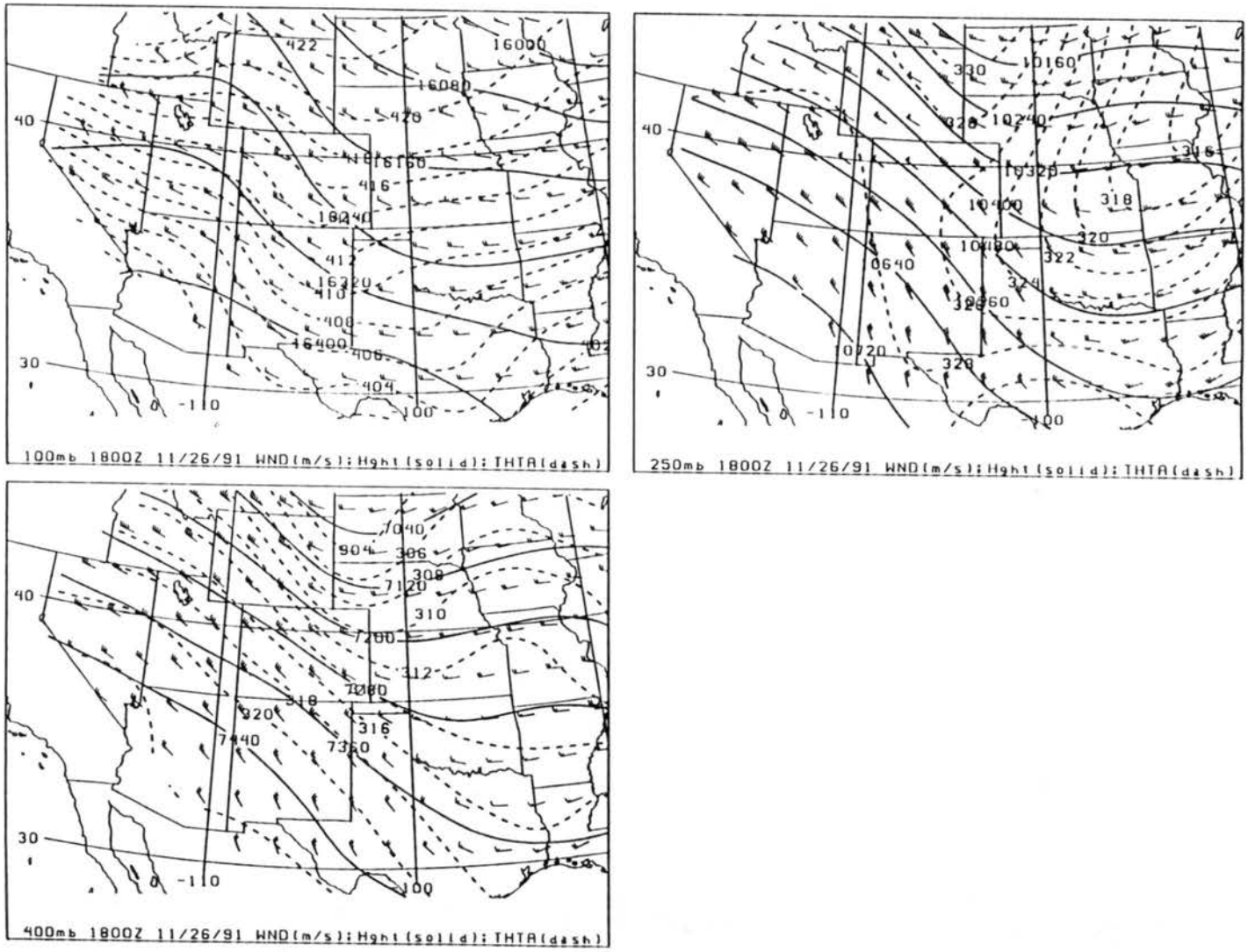

Figure 5.11 continued.

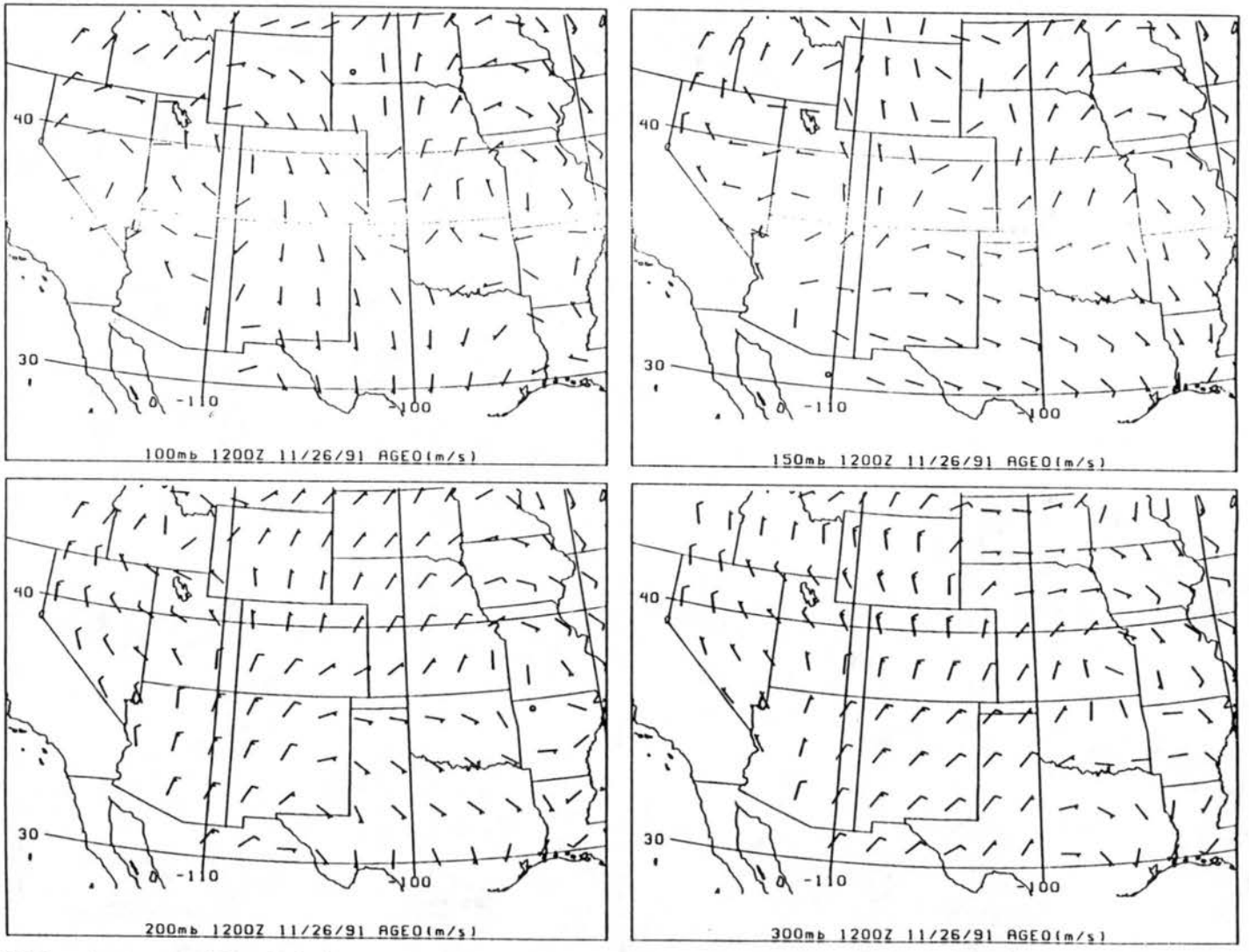

Figure 5.12 Ageostrophic winds from rawinsonde systems for 1200Z and 1800Z on November 26th. One full wind bar represents 10m/s.

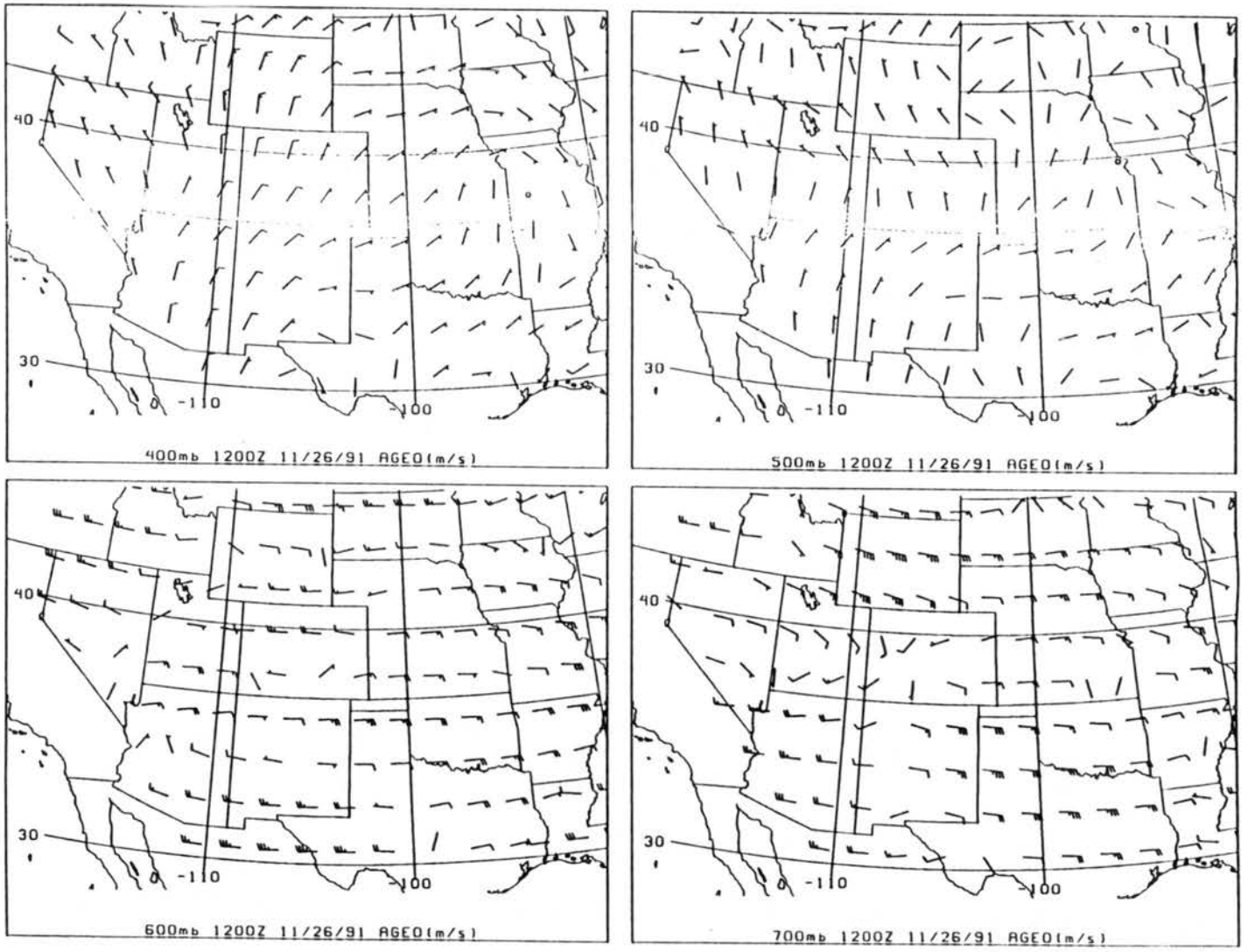

Figure 5.12 continued.

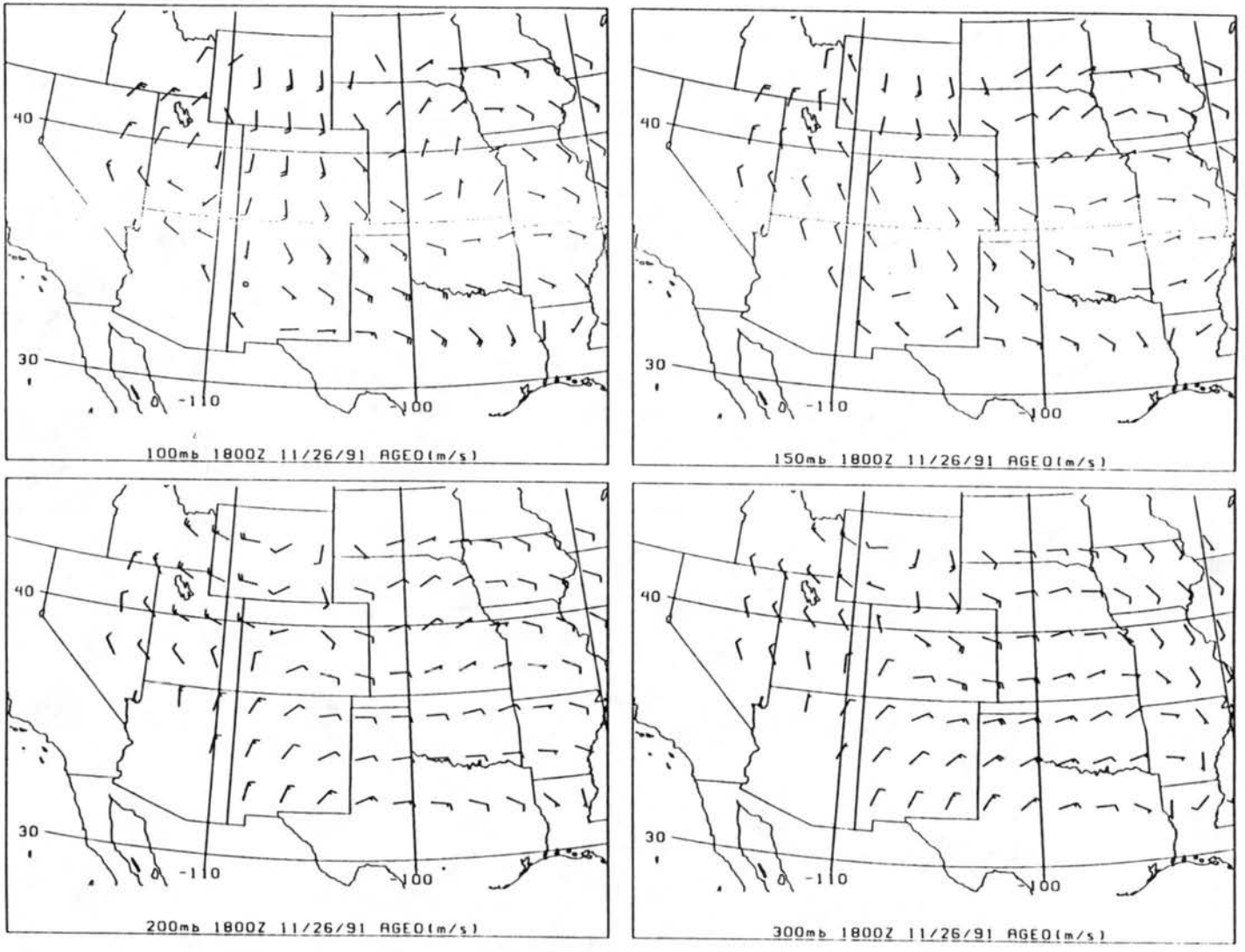

Figure 5.12 continued.

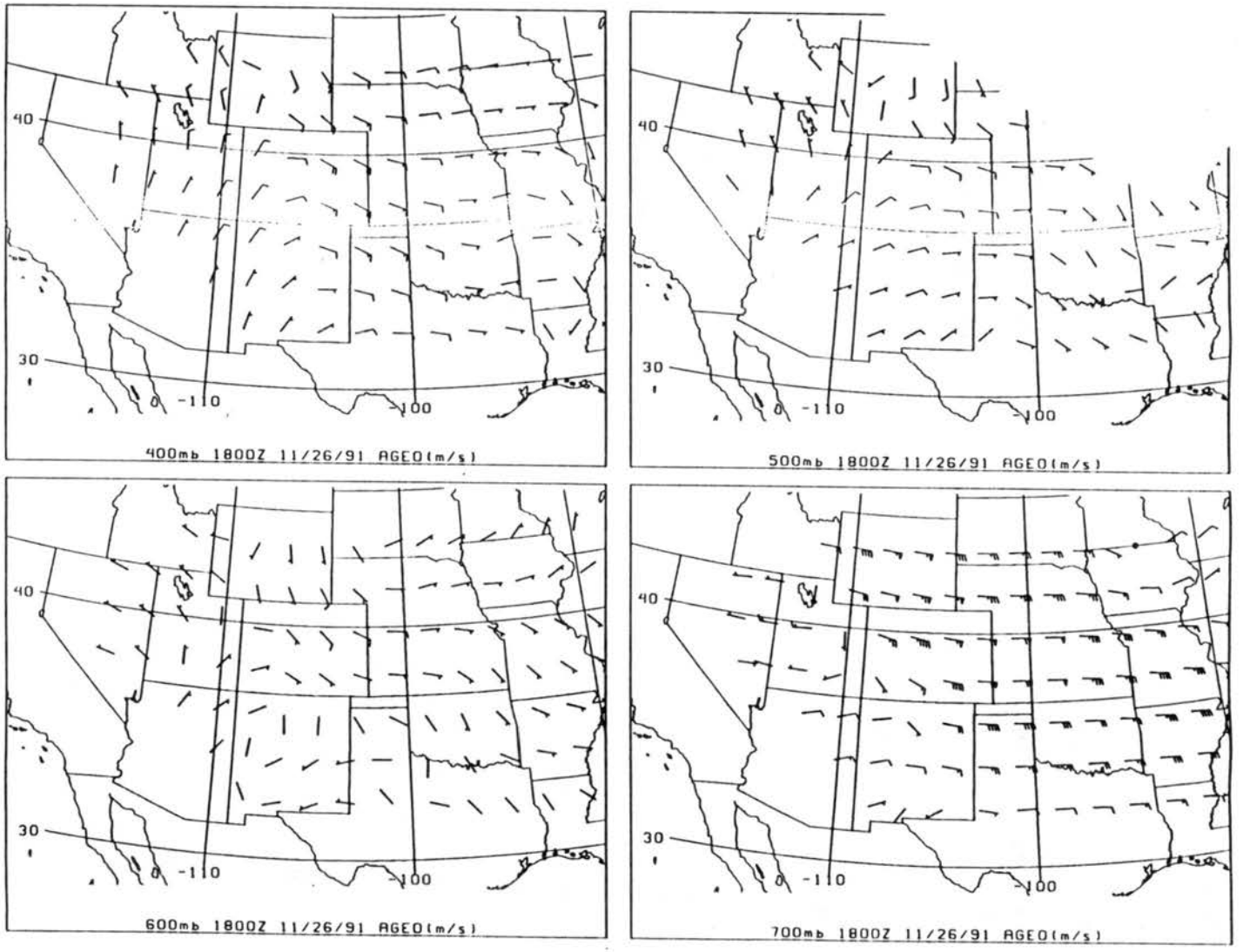

Figure 5.12 continued.

indicates that the anticipated northwesterly ageostrophic component in the lower levels is to be revealed since many factors can significantly modify ageostrophic wind in the low troposphere. The ageostrophic winds turned southerly at 100mb. In the jet streak left exit area over Texas, Oklahoma and Kansas, there is a confluence region at layers above 200mb and difluence on the 300mb surface. Conservation principles suggest that this may produce a downward motion above the jet core and an upward motion below the jet core.

By 1800Z, the ageostrophic wind speeds were generally enhanced. Wind direction became more southeasterly above 150mb. Northeasterly ageostrophic winds between the lower stratosphere and 500mb generally disappeared and changed to an easterly wind in the exit area over Texas, Oklahoma, and Kansas. This deviation from the classical model of a jet streak may be explained by the curvature effect when the jet streak was close to the trough. In addition, the direct circulation induced by the strengthened shearing deformation present at 1800Z also modified the ageostrophic wind field. The transverse ageostrophic circulation expected from geostrophic difluence in the conventional 2-dimensional model can be barely detected. In the next section, we will further analyze the vertical motion fields.

5.6 Divergence Structure and Vertical Wind Field

In the present case, the classical pattern of the air mass divergence and ageostrophic circulation of the jet streak exit region is modified by both the shearing deformation and curvature effects.

Figure 5.13 shows the time-height contours of the divergence pattern derived from three NOAA wind profilers at NDS, HBR, and LMN based on the kinematic method using hourly-averaged horizontal velocities. The shaded areas indicate divergence; the unshaded area represent convergence. The beginning of the time series, convergent air motions dominated the lower stratosphere and upper troposphere, while divergent motions were presented in the lower portion of the atmosphere, however by 047 divergence was found throughout most of the troposphere (from 2Km to 9Km). This divergence pattern in the troposphere lasted until about 1100Z when convergence near 3.5km appeared and began to expand downward toward the surface and upward into the middle of the troposphere. This was followed by a rapid penetration of convergent motion into the upper troposphere at 1900Z. The values of the divergence/convergence mainly ranged between $4x10^{-5}$ s^{-1} and $-2x10^{-5}$ s^{-1}.

Assuming zero vertical velocity at the altitudes of 1km and 16.4km, vertical velocities can be calculated by integrating the divergence profile. The time-height contouring of the derived vertical wind velocities are shown in Figure 5.14, where the shaded areas present upward motions and the thick solid lines are the zero velocity isopleths. The velocities have a range of -14cm/s to 12cm/s. Prior to 1330Z, the atmosphere was dominated by downward air motions. A region of upward motion quickly developed below 9.5km after 1330Z. The vertical expansion of this upward motion at 10km stopped between 1700Z to 2000Z, when the jet front area was

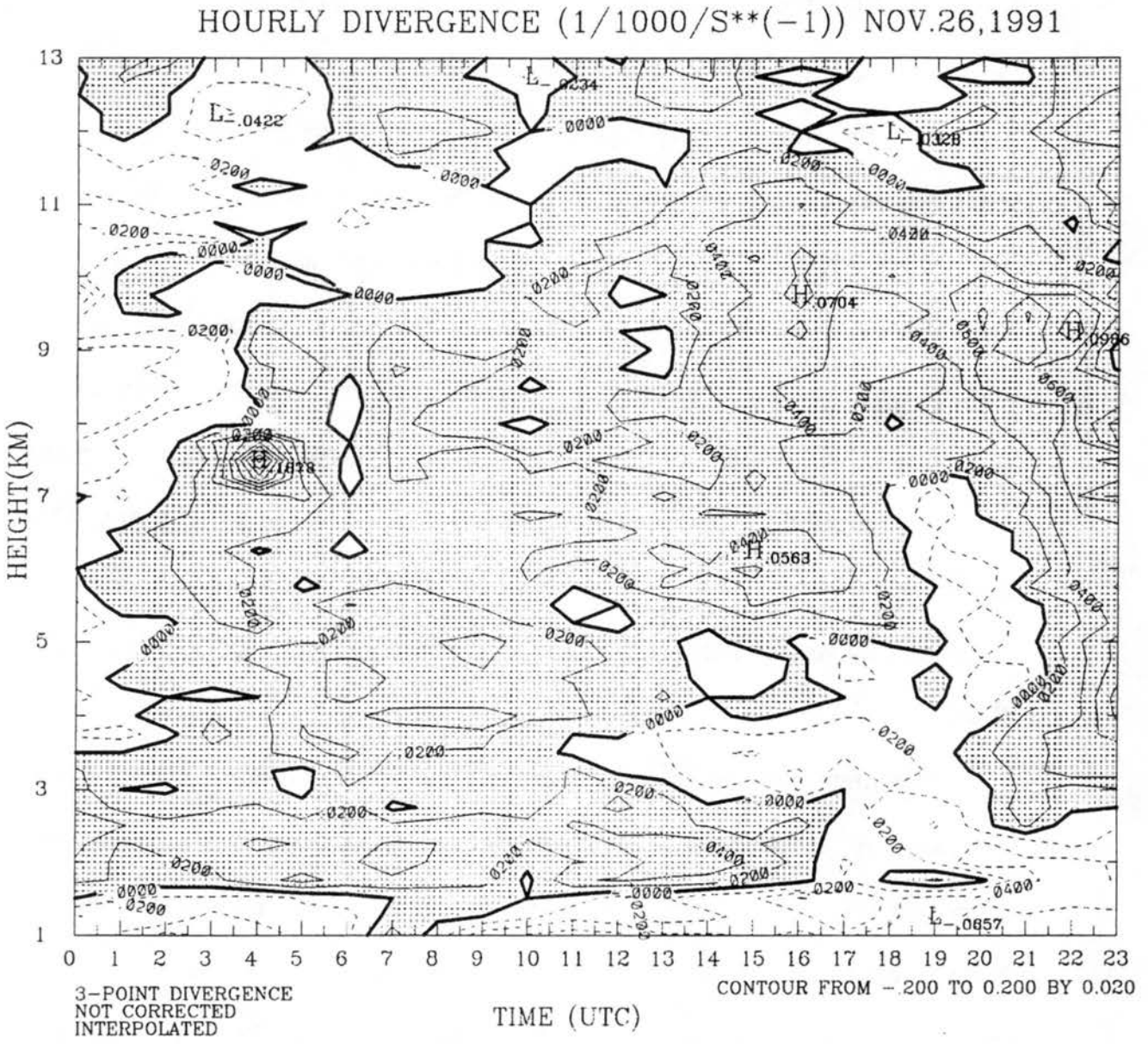

Figure 5.13 Time-height contours of hourly averaged divergence deduced from wind profilers hourly averaged horizontal winds using kinematic method. Positive ~ divergence, negative ~ convergence. Unit $s^{-1}/1000$. November 26th.

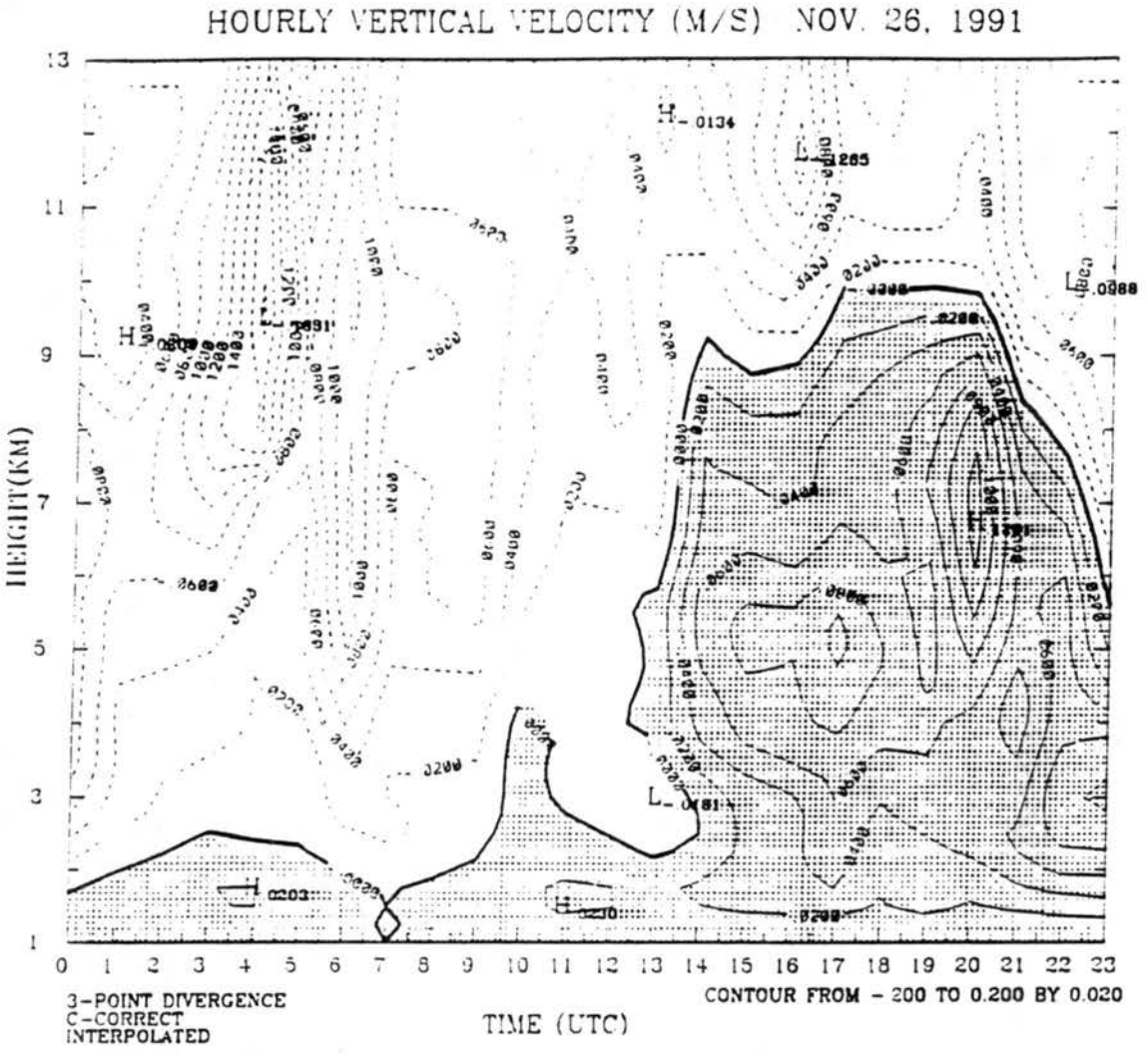

Figure 5.14 Hourly averaged vertical velocities from the kinematic method. Contour interval is 0.02m/s. Shaded areas indicate upward motions. Dark solid line is the zero line. (Repeat of Fig. 3.13)

passing through the observational site. The height of the reversal level of the vertical motion started to drop at 2000Z when the jet streak maximum passed over the observation area. This structure is consistent with the classical jet streak circulation model as discussed earlier.

The 12-hour averaged profiles in Figure 5.15 exhibit a downward motion through the entire atmosphere during the first 12 hours. The maximum value in the figure is about 9cm/s. During the second 12-hour period, a pair of ascending and descending air currents of almost equal magnitude dominate the troposphere and lower stratosphere, respectively. The large downward motion in the lower stratosphere further confirms the hypothesis that the vertical circulation above a jet streak has direction opposite to the one in the troposphere (Namias and Clapp (1949); Uccellini and Johnson (1979); Mattocks and Bleck (1986)).

Figure 3.10 presented time-height contours of hourly averaged vertical velocities derived from CSU wind profiler data using the quasi-VAD technique. Since the upper level data above 13km were often poorly defined, an upper boundary is placed at 12.5km by assuming zero vertical velocity. The contours in Figure 3.10 show significantly more variable structures than that found in Figure 5.14. However, applying the quasi VAD method to 12-hour averaged profiles (Figure 5.16), a consistent upward motion extending from the middle to the upper troposphere is found during the 12-24Z period when the jet streak was passing by the observation area. The sign of vertical velocities changed at about 10km accompanied by a much weaker downward motion above the jet streak core. The strong ascending motion

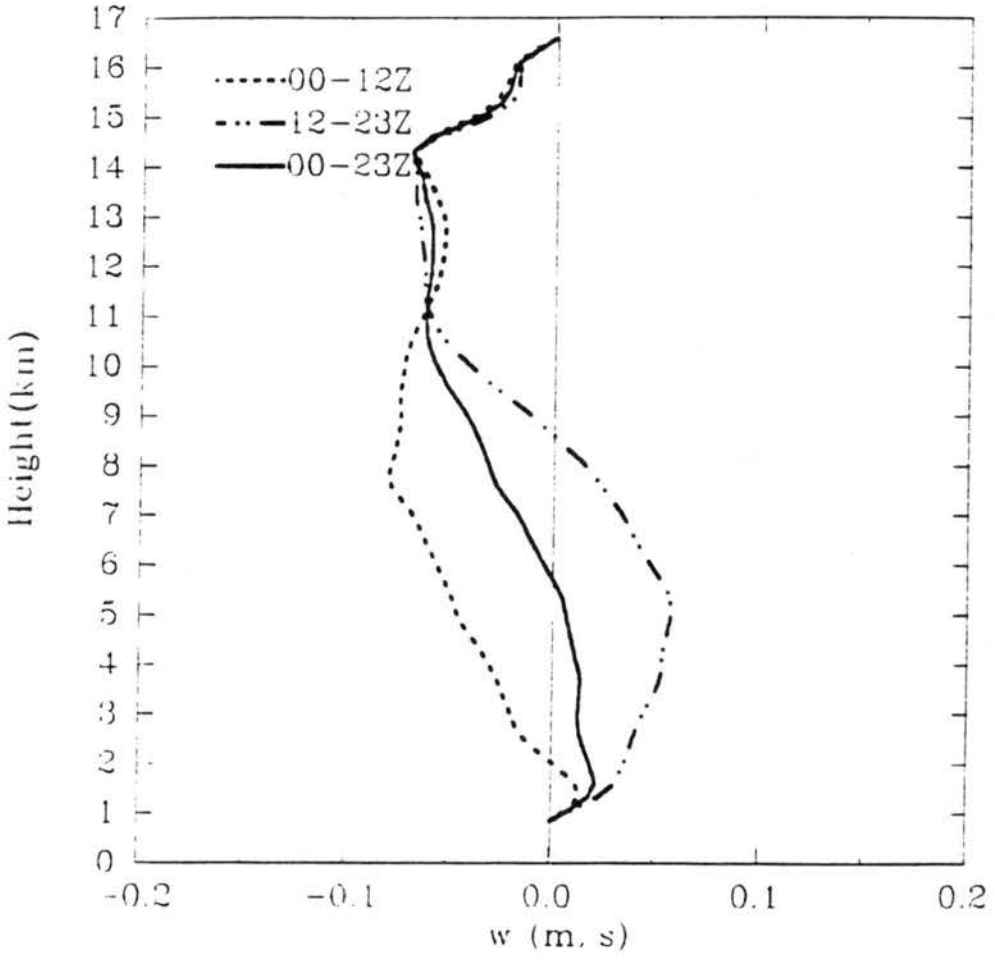

Figure 5.15 Averaged vertical velocity profiles deduced from kinematic method. Dashed line: 00-12Z averaged; dash-dotted line: 12-23Z averaged; solid line: daily averaged. (Repeat of Fig. 3.14).

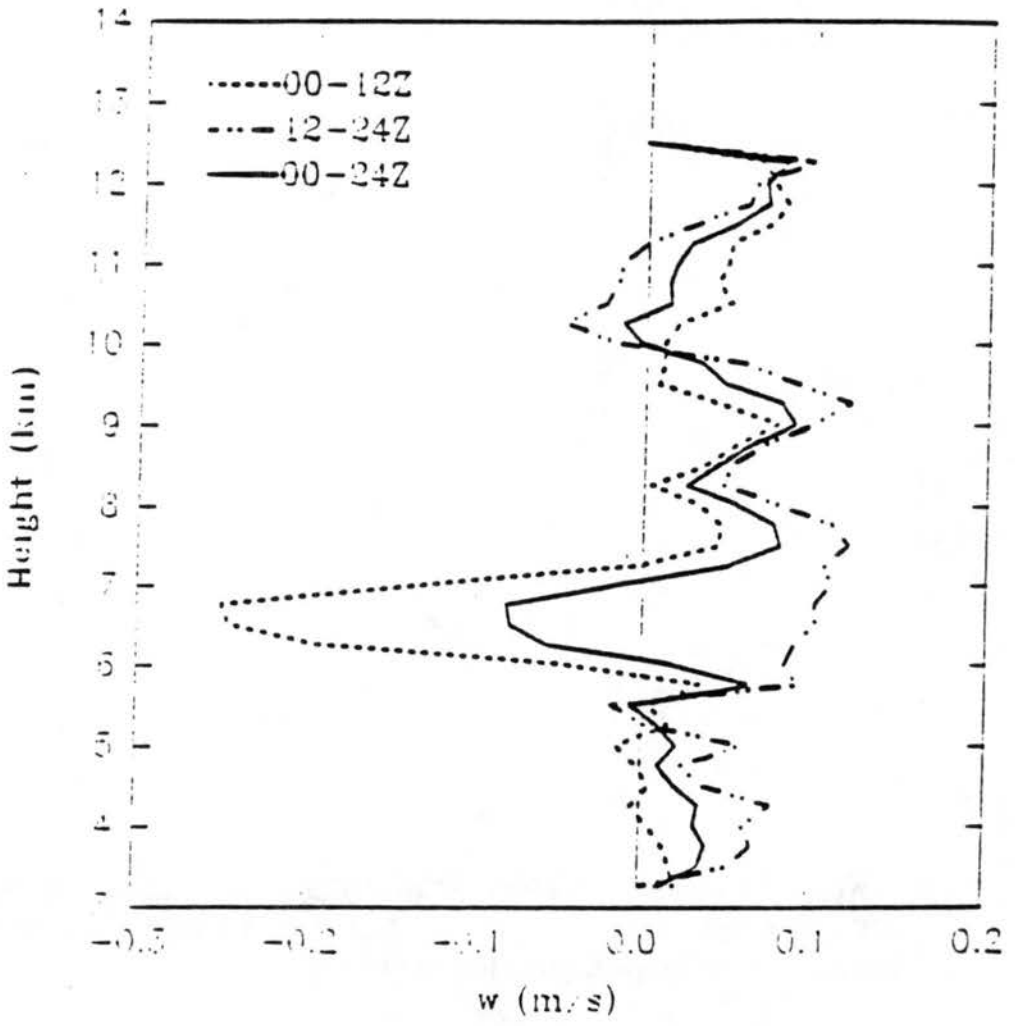

Figure 5.16 Averaged vertical velocity from the quasi-VAD method. (Repeat of Fig. 3.11)

deduced from the kinematic method does not appears in this case. Since an upper boundary was defined at 12.5km with zero vertical velocity, extreme caution must be taken in interpreting the data between 11.5km and 12.5km. As a result, the negative vertical velocity above the jet system may not reveal the true vertical air motions since the layer is too close to the top boundary. The averaged vertical air motion for the period between 00Z and 12Z indicates an upward motion above 7km instead of downward motion suggested by Figure 5.15. The averaged vertical velocities generally ranged between -10cm/s and +10cm/s even though there is a -0.27 m/s maximum at about 6.6km in the 00-12Z averaged profile for the quasi-VAD method.

According to the earlier discussions, signal returns from small scale motions can affect the retrieved vertical air motions. Since both the satellite IR images and ground-based lidar images of the clouds were available during this experimental period, they can be used further to explore how clouds are related to wind profilers direct measurements of vertical air motions. Figure 5.17 shows a time-height contours of the vertical velocities directly measured by the wind profiler at NDS during the period of 12Z to 22Z. The figure shows the alternating upward and downward motions at short cycles. However, there was a consistent descending motion below 10km after 1730Z. The cirrus cloud was first reported by the lidar at about 1615Z at the Parsons site. One might attribute this downward motion to the ice particles in cirrus clouds, however there was a 1-hour difference between these two events. Further analysis of the vertical distribution of this downward moving mass indicates that this layer extended from 10km to about 5km at 1900Z, which is much

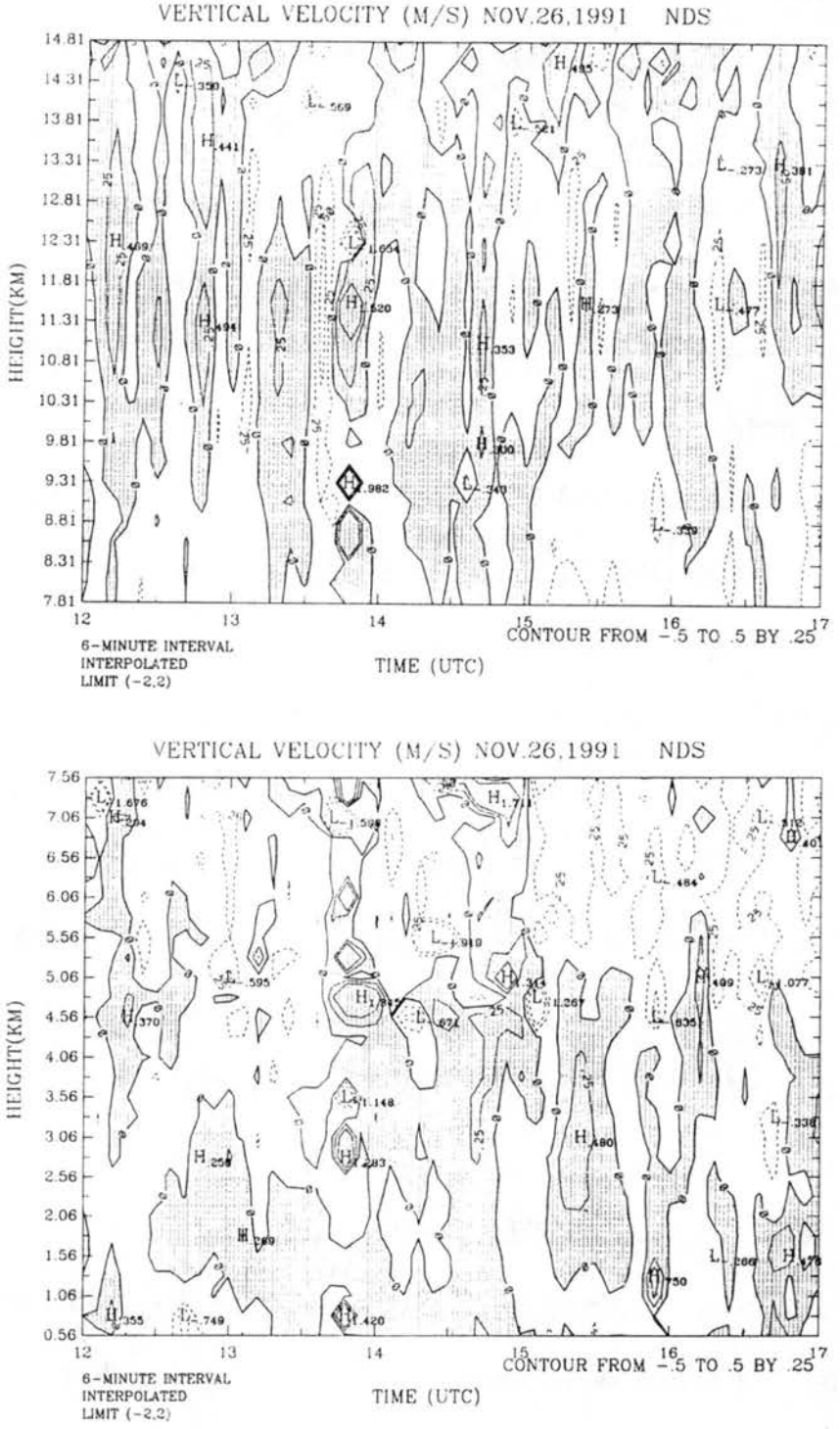

Figure 5.17 Time-height contours of the 6-minute vertical velocities at NDS. Positive values are downward motion and negative values are upward motions. Unit is m/s.

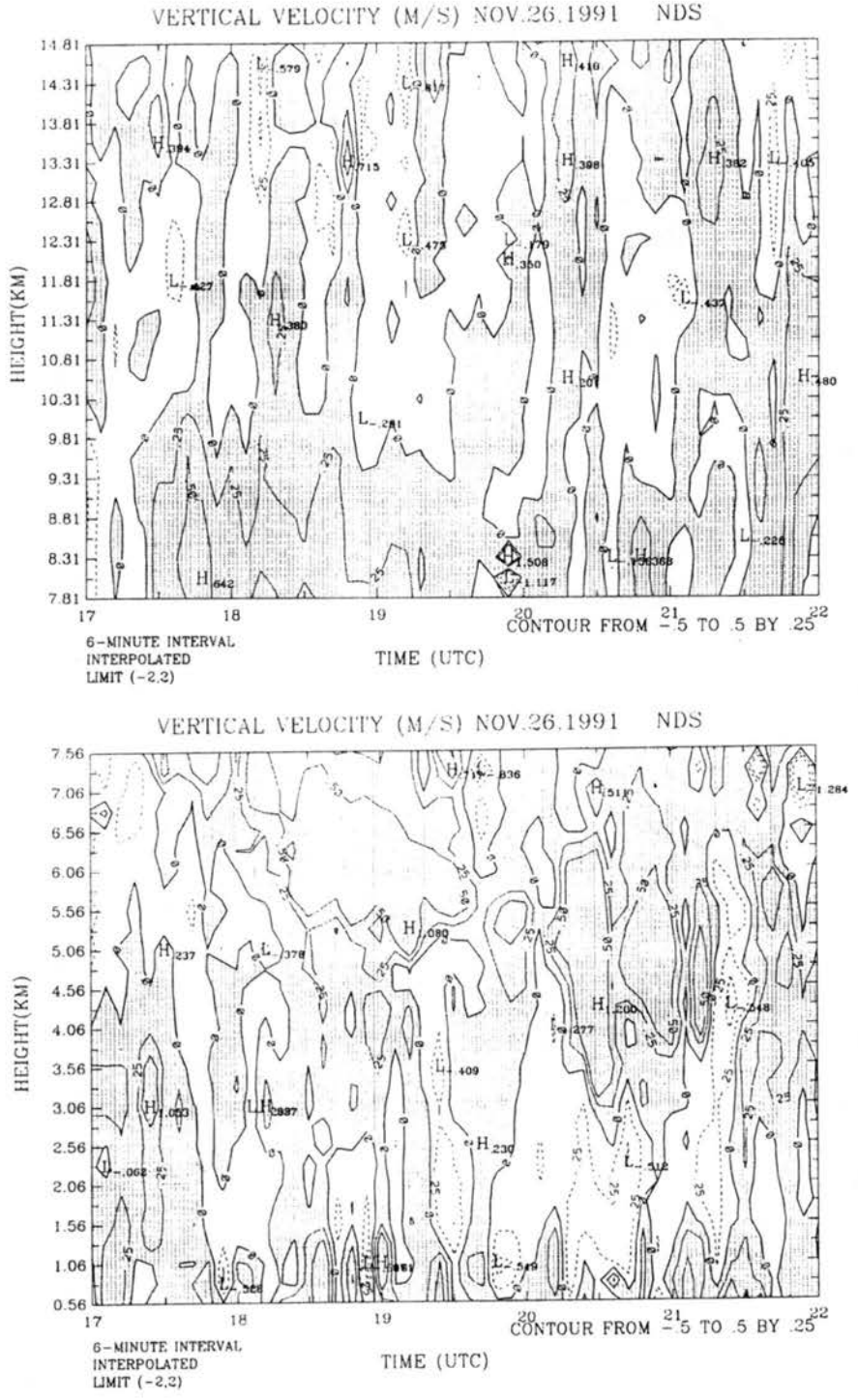

Figure 5.17 continued.

thicker than the cloud layer itself. Therefore, one might expect that the small scale air motions induced by the clouds (thermodynamical processes, shear-induced turbulence, cloud droplet motions etc.) instead of Rayleigh backscattering from cloud particles themselves were responsible for the above echoing features.

In order to directly retrieve large-scale air motions from the wind profiler, data were averaged at the NDS site between 1400Z and 1700Z when the jet streak front area (exit region) was moving over the observation site, and when the cirrus clouds had no influence on the wind profiler sampling. During this period there was extremely good agreement among the vertical velocities deduced from the averaged direct measurement (shown in Figure 5.18), the quasi-VAD retrieved profile and that deduced from the kinematic method. An upward motion field with a maximum of 17cm/s at 6km was well defined in the upper troposphere. The magnitude of this upward motion decreased dramatically between 8 and 10km with a quiescent layer between 10km and 11km, in the terms of vertical air motion.

To analyze the horizontal variations of the vertical motion fields during the jet streak event, isopleths of the 14-17Z averaged vertical velocity based on interpolated direct observational data from the NOAA wind profilers are shown in Figure 5.19. The rectangular area marked by the dashed line in Figure 1.1 is the region where interpolation was done using a grid resolution of 0.5°x0.5°. The stations in the box had missing vertical velocity data on 26th of November. Due to lack of data on the right exit side of the jet streak, the analysis can only be done in the left exit region located in the Kansas area. Figure 5.19 shows that small scale motions were mainly

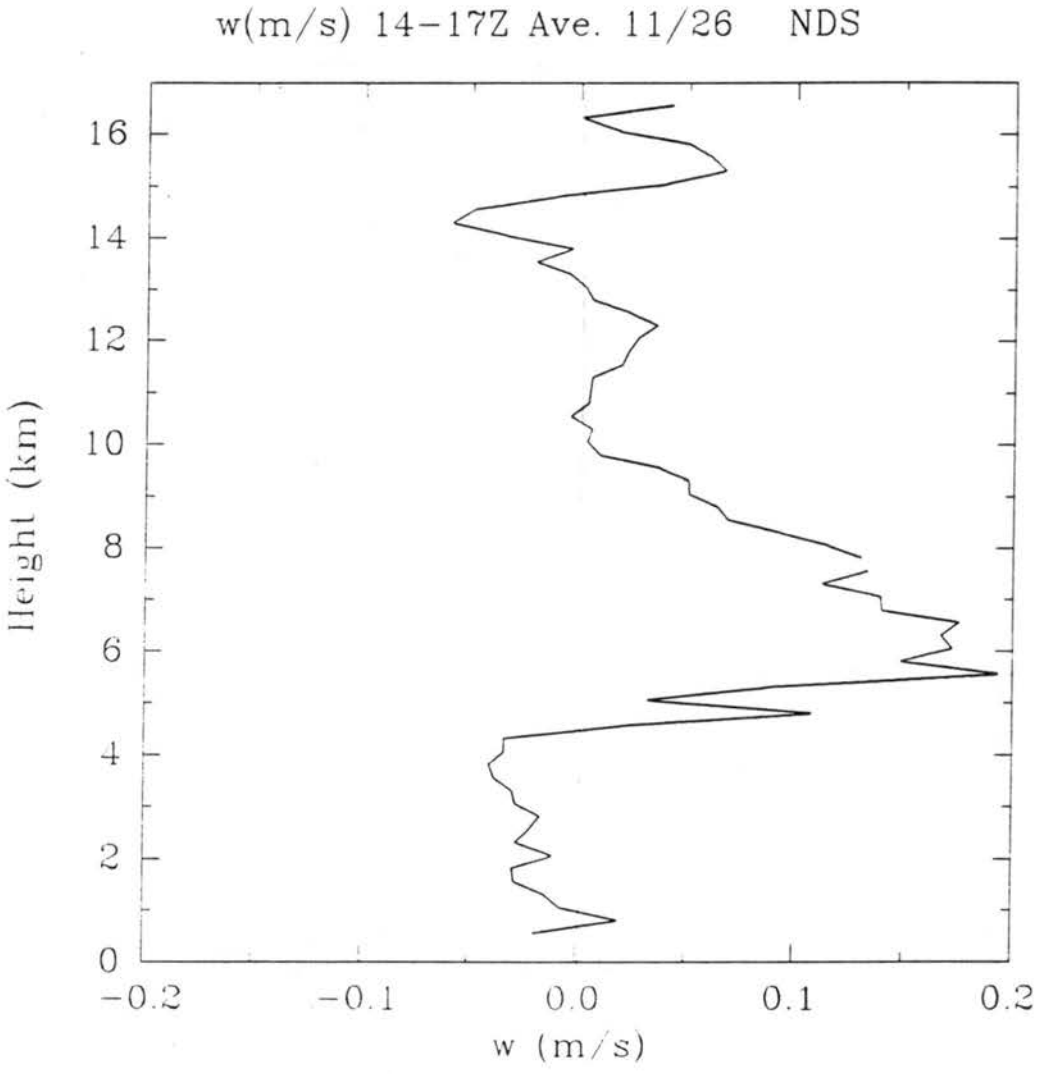

Figure 5.18 Three-hour averaged vertical wind profile from direct vertical beam measurement at NDS. Unit is m/s. On November 26.

a) 3km

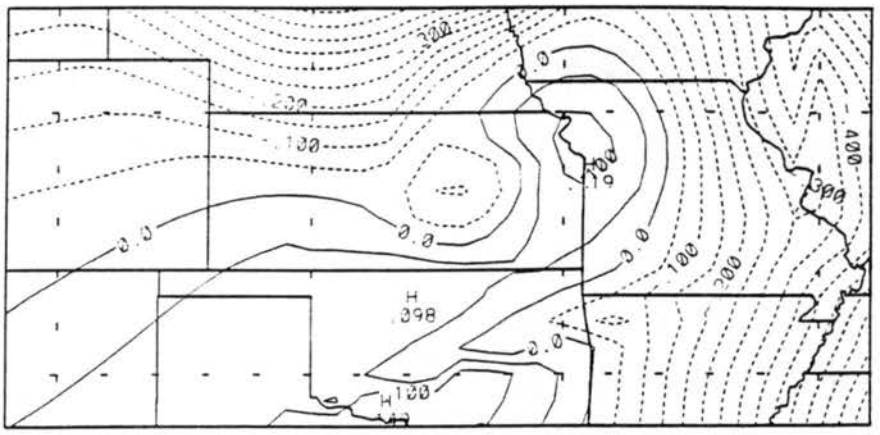

CONTOUR FROM .0 .F000 TO .0 .3000 CONTOUR INTERVAL OF .0.50000E-01 PT(3,3)= .0.40454E-01

b) 4km

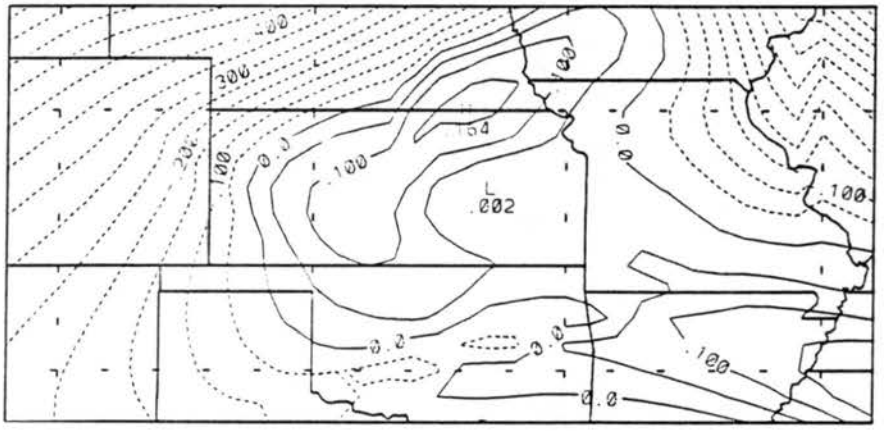

CONTOUR FROM -0.65000 TO 0.15000 CONTOUR INTERVAL OF 0.50000E-01 PT(3,3)= -0.20530

c) 5km

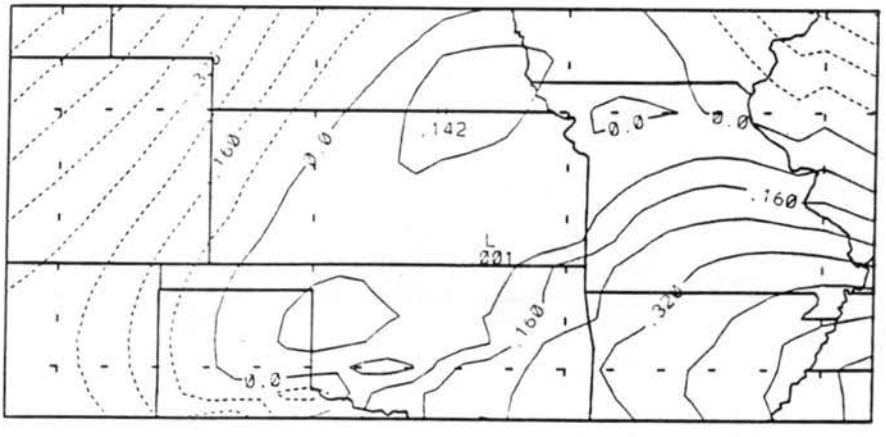

CONTOUR FROM -0.64000 TO 0.56000 CONTOUR INTERVAL OF 0.80000E-01 PT(3,3)= -0.26528

Figure 5.19 Three-hour (14Z-17Z) averaged vertical velocity (m/s) contours deduced from the direct vertical beam measurements by NOAA wind profiler network. The positive means ascending and the negative means descending.

d) 6km

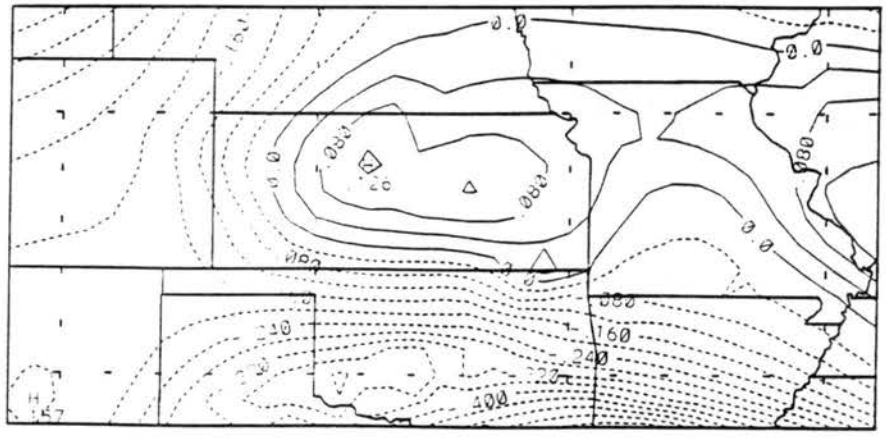

CONTOUR FROM -0.56000 TO 0.12000 CONTOUR INTERVAL OF 0.40000E-01 PT(3,3)= -0.16067

e) 7km

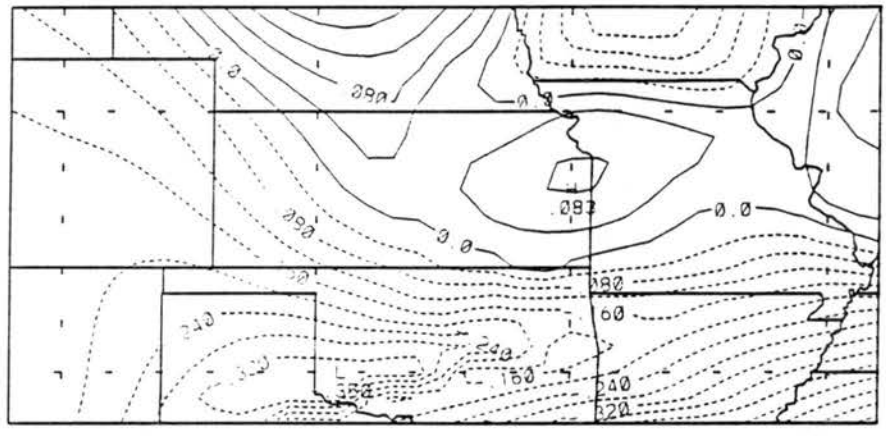

CONTOUR FROM -0.56000 TO 0.16000 CONTOUR INTERVAL OF 0.40000E-01 PT(3,3)= -0.18804

f) 8km

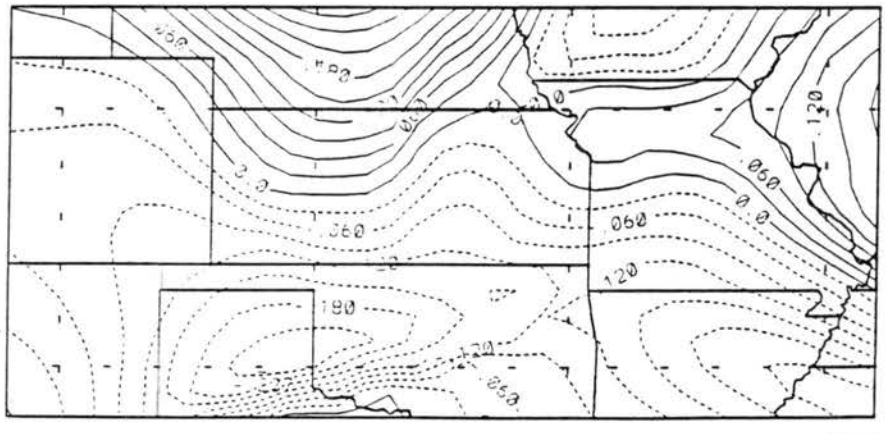

CONTOUR FROM -0.21000 TO 0.27000 CONTOUR INTERVAL OF 0.30000E-01 PT(3,3)= -0.37259E-01

Figure 5.19 continued.

g) 9km

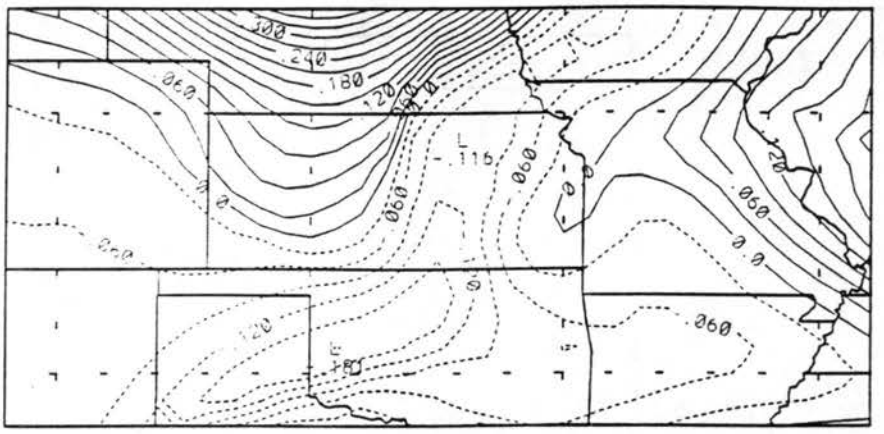

CONTOUR FROM -0.18000 TO 0.39000 CONTOUR INTERVAL OF 0.30000E-01 PT(3,3)= -0.67093E-01

h) 10km

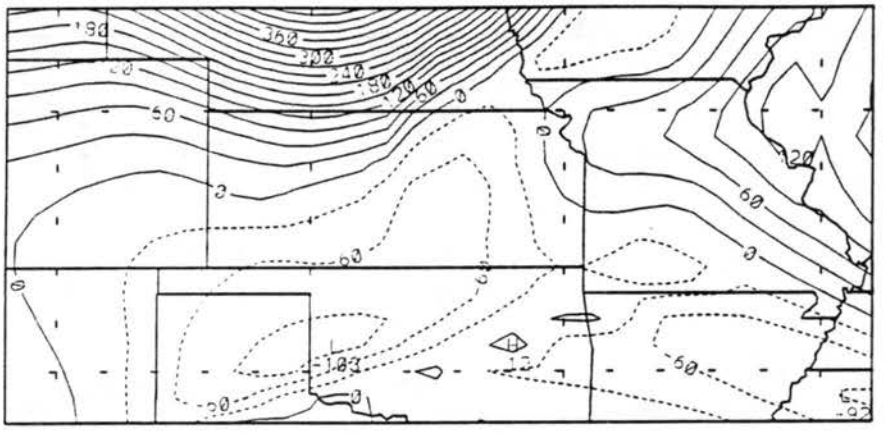

CONTOUR FROM -0.90000E-01 TO 0.45000 CONTOUR INTERVAL OF 0.30000E-01 PT(3,3)= 0.31476E-02 LABELS SCALED BY 1000

i) 11km

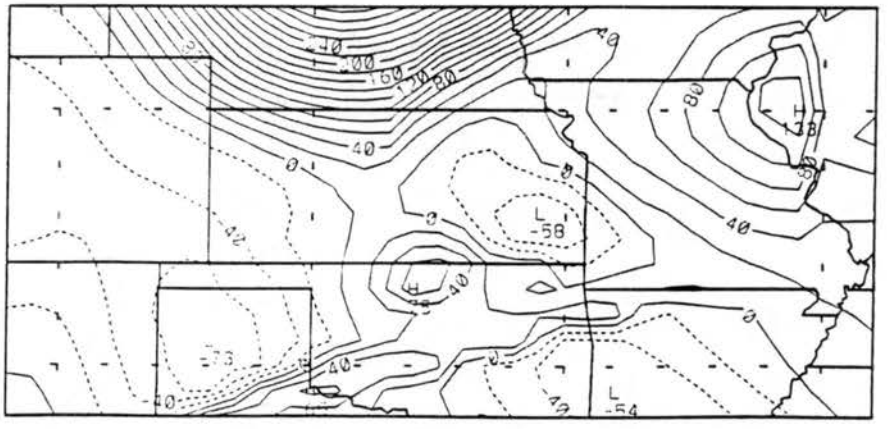

CONTOUR FROM -0.60000E-01 TO 0.32000 CONTOUR INTERVAL OF 0.20000E-01 PT(3,3)= -0.89525E-02 LABELS SCALED BY 1000.0

Figure 5.19 continued.

j) 12km

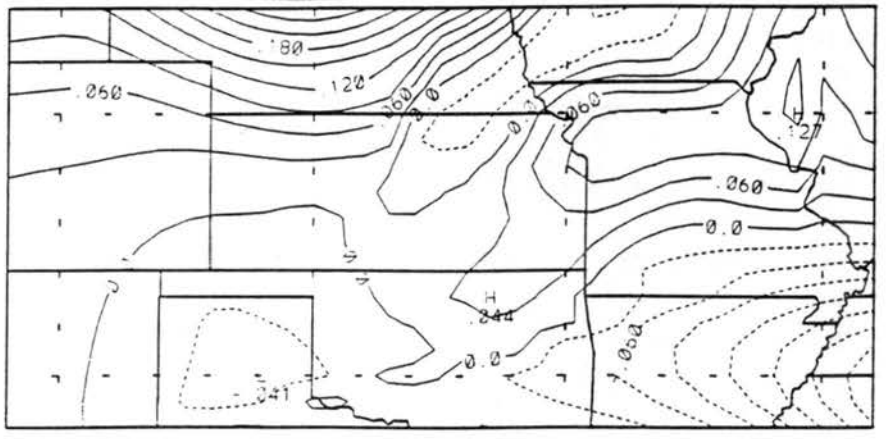

CONTOUR FROM -0.21000 TO 0.24000 CONTOUR INTERVAL OF 0.30000E-01 PT(3,3)= 0.90228E-02

k) 13km

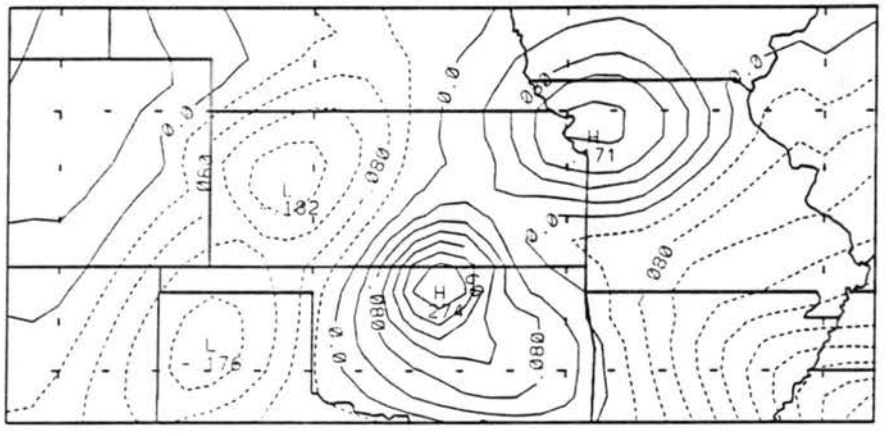

CONTOUR FROM -0.44000 TO 0.24000 CONTOUR INTERVAL OF 0.40000E-01 PT(3,3)= -0.38480E-

l) 14km

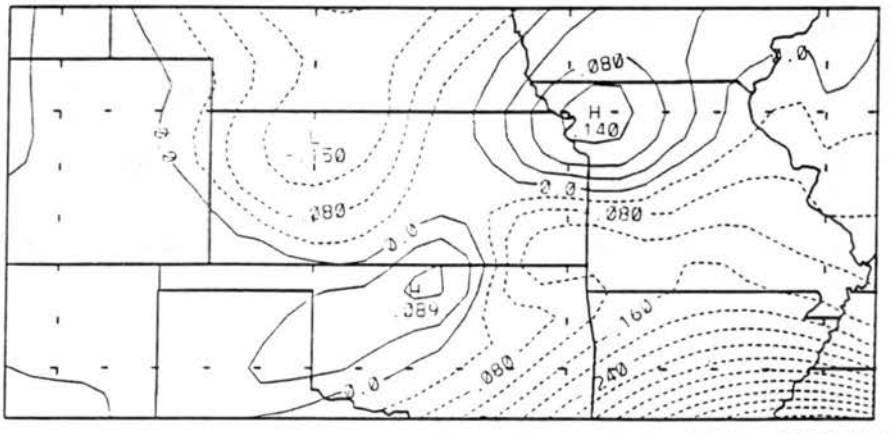

CONTOUR FROM -0.56000 TO 0.12000 CONTOUR INTERVAL OF 0.40000E-01 PT(3,3)= 0.27466E-02

Figure 5.19 continued.

averaged out and a nicely defined structure is exposed. Below 5km, upward motions predominated in the jet streak exit area above Kansas and Oklahoma. From 6km level, downward motions in the jet-streak right exit area grew rapidly and formed a structure with ascent on the left and descent on the right. The horizontal normal distance between the maximum centers of the upward motions and the jet streak axis was about 600km on the 6km surface, which is close to that reported by Shapiro(1981). From 8km and above, downward motions prevailed, and the pair of vertical motion cells across the jet disappeared. Instead, an dipole structure along the jet developed. In general, downward motion was tilting over the upward motion area and formed asymmetric to the jet axis. This prevailing tendency of downward motion is expected from shearing deformation and curvature as argued before.

The vertical velocity in a cross section normal to the jet streak (AB line in Figure 1.1) is presented in Figure 5.20. The grid spacial resolution is also 0.5°x0.5°. This figure shows a structure which has ascending motion mainly in the "remote" left exit area of the jet streak (38°,-96° to 41°, -93°), and descending motion near the jet streak core area (33°,-101° to 38°, -96°), while the maximum upward velocity was 0.07m/s locating in the upper troposphere, and the maximum downward motion was much larger with a value of about 0.31m/s. The ascending and descending motion cells were asymmetric to the jet axis and the descending motion area extended into the ascending area in the upper troposphere and the ascending portion extended toward and beneath the downward air motion area in the middle and lower

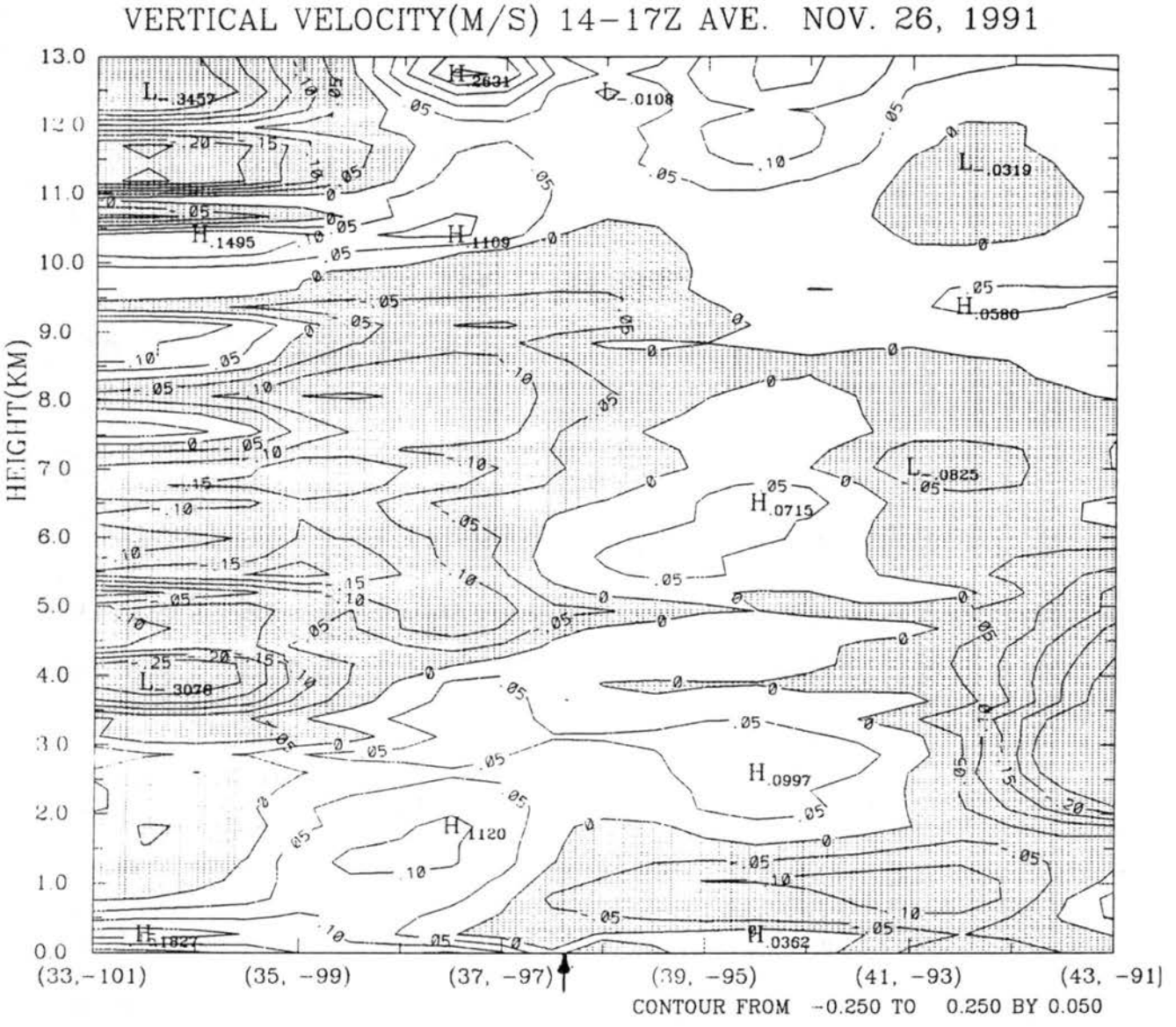

Figure 5.20 The three hour (14-17Z) averaged vertical velocity (m/s) in a cross section on line AB in Figure 1.1. The arrow indicates the location of NDS. From direct measurements by NOAA wind profiler network. The positive (negative) means upward (downward) motion.

troposphere. Descending motion exceeded upward motion in the jet streak exit area in the troposphere. It should be noted that, from Figure 5.20, the reversal level of the vertical velocities dropped to the 8km level at NDS site. A small area of descending motion was present in the layer between 7 and 10km, conflicting with the results shown in Figure 5.18. The cause of this discrepancy is possibly due to the interpolation algorithm used to create the cross section plot.

The 1200Z ECMWF analyses of the vertical wind velocities at different levels (i.e. 500mb, 400mb, 250mb, 200mb and 150mb) over the U.S are shown in Figure 5.21. The unit of these fields is Pa/s and the dashed (solid) lines represent upward (downward) motion. Generally, stronger vertical motions were formed at lower levels and the magnitude decreased with height. On the 500mb surface, upward motion of 0.15 Pa/s (3.0cm/s) is found in the jet streak left exit region over Kansas and Nebraska, and a downward motion of about 0.3 Pa/s (6.0cm/s) is observed in the right exit region over New Mexico and western Texas. The large values over Colorado on the 400mb and 500mb surfaces are questionable data since there was no any hints of such strong convection. At 250mb, the upward motion in Kansas disappeared and was replaced by a weak downward motion (i.e., less than 0.1 Pa/s (3cm/s)), however, the downward motion in the right-exit area was getting even stronger. On the 200mb surface, the area of downward motion expanded and covered almost the entire exit region, but the magnitude remained nearly the same. The cross-jet variation of the vertical wind field shows ascending motion below 250mb descending motion aloft in

a) 500mb

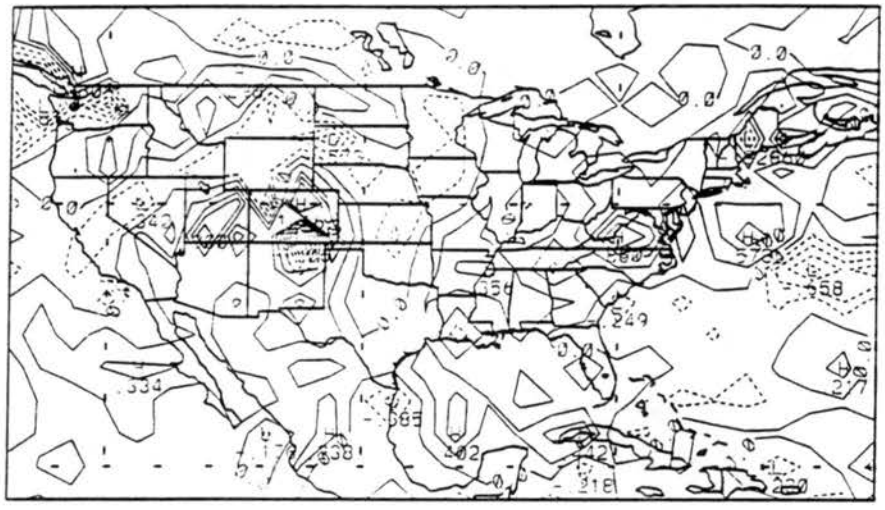

b) 400mb

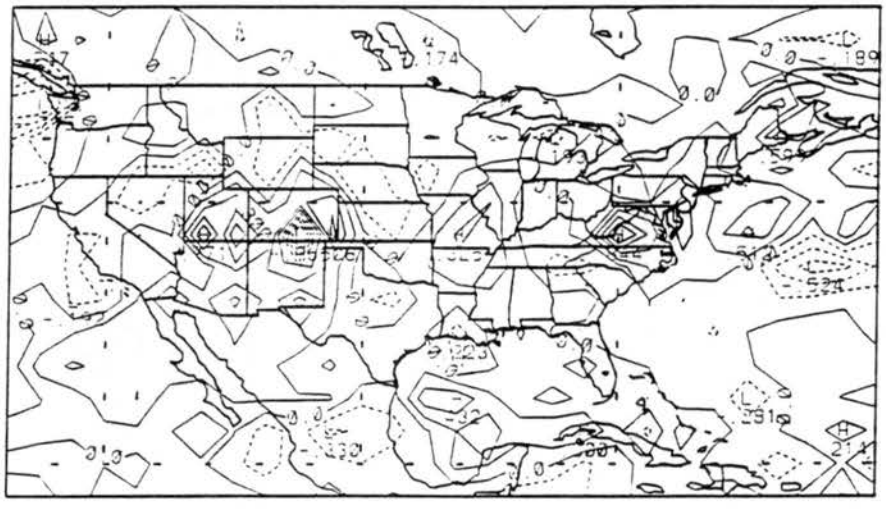

Figure 5.21 ECMWF analysis vertical velocity contours at 1200Z, November 26. Unit Pa/s. Positive and negative values represent downward and upward motions, respectively.

c) 250mb

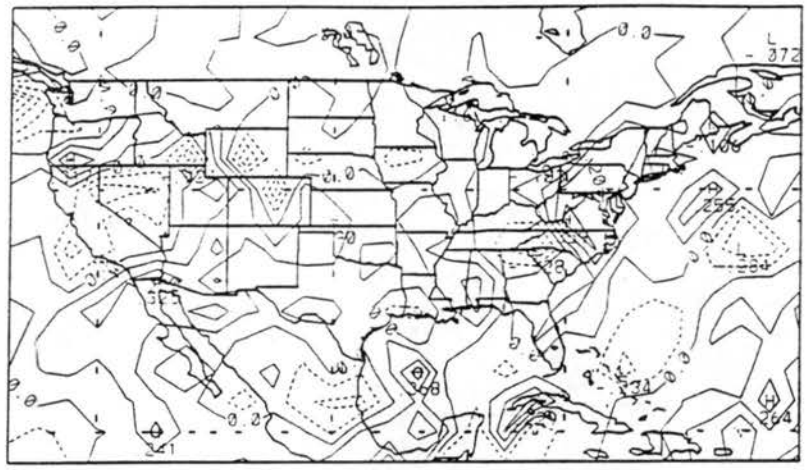

d) 200mb

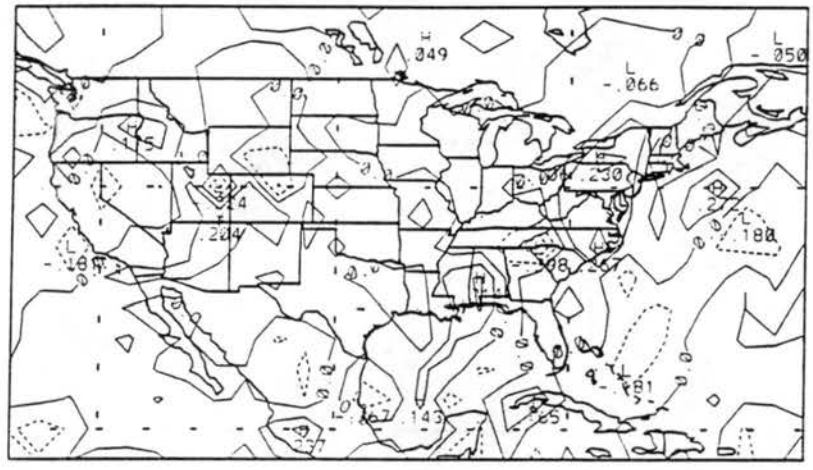

e) 150mb

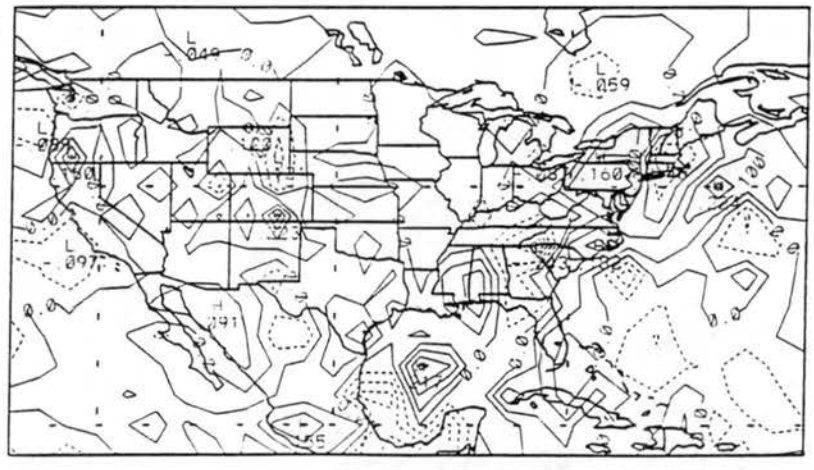

Figure 5.21 continued.

the left exit area, and a larger area of downward motion in the central and right exit regions. This structure agrees very well with the direct observations shown in Figure 5.19. A further comparison of Figure 5.19 and Figure 5.21 provides evidence of the existence of along-jet variations of the vertical wind; in the layers above 400mb, there is a dipole structure of the vertical wind, i.e., a downward (upward) motion found in the left exit area was followed by an upward (downward) motion along the direction of jet.

In general, there is good consistency among the vertical velocity fields obtained from different methods. The large-scale upward motions in the jet streak left-exit region support the development of cirrus cloud system. The hourly averaged vertical wind velocity is of order 10cm/s. Shearing deformation and curvature effects on the ageostrophic circulation of the jet streak are evident. A schematic diagram of the vertical wind field in the jet streak's exit area for the case on November 26, 1991, is shown in Figure 5.22(b). Offsets from the classical two-dimensional model (Figure 5.22(a)) is apparent. As shown in Figure 4.2, the secondary ageostrophic circulation corresponding to the warm advection will decrease the strength of upward motion in the left-exit area and shift the zero velocity points to the warm side of the jet. The convergence on the left side of the trough caused by the curvature effect (Figure 4.3) also decrease the ascending motion in the left-exit area.

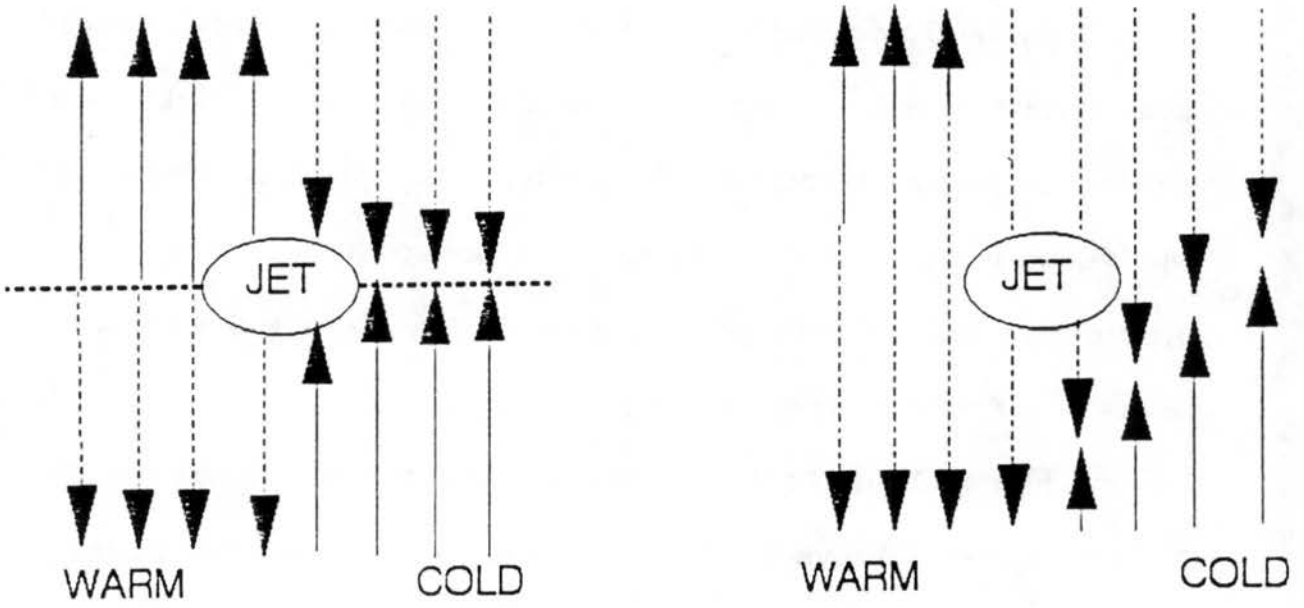

Figure 5.22 Schematic vertical cross section of the vertical wind field in a jet-streak exit area according to a) the classical model, b) the observations of November 26th, 1991. Up-pointed arrows represent upward motion.

Chapter 6

SUMMARY AND CONCLUSIONS

Studies were performed on determining the potential of Model-400 wind profilers in vertical wind velocity measurement. Direct (DDM) and indirect (QVAD and KM) methods were applied and their results were intercompared. Clear air radar echoing mechanisms were evaluated in order to interpret wind profiler signals and for defining radar sensitivity to ice particles. Turbulent structures in the cirrus cloud layer and environment is investigated around the cloud using the static instability, KH instability profiles and wind profiler signal return from the atmosphere. The jet streak ageostrophic circulation conceptual model and theory were discussed and compared with the observational results.

The CSU wind profiler spectral data were used to determine the capability of a Model-400 wind profiler for detecting the vertical wind signals in the presence of strong clutter effects. The vertical wind signal return is often obscured by strong signal returns from 'ground clutter.' The time-height structure of clutter signals showed strong temporal and spatial variations, however, they are still more regular than the vertical velocity signal.

Consideration of the mechanisms which produce echos for a Model-400 wind profiler shows that reflective turbulence is more effective than Rayleigh backscattering by ice particles in a cirrus cloud. However, downward motions during a cirrus cloud event were shown by the 6- or 10-minute cycle wind profiler data in our case. These downward motions were explained as ice particle fallout turbulence

at a spacial scale of several tens of centimeter rather than Rayleigh scattering by the particles themselves. Two major periods of strong echo were observed which corresponded to an area of large shear-induced turbulence, and an area which was nearly well-mixed at the beginning and later became thermally stratified.

The analysis of cirrus clouds' and cirrus environment thermal instability and dynamical instability structures shows a nearly well-mixed cloud and sub-cloud layer with a thermally very stable layer above and a thermally slightly more stable layer below. The average lapse rates are 1.4°K/km for the cloud and sub-cloud layers, 34°K/km right above the cloud layer and 4.33°K/km below the nearly neutral layer. Compared to the layer above cloud, the vertical shear of horizontal wind is much smaller at the cloud and subcloud layer before and during the cloud formation period. Richardson number profiles suggest the existence of several dynamically turbulent regions in the cloud layer. There is also the strong possibility of KHI right above cloud top, however, there was no KH wave structure visible. There was also no evidence of evaporation dissipation of cloud due to entrainment of cooler and dry in air from above the cloud by KHI.

A transverse secondary circulation in the jet streak exit area was identified generally as a thermally indirect circulation cell. Deviations from the classical two-dimensional model were recognized. The importance of geostrophic shearing deformation of an along-jet thermal gradient was manifested in weakened upward motion on the cold side of the jet and stronger downward motion on the warm side. The effect of a curved trajectory was also detected as the jet streak entered an

upper-level trough and along the jet component of the ageostrophic wind in the upper troposphere increased.

Vertical velocities deduced from three methods show both consistencies and discrepancies. The Kinematic and Quasi-VAD methods were better for calculating large scale vertical motions. The direct measurement of the vertical velocities, however, was strongly affected by what appeared to be random, small scale air motions and produced larger vertical wind velocities. Usually, these small scale motions in the direct measurement cancel after temporal averaging. In the presence of cirrus clouds, a net downward motion inside and below the cloud layer was deduced from the vertical beam radial velocities. In spite of this, a large-scale upward vertical velocity in the presence of a cirrus cloud was revealed by all three methods. A three dimensional structure of the vertical wind field associated with jet streak ageostrophic circulations was effectively retrieved by the three-hour averaged direct measurement.

It is concluded from this study that, in general, the cloud system was supported by large scale upward forcing (on order of 10cm/s) produced by the jet streak system, and horizontal moisture advection. There is no hint of strong convection.

In the future, statistical studies of clutter signal are strongly suggested for improving the clutter-removal algorithms which are especially important for directly measuring the vertical wind with wind profilers. Further investigations on the echo producing mechanisms of a Model-400 wind profiler are also very important for understanding the effects of cirrus clouds on the wind measurement, and defining the

scale of motion measured by wind profilers. A more quantitative study of the geostrophic stretching, shearing deformations of along-jet thermal gradient in modifying a transverse ageostrophic circulation and the curvature effect on the possible along-jet ageostrophic circulation should be performed for this jet-streak case.

REFERENCES

Akima, H. 1978: A method of bivariate interpolation and smooth surface fitting for values given at irregularly distributed points. *ACM-TOMS*, **4**, No. 2, June 1978.

Akima, H. 1984: On estimating partial derivatives for bivariate interpolation of scattered data. *Rocky Mountain Journal of Mathematics*, **14**, No. 1, Winter 1984.

Atlas, D., 1964: Advances in radar meteorology. *Adv. in Geophys.*, **10**, 317-478.

Atlas, D., K. R. Hardy and K. Naito, 1966: Optimizing the radar detection of clear air turbulence. *J. Appl. Meteor.*, **5**, 450-460.

Bluestein, H. B., 1993: Synoptic-Dynamic Meteorology in Midlatitudes. Vol. II, Observations and Theory of Weather Systems. Oxford University Press.

Brost, R. A., J. C. Wyngaard, and D. H. Lenschow, 1982: Marine stratocumulus layers. Part II: Turbulence budgets. *J. Atmos. Sci.*, **39**, 818-836.

Browning, K. A., 1971: Structure of the atmosphere in the vicinity of large-amplitude Kelvin-Helmholtz billows. *Quart. J. R. Met. Soc.*, **97**, 283-299.

Davies-Jones, R., 1993: Useful formulas for computing divergence, vorticity, and their errors from three or more stations. *Mon. Wea. Rev.*, **121**, 713-725.

Dmitriev, V. K., T. P. Kapitanova, V. D. Litvinova, N. G. Pinus, G. A. Potertikova, and G. N. Shur, 1984: Meso- and microscale structure of wind and temperature fields in jet stream Ci clouds, The 9th International Cloud Physics Conference, vol. 2, Tallin, 1984, 347-350.

Gage, K. S., and B. B. Balsley, 1978: Doppler radar probing of the clear atmosphere. *Bull. Amer. Meteor. Soc.*, **59**, 1074-1093.

Gossard, E. E., J. E. Gaynor, R. J. Zamora and W. D. Neff, 1985: Fine structure of elevated stable layers observed by sounder and in-situ tower sensors. *J. Atmos. Sci.*, **42**, 2156-2169.

Gossard, E. E., 1990: Radar research on the atmospheric boundary layer. *Radar in Meteorology*, D. Atlas, Eds., Amer. Meteor. Soc., 477-527.

Gossard, E. E., and A. S. Frisch, 1987: Relationship of the variances of temperature and velocity to atmospheric static stability-Application to radar and acoustic sounding. *J. Climate. Appl. Meteor.*, **26**, 1021-1036.

Gultepe, I., A. J. Heymsfield and D. H. Lenschow 1990: A comparison of Vertical Velocity in Cirrus Obtained from Aircraft and Lidar Divergence Measurements during FIRE. *J. Atmos. Ocean. Tech.*, **7**, 58-67.

Gultepe, I., and D. Starr, 1992: Microphysical and radiative development of a cirrus cloud during FIRE: implications for dynamic effects. 11th International Conference on Clouds and Precipitation, Vol.1, Canada, 545-548.

Gyakum, J. R., and M. Cai, 1990: An observational study of strong vertical wind shear over north America during the 1983/84 cold season. *J. Appl. Meteor.*, **29**, 902-915.

Hermes, L. G. 1991: Comparisons of rawinsonde-deduced kinematic and thermodynamic quantities with those deduced from VHF profiler observations. *Mon. Wea. Rev.*, **119**, 1693-1712.

Hocking, W. K, and J. Rottger, 1983: Pulse length dependence of radar signal strengths for Fresnel backscatter. *Radio Sci.*, **18**, 1312-1324.

Hocking, W. K., 1986: Observation and measurement of turbulence in the middle atmosphere with a VHF radar. *J. Atmos. Terres. Phys.*, **48**, 655-670.

Hildebrand, P. H., and R. S. Sekhon, 1974: Objective determination of the noise level in Doppler spectra. *J. Appl. Meteor.*, **13**, 808-811.

Heymsfield, A., 1975: Cirrus uncinus generating cells and the evolution of cirriform clouds.- Part II: the structure and circulations of the cirrus uncinus generating head. *J. Atmos. Sci.*, **32**, 809-819.

Keeler, R. J. and R. E. Passarelli, 1990: Signal processing for atmospheric radars. *Radar in Meteorology*, D. Atlas, Ed., Amer. Meteor. Soc., 199-229.

Kennedy, P. J. and M. A. Shapiro, 1975: The energy budget in a clear air turbulence zone as observed by aircraft. *Mon. Wea. Rev.*, **103**, 650-654.

Kennedy, P. J. and M. A. Shapiro, 1980: Further encounters with clear air turbulence in research aircraft. *J. Atmos. Sci.*, **37**, 986-993.

Keyser, D. and M. A. Shapiro, 1986: Review -- A review of the structure and dynamics of upper-level frontal zones. *Mon. Wea. Rev.*, **114**, 452-499.

Keyser, D., and M. J. Pecnick, 1985a: A two-dimensional primitive equation model of frontogenesis forced by confluence and horizontal shear. *J. Atmos. Sci.*, **42**, 1259-1282.

Keyser, D., and M. J. Pecnick, 1985b: Diagnosis of ageostrophic circulations in a two-dimensional primitive equation model of frontogenesis. *J. Atmos. Sci.*, **42**, 1283-1305.

Keyser, D., and D. R. Johnson, 1984: Effects of diabatic heating on the ageostrophic circulation of an upper tropospheric jet streak. *Mon. Wea. Rev.*, **112**, 1709-1724.

Larsen, M. F., 1983: Can a VHF Doppler radar provide synoptic wind data? - A comparison of 30 days of radar and radiosonde data. *Mon. Wea. Rev.*, **111**, 2047-2057.

Larsen, M. F., and J. Rottger, 1991a: VHF radar measurements of in-beam incidence angles and associated vertical-beam radial velocity corrections. *J. Atmos. Oceanic Technol.*, **8**, 477-490.

Larsen, M. F., S. Fukao, O. Aruga, M. D. Yamanaka, T. Tsuda and S. Kato, 1991b: A comparison of VHF radar vertical-velocity measurements by a direct vertical-beam method and by a VAD technique. *J. Atmos. Oceanic Technol.*, **8**, 766-776.

Ludlam, F. H., 1967: Characteristics of billow clouds and their relation to clear air turbulence. *Quart. J. R. Met. Soc.*, **93**, 419-435.

Miles, J. W. and L. N. Howard, 1964: Note on a heterogeneous shear flow. *J. Fluid Mech.*, **20**, 331-336.

Namias, J. and P. F. Clapp, 1949: Confluence theory of the high tropospheric jet stream. *J. Metero.*, **6**, 330-336.

Nastrom, G. D., 1984: Detection of synoptic-scale vertical velocities using an MST radar. *Geophys. Res. Lett.*, **11**, 57-60.

Nastrom, G. D., 1985: Direct measurement of large-scale vertical velocities using clear-air Doppler radars. *Mon. Wea. Rev.*, **113**, 708-718.

O'Brien, J. J., 1970: Alternative solutions to the classical vertical velocity problem. *J. Appl. Meteor.*, **9**, 197-203.

Peterson, V. L., 1988: Wind profiling - The history, principles, and applications of clear-air Doppler radar. Tycho Technology, Inc.

Peterson, V. L., and B. B. Balsley, 1979: Clear air Doppler radar measurements of the vertical component of wind velocity in the troposphere and stratosphere. *Geophys. Res. Lett.*, **6**, 933-936.

Plank, V. G., D. Atlas and W. H. Paulsen, 1955: The nature and detectability of clouds and precipitation as determined by 1.25 centimeter radar. *J. Meteor.*, **12**, 358-378.

Rottger, J., and M. F. Larsen, 1990: UHF/VHF radar techniques for atmospheric research and wind profiler applications. *Radar in Meteorology,* D. Atlas, Ed., Amer.Meteor.Soc., 235-281.

Sato, T., and R. F. Woodman, 1982: Fine altitude resolution observations of stratospheric turbulent layers by the Arecibo 430MHz radar. *J. Atmos. Sci.*, **39**, 2546-2552.

Sassen, K., C. J. Grund, J. D. Spinhirne, M. M. Hardesty, and J. M. Alvarez, 1990: The 27-28 October 1986 FIRE IFO cirrus case study: a five lidar overview of cloud structure and evolution. *Mon. Wea. Rev.*, **118**, 2288-2311.

Shapiro, M. A., 1981: Frontogenesis and geostrophically forced secondary circulations in the vicinity of jet stream-frontal zone systems. *J. Atmos. Sci.*, **38**, 954-973.

Skov, R. A., 1986. Nowcasting thermodynamic profiles using a triangle of wind profilers in an advection model. M.S. Thesis, Univ. of Oklahoma Graduate College.

Starr, D. and A. R. Lare, 1993a: Meteorological analysis of the December 4-6 FIRE cirrus-II case. NASA Conference Publication 3238, FIRE Cirrus Science Results, 92-97.

Starr, D. and A. R. Lare, 1993b: Meteorological Analysis of the November 25 FIRE cirrus-II case: A well-defined ridge-crest cirrus system over Oklahoma. NASA Conference Publication 3238, FIRE Cirrus Science Results, 144-147.

Starr, D. and D. P. Wylie, 1990: The 27-28 October 1986 FIRE cirrus case study: Meteorology and clouds. *Mon. Wea. Rev.*, **118**, 2259-2287.

Starr, D. and S. K. Cox, 1985a: Cirrus clouds-Part I: A cirrus cloud model. *J. Atmos. Sci.*, **42**, 2663-2681.

Starr, D. and S. K. Cox, 1985b: Cirrus clouds-Part II: Numerical experiments on the formation and maintenance of cirrus. *J. Atmos. Sci.*, **42**, 2682-2694.

Tycho Technology, Inc., 1989: Model 400S 3-beam wind profiler - Software user's manual.

Uccellini, L. W. and D. R. Johnson, 1979: The coupling of upper and lower tropospheric jet streaks and implications for the development of severe convective storms. *Mon. Wea. Rev.*, **107**, 682-703.

Woodman, R. F., and A. Guillen, 1974: Radar observations of winds and turbulence in the stratosphere and mesosphere. *J. Atmos. Sci.*, **31**, 493-505.

Woods, J. D., 1969: On Richardson's number as a criterion for laminar-turbulent-laminar transition in the ocean and atmosphere. *Radio Science*, **4**, 1289-1298.

Yagi, T., 1969: On the relation between the shape of cirrus clouds and the static stability of the cloud level-studies of cirrus clouds: Part IV, *J. Meteor. Soc. Japan*, **47**, 59-64.

Yoe, J. G., M. F. Larsen and E. J. Zipser 1992: VHF Wind-Profiler Data Quality and Comparison of Methods for Deducing Horizontal and Vertical Air Motions in a Mesoscale Convective Storm. *J. Atmos. Oceanic Technol.*, **9**, 713-727.

Appendix A.

Location and Orientation of Wind Profilers

Table A.1 gives information on the geographical location and beam direction of NOAA wind profilers and CSU wind profiler, which are mapped in Figure 1.1.

Table A.1

Station	Latitude (deg)	Longitude (deg)	Elevation (m)	Orient. from True North(deg)*
PLT	40.18	-104.71	1524	0
SBY	42.41	-71.48	93	-70
WSM	32.40	-106.34	1224	-5
PRC	34.97	-97.51	331	-13
BMF	41.88	-72.70	56	N/A
VCI	36.07	-99.21	648	-10
LMN	36.69	-97.48	306	-12
HKL	35.80	-95.78	212	-16
NDS	37.37	-95.63	255	-14
HVL	37.65	-99.09	648	-10
HBR	38.30	-97.29	447	-8
CNW	37.52	-92.70	390	-16
OKO	34.08	-88.86	125	-22
DQU	34.11	-94.29	195	-17

PAT	31.77	-95.71	119	-17
WNF	31.89	-92.78	93	-20
JTN	33.01	-100.98	707	-11
TCU	35.08	-103.60	1241	-6
AZC	36.84	-107.90	1902	0
GDA	37.77	-102.17	1155	-6
MBW	41.90	-106.18	1997	1
MRR	42.90	-101.69	991	-4
RWD	40.08	-100.65	800	-6
FBY	40.09	-97.34	433	-10
NLG	42.20	-97.79	524	-8
CSU**	37.30	-95.12	269	5

* Positive values represent the case that beam turns to the east.

** CSU wind profiler site near Parsons, Kansas

APPENDIX B

Thermal Instability and Dynamic Instability

Several concepts based on the stability of the atmosphere, have been used in understanding the dynamics of the atmosphere. These include but are not limited to (conditional) static stability, convective instability, shear-induced instability (also referred as K-H instability, a form of dynamic instability), and baroclinic instability. In this section, we will emphasize only static stability and shear-induced instability which are important to the explanations of cirrus cloud structure and radar echo mechanisms.

Static stability is traditionally defined by the local lapse rate of temperature and potential temperature as following,

Statically stable	$d\theta/dz > 0$
Statically neutral	$d\theta/dz = 0$
Statically unstable	$d\theta/dz < 0$

These definitions generally work well in most part of the atmosphere above the boundary layer. Some concerns for the convective boundary layer is mentioned by Stull (1988).

Shear-induced turbulence is normally defined in a statically stable (or, thermally stratified) atmosphere, in which buoyancy tends to suppress turbulence and wind shears tend to enhance turbulence (Stull, 1988, pp175). While the buoyant

production term in the TKE (Turbulent Kinematic Energy) budget equation (cf. Eq.(5.1b) in Stull, 1988) is normally negative, the mechanical production term is positive due to wind shears. Experimental data and theoretical studies suggest that shear-induced turbulence can only occur if the strength of the shear production with respect the buoyancy suppression exceeds a critical limit. A simplified parameter, Flux Richardson number(R_f), which is the ratio of the buoyancy term and the shear production term, has often been used to examine this type of dynamical instability.

$$R_f = \frac{\left(\frac{g}{\bar{\theta}_v}\right)\left(\overline{w'\theta_v'}\right)}{\left(\overline{u_i'u_j'}\right)\frac{\partial \bar{U}_i}{\partial x_j}} \qquad (1)$$

where,

g -- gravitational acceleration

θ_v -- virtue potential temperature

$u_{i,j}$, w -- horizontal and vertical wind components

(bar) -- averaging

(′) -- perturbation

Assuming horizontal homogeneity and neglecting subsidence, the flux Richardson number (R_f) can be expressed as:

$$R_f = \frac{\left(\frac{g}{\bar{\theta}_v}\right)\left(\overline{w'\theta_v'}\right)}{\left(\overline{u'w'}\right)\frac{\partial \bar{U}}{\partial z} + \left(\overline{v'w'}\right)\frac{\partial \bar{V}}{\partial z}} \qquad (2)$$

Traditionally, the onset of turbulence requires R_f to be one, which means that the mechanical term balances the buoyant term in a TKE equation. In Stull (1988), Rf $< +1$ is a necessary and sufficient condition for the atmosphere being turbulent, however, Rf$>+1$ is only a necessary condition for atmosphere being laminar.

This Flux Richardson number is, however, not practically useful to study turbulence in a laminar flow because perturbation parameters are not available (Stull, 1988). Thus, a substitution parameter called Gradient Richardson number (Ri), based on the Flux Richardson number by applying the K-theory, is introduced:

$$R_i = \frac{\frac{g}{\theta_v}\frac{\partial \theta_v}{\partial z}}{\left(\frac{\partial U}{\partial z}\right)^2 + \left(\frac{\partial V}{\partial z}\right)^2} \qquad (3)$$

The advantage of R_i is that it uses measurable mean atmospheric quantities instead of the their perturbation values. Stull(1988) shows different critical values of the Gradient Richardson number Rc (lower limit) and Rt (upper limit). $R_i<R_c$ is the sufficient condition for the atmosphere being turbulent and $R_i>R_t$ is the sufficient condition for the laminar atmosphere. Usually, Rc = 0.21 to 0.25 and Rt = 1 leaving a range in which the stability is not certain. Stull (1988) suggested that in this range, Ri of nonturbulent flow must be lowered to Rc for the onset of the turbulence, but once turbulent, the instability can continue until Ri=Rt. This phenomena is also called "Richardson number hysteresis" in Woods(1969).

Since the atmospheric state parameters are normally measured at discrete points,

their values are typically used to represent an average over some area. This leads to the definition of the Bulk Richardson number, which is defined as Equation 5.4 for a layer ΔZ at Z.

$$R_i(Z) = \frac{\frac{g}{\theta(Z)}\left(\frac{\Delta\theta}{\Delta Z}\right)}{\left(\frac{\Delta V}{\Delta Z}\right)^2} = \frac{\frac{g}{\theta(Z)}\left(\frac{\Delta\theta}{\Delta Z}\right)}{\left(\frac{\Delta U}{\Delta Z}\right)^2 + \left(\frac{\Delta V}{\Delta Z}\right)^2} \qquad (4)$$

where, ΔV is the magnitude of the vector wind shear over the depth, ΔZ is the thickness of the layer and θ is the mean potential temperature. Due to the significant variation in the thickness of the turbulent layer (Browning, 1971), which may range from the order of meters to hundreds of meters, the Bulk Richardson number may not show the real properties of the subregional area of interest since it represents the average of the whole layer. The previously mentioned critical values may not apply to the Bulk Richardson number which varies with spatial resolution of the measurements.

Several researches have investigated the theoretical critical value of the Richardson number. Through purely mathematical arguments, Miles and Howard (1964) found that $Ri \leq 0.25$ is a necessary condition for the existence of the shear-induced instability. Their conclusion, however, is somewhat inconclusive since they used an idealized structure of the shear layer, within which the velocity and the density varied linearly and external to the layer, the velocity and air density were constant. This structure may not be representative of the real atmosphere. On the other hand, observational studies by Ludlam (1967) and Browning (1971) have shown

some consistency with a 0.25 critical Richardson number, with also the disagreements. Vinnichenko and Dutton (1969) and Gyakum and Cai (1990) give a wider limit for the condition of shear-induced instability in the clear atmosphere with a critical Richardson number of 1.0. The differences between the theoretical study and the observations are likely due to the observational inaccuracies and difficulties. In the sense of bulk values, the Richardson number has been averaged over the whole layer and the observed critical value of Ri usually decreases with the decreases of the layer thickness and approaches the theoretical value of 0.25.